

Confinement of relativistic runaway electrons in tokamak plasmas

Citation for published version (APA):

Entrop, I. (1999). *Confinement of relativistic runaway electrons in tokamak plasmas*. [Phd Thesis 1 (Research TU/e / Graduation TU/e), Applied Physics and Science Education]. Technische Universiteit Eindhoven. <https://doi.org/10.6100/IR528445>

DOI:

[10.6100/IR528445](https://doi.org/10.6100/IR528445)

Document status and date:

Published: 01/01/1999

Document Version:

Publisher's PDF, also known as Version of Record (includes final page, issue and volume numbers)

Please check the document version of this publication:

- A submitted manuscript is the version of the article upon submission and before peer-review. There can be important differences between the submitted version and the official published version of record. People interested in the research are advised to contact the author for the final version of the publication, or visit the DOI to the publisher's website.
- The final author version and the galley proof are versions of the publication after peer review.
- The final published version features the final layout of the paper including the volume, issue and page numbers.

[Link to publication](#)

General rights

Copyright and moral rights for the publications made accessible in the public portal are retained by the authors and/or other copyright owners and it is a condition of accessing publications that users recognise and abide by the legal requirements associated with these rights.

- Users may download and print one copy of any publication from the public portal for the purpose of private study or research.
- You may not further distribute the material or use it for any profit-making activity or commercial gain
- You may freely distribute the URL identifying the publication in the public portal.

If the publication is distributed under the terms of Article 25fa of the Dutch Copyright Act, indicated by the "Taverne" license above, please follow below link for the End User Agreement:

www.tue.nl/taverne

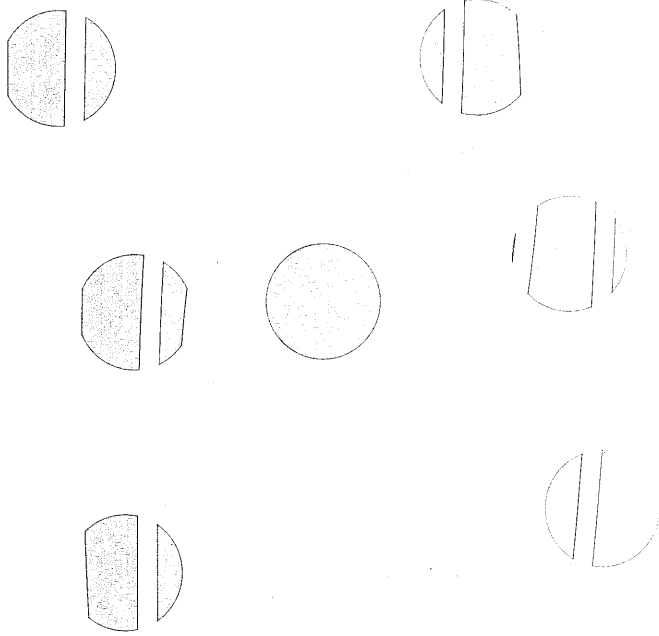
Take down policy

If you believe that this document breaches copyright please contact us at:

openaccess@tue.nl

providing details and we will investigate your claim.

Confinement of relativistic runaway electrons in tokamak plasmas



Ingeborg Entrop

Confinement of relativistic runaway electrons in tokamak plasmas

CIP-DATA LIBRARY TECHNISCHE UNIVERSITEIT EINDHOVEN

Entrop, Ingeborg

Confinement of relativistic runaway electrons in tokamak plasmas / by
Ingeborg Entrop. - Eindhoven: Technische Universiteit Eindhoven, 1999. -
Proefschrift. - ISBN 90-386-0947-7

NUGI 812

Trefw.: plasma / tokamak / opsluiting / elektronen

Subject headings: plasmas / tokamak / confinement / electrons

Confinement of relativistic runaway electrons in tokamak plasmas

PROEFSCHRIFT

ter verkrijging van de graad van doctor aan de
Technische Universiteit Eindhoven, op gezag van de
Rector Magnificus, prof.dr. M. Rem, voor een
commissie aangewezen door het College voor
Promoties in het openbaar te verdedigen
op maandag 20 december 1999 om 14.00 uur

door

Ingeborg Entrop

geboren te Dordrecht

Dit proefschrift is goedgekeurd door de promotoren:

prof.dr. N.J. Lopes Cardozo
en
prof.dr. F.C. Schüller

Copromotor:
dr. R. Jaspers

The work described in this thesis was done under the Euratom-KFA and Euratom-FOM association agreements as part of a research program of the Stichting voor Fundamenteel Onderzoek der Materie (FOM) and Institut für Plasmaphysik, Forschungszentrum Jülich GmbH, with financial support from the Nederlandse Organisatie voor Wetenschappelijk Onderzoek (NWO), Euratom and Forschungszentrum Jülich. It was carried out at the TEXTOR-94 tokamak, Institut für Plasmaphysik, Forschungszentrum Jülich GmbH, Germany, in collaboration with the FOM-Instituut voor Plasmafysica 'Rijnhuizen'.

"Wisest is she who knows she does not know..."

Alberto Knox
(in 'Sophie's World' - Jostein Gaarder)

Contents

1	Introduction	1
1.1	Nuclear fusion	1
1.2	Tokamak	2
1.3	Transport	3
1.4	Runaway electrons	4
1.5	This thesis	6
1.6	Publications	8
	References	10
2	Runaway electrons	11
2.1	Electron runaway	11
2.2	Generation	14
2.3	Orbits	17
2.4	Energy limits	20
2.5	Transport	23
	References	28
3	Runaway detection	31
3.1	Synchrotron radiation	31
3.2	Infrared measurements	35
3.3	Other runaway diagnostics	40
	References	42
4	Simulations	43
4.1	Radiation evolution	43
4.2	Poloidal projection of radiation cone	49
	References	52
5	Runaway transport in Ohmic plasmas	53
5.1	Introduction	54
5.2	Experiment	57

5.2.1	Set-up	57
5.2.2	Image processing	57
5.2.3	Typical measurement	59
5.3	Method of data analysis	60
5.3.1	Transport model	60
5.3.2	Relation between intensity of radiation and number of runaways	61
5.3.3	Source density profile	64
5.3.4	Diffusion coefficient	65
5.4	Results	66
5.5	Discussion	69
	References	73
6	Runaway transport during additional heating	75
6.1	Scale size of magnetic turbulence in tokamaks probed with 30 MeV electrons	76
	References	84
6.2	Runaway electron transport during additional heating in TEX- TOR-94	86
6.2.1	Introduction	86
6.2.2	Theory	88
6.2.3	Runaway detection in TEXTOR-94	91
6.2.4	Observations	91
6.2.5	Simulations	99
6.2.6	Relating the energy dependence of runaway confine- ment to the average width of perturbing magnetic modes	105
6.2.7	Discussion	110
6.2.8	Summary and conclusion	112
	References	113
7	Runaway snakes	115
7.1	Introduction	116
7.2	Runaway detection	118
7.2.1	Experimental set-up	118
7.2.2	Synchrotron radiation pattern	120
7.3	Runaway snake observations	124
7.3.1	Observation of runaway snake in part of poloidal cross section	124
7.3.2	A: Observation of a runaway snake in full poloidal view	125
7.3.3	B: Influence of plasma current on a runaway snake	129

7.3.4	C: Non-pellet induced runaway snake	131
7.3.5	Summary of observations	134
7.4	Derived parameters	134
7.4.1	Drift surface parameters	134
7.4.2	Runaway energy and pitch angle	136
7.4.3	Frequency	137
7.4.4	Confinement	137
7.5	Discussion	139
7.5.1	Runaway parameters	139
7.5.2	Higher order theory	140
7.5.3	Island width	141
7.5.4	Changes in q profile	141
7.5.5	Transport	141
7.5.6	Acceleration inside a runaway snake	142
7.6	Summary and conclusion	144
	References	145
8	Disruptions, fast pitch angle scattering and transport barriers	147
8.1	Disruptions	147
8.1.1	Introduction	147
8.1.2	Observations	149
8.1.3	Experiments	150
8.1.4	Discussion	151
8.2	Runaway electrons as probe for barriers?	153
8.2.1	Introduction	153
8.2.2	Effect of a barrier on runaway electron measurements	154
8.2.3	Observations	156
8.2.4	Discussion	157
8.3	Fast pitch angle scattering events	159
8.3.1	Introduction	159
8.3.2	New observations	161
8.3.3	Discussion	162
	References	163
9	Evaluation	165
	References	172
	Summary	173
	Samenvatting	177

Dankwoord	181
Curriculum vitae	183

Chapter 1

Introduction

1.1 Nuclear fusion

The world's energy demand is growing while the supplies of fossil fuel such as coal, oil and gas are shrinking. The environmental pollution and irreversible influence on climate that are the result of the use of these conventional energy sources are becoming a problem as well. To satisfy the future energy demand and simultaneously protect the environment, alternative energy sources that are clean, safe and sufficiently available in the next centuries, are searched for. One of the candidates of new energy sources for the future is nuclear fusion. Fusion is a very natural process: It provides the stars with energy.

Fusion is the process where two nuclei melt together under release of an enormous amount of energy. The reaction that is least difficult to initiate in a fusion reactor is the one between the two hydrogen isotopes deuterium $D \equiv {}^2_1\text{H}$ and tritium $T \equiv {}^3_1\text{H}$:



where ${}^4_2\text{He}$ stands for helium and n is an energetic neutron. Deuterium is present in water. Tritium is bred from lithium ${}^6_3\text{Li}$ which is present in sea water or can be mined. The amount of released energy in a fusion reaction is enormous: one liter of water contains an amount of deuterium (about 33 mg) that will produce as much energy as burning 260 liters of oil. Because the fuels are cheap and widely accessible, nuclear fusion is an almost inexhaustible energy source.

How clean and safe is fusion energy? Tritium is a radioactive hydrogen isotope with a half-life of about 12 years. The ash of the fusion reaction helium is a harmless inert element. The energetic neutron has the disadvantage to make the innermost parts of the fusion reactor radioactive. As long as the

tritium is produced in the reactor vessel itself and is kept in a closed system and as long as the half-life of the materials that are used to build the reactor vessel are relatively short (< 100 years), nuclear fusion is a relatively clean energy source.

The quantity of nuclear waste is small with respect to that of nuclear fission. An additional advantage of fusion above fission is the continuously flow of fuel into the reactor instead of a storage of fuel for years in the reactor: there is no possibility of explosion or melt-down. Moreover, nuclear fusion is not based on a chain reaction as fission is. Nuclear fusion is, therefore, inherently safer process than nuclear fission.

1.2 Tokamak

A fusion reaction only takes place at velocities that are large enough to overcome the repelling forces between the nuclei. These high velocities can be achieved by heating the fusion fuels. The burn temperature of the D – T reaction in a reactor is 10^8 K. At such high temperatures, atoms are fully ionized and form a gas of ions and electrons, a so-called plasma. A hot fusion plasma is confined in a magnetic field to avoid contact with the vessel wall. The most promising results in the field of nuclear fusion have been achieved in a test reactor of the type tokamak (derived from the Russian

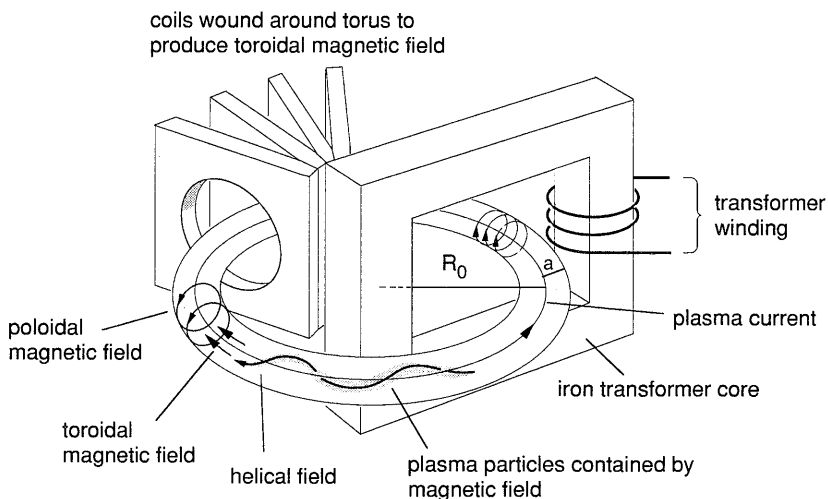


Figure 1.1: Schematic overview of a tokamak.

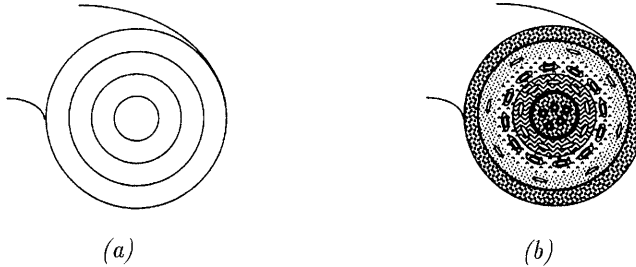


Figure 1.2: (a) *Nested magnetic surfaces* (b) *Perturbed magnetic field*

'toroidal'naya kamera i magnitnaya katushka', which means toroidal chamber with magnetic coils), which is schematically shown in figure 1.1.

In a tokamak [1], a plasma is confined by a helical magnetic field in a toroidal shaped vacuum vessel. External coils induce a toroidal field component B_t and a plasma current I_p induces a much weaker poloidal field component B_p . This plasma current is generated by using the plasma as the secondary winding of a transformer. The helicity of the resulting magnetic field is characterized by a winding number q , which indicates the number of toroidal turns that a field line makes to complete one poloidal turn.

The early years of tokamak research until now show an enormous increase in performance whereas the size has grown from a table-top experiment to almost full reactor size with plasma volumes of more than 100 m^3 . Nowadays, the star among the tokamaks is JET (Joint European Torus) in England. Records recently obtained in this largest tokamak in the world (major radius $R_0 = 3 \text{ m}$ and minor radius $a = 1 \text{ m}$) are

- a fusion power of 16.1 MW,
- a fusion energy of 21 MJ, produced in quasi-steady state in 3 seconds,
- a ratio between fusion power and input power of $P_{\text{fus}}/P_{\text{in}} \approx 0.65$.

1.3 Transport

The magnetic field topology in a tokamak consists of a set of nested toroidal surfaces spanned by field lines of equal winding number q as shown in figure 1.2(a). Transport of heat along the field lines is very fast, but because of the toroidal shape no losses occur in that direction. Transport perpendicular to the magnetic surfaces is expected to be governed by collisions and the

effects of the toroidal geometry. However, experiments show energy losses via electrons that are up to two orders of magnitude larger, and via ions less than one order of magnitude larger than theory predicts. This is the reason why no net energy production has been achieved yet by nuclear fusion in the tokamaks of a size presently operational.

When nuclear fusion should serve as a future energy source in reactors of acceptable size, it is important to understand the enhanced heat transport. Therefore, much effort is put into the study of this anomalous transport. Turbulent fluctuations in either the electric or magnetic field are held responsible for the enhanced transport. Electric field fluctuations move particles across the surfaces and the magnetic field keeps its topology of nested surfaces. Magnetic field fluctuations, however, break up the symmetry of the nested magnetic surfaces (see figure 1.2(b)). Magnetic field lines make radial excursions as do the particles that follow these lines. Especially magnetic field surfaces with low order rational values of the winding number q are sensitive to the perturbations. Small perturbations already change the topology of nested surfaces into a mixture of good surfaces, chains of magnetic islands and stochastic regions. For larger magnetic perturbations, the size of the magnetic islands increases. Where islands on different flux surfaces overlap, large stochastic layers exist. The behavior of the magnetic field lines in stochastic regimes cause an increased radial transport. A total description of the heat transport in a tokamak plasma probably unites aspects of both electrostatic and magnetic fluctuations.

Transport by electrostatic fluctuations has been extensively investigated. Magnetic turbulence is more difficult to diagnose because small perturbations of the order of 10^{-5} to 10^{-4} of the toroidal magnetic field B_t are sufficient to enhance the heat transport significantly. Hence, what the contribution of magnetic turbulence to heat transport is, is still an open question. This question will be investigated in this thesis.

1.4 Runaway electrons

In a tokamak plasma, a current is driven by the electric field induced by the transformer principle. Electrons are accelerated by the electric field, but they experience also friction due to collisions with ions and other electrons. The friction is inversely proportional to the square of the electron velocity. Only a small part of the total electron population has a sufficiently large velocity to escape from the influence of the friction. Once the acceleration is larger than the slowing down of the friction, electrons 'run away' from the thermal bulk electron population. These electrons are called runaway electrons.

Runaway electrons can be regarded as effectively collisionless. This makes them a suitable probe for investigating the non-collisional, turbulent, transport. Transport induced by electrostatic fluctuations is inversely proportional to the particle velocity, whereas transport induced by magnetic fluctuations is proportional to the particle velocity. Because of their large velocity, transport of runaway electrons is mainly determined by the magnetic perturbations. Therefore, the determination of the runaway electron transport gives a possible tool to probe the magnetic fluctuations.

However, there is a complication. The electrons in a tokamak do not follow magnetic field lines exactly because of the toroidal geometry. The magnetic field B is stronger at the inner side (the 'high field side') of the torus, which gives rise to a gradient in B . Furthermore, the magnetic field lines are curved. As a result of this gradient and curvature in B , the runaway electron orbits are shifted outward with respect to the magnetic field surfaces. This shift can be a few cm which is larger than the typical scale size of the magnetic turbulence. The sensitivity to magnetic fluctuations of high energy runaway electrons is, hence, strongly reduced.

The question how to diagnose the turbulence with runaway electrons is discussed in this thesis.

Electron runaway is subject of research, ever since the first publication by Giovanelli in 1949 [2]. Besides the use of runaways as possible probe for magnetic turbulence, other fields of interest are the runaway generation, acceleration and loss processes. Motivation for these particular fields of interest is found in the damaging effect of energetic runaways on reactor vessel components when they are lost. Especially during a sudden and violent loss of the energy confined in a plasma, a so-called disruption, large numbers of energetic runaways can be generated. In future reactors, these electrons could cause severe damage.

Detection of runaway electrons is usually done by measuring x-ray radiation emitted when runaways are lost from the plasma and hit a solid material. Runaway electrons also emit radiation themselves due to their toroidal motion. In TEXTOR-94 (Tokamak EXperiment for Technology ORiented Research, last upgrade (pulse lengthening) in 1994) which is a medium-sized limiter tokamak with circular cross section (for typical parameters, see table 1.1), this radiation - synchrotron radiation - is measured with an infrared camera. The first detection of runaway electrons by means of infrared measurements instead of the usual x-ray measurements from runaway losses was reported in 1990 by Finken et al. [3]. Since those pioneering measurements, a more systematic study was made by Jaspers [4]. New information was found on the runaway generation in general and during disruptions in particular, on instabilities from interaction between runaways and waves and on the

Table 1.1: An overview of the machine parameters of the TEXTOR-94 tokamak.

TEXTOR-94 parameters			
major radius	R_0	1.75	m
minor radius	a	0.46	m
toroidal magnetic field	B_t	1.3-2.9	T
<i>standard operation</i>		2.2	T
plasma current	I_p	200-800	kA
<i>standard operation</i>		350	kA
loop voltage	V_{loop}	1	V
pulse duration	τ_{pulse}	10	s
<i>standard operation</i>		5	s
auxiliary heating	P_{NBI}	2×1.5	MW
	P_{ICRH}	2×2.2	MW

capability of runaways to probe magnetic turbulence.

In summary, one of the biggest issues in plasma physics is the anomalous heat transport. Turbulent fluctuations in magnetic field could be one of the causes of this anomalous transport. Runaway transport is dominated by magnetic turbulence. Investigation of this runaway transport is a possible way to measure the magnetic turbulence level and scale size.

1.5 This thesis

This thesis deals with a detailed study of runaway transport. It is tried to find answers on the following questions:

- What is the runaway electron transport under different plasma conditions?
- How are scale size and level of magnetic turbulence derived from the runaway transport measurements?
- What is the contribution of magnetic turbulence to anomalous heat transport?

In TEXTOR-94, one has the unique capability to detect runaways in the plasma core by the synchrotron radiation measurements. With an infrared

camera viewing tangentially into the plasma in the direction of electron approach, poloidal projections of the radiation coming from the toroidal runaway beam are observed. From these measurements, time evolutions and radial profiles of runaway electron distribution can be derived.

First, the runaway transport in an Ohmic plasma (i.e. a plasma only heated by the plasma current) is estimated. Use is made of the measured synchrotron radiation evolutions and profiles. The profile measurements allow the determination of the radial profile of the diffusion coefficient. A model that prescribes the diffusion of test particles as a result of magnetic field line diffusion gives an estimate of the level of magnetic turbulence in an Ohmic plasma. Secondly, the runaway transport is studied in plasmas with different externally applied perturbations. The plasma is perturbed by the application of additional heating, either by means of injection of a neutral particle beam or by means of emittance of waves into the plasma that are resonant with the frequency with which ions gyrate around the magnetic field lines. Previous experiments [4] already showed that runaway confinement degrades with additionally applied heating. A systematic study presented in this thesis shows that the runaway confinement is energy dependent as can be expected from the energy dependent reduction in sensitivity to magnetic turbulence of higher energetic electrons due to a large orbit shift. In other experiments, the plasma is disturbed by injecting a small frozen hydrogen pellet or by shifting and compressing the plasma to the inner wall, which leads to the formation of magnetic islands. In those cases, the rather spectacular phenomenon of a runaway 'snake', a narrow toroidal runaway beam confined in a magnetic island, occurs. Finally, the results of these runaway transport measurements are discussed and interpreted in the frame of different models about transport due to magnetic fluctuations.

In the first part of this thesis, a short overview is given of the phenomenon of electron runaway, the theory and the method of the synchrotron radiation measurement are discussed. In chapter 4, it is investigated with help of simulation codes what radiation evolutions and the poloidal projections of synchrotron radiation look like in TEXTOR-94. The main work on runaway confinement is described in chapter 5, 6 en 7. Chapter 8 discusses a few topics that are too speculative for publication in a journal at this stage, but are worth a short presentation.

1.6 Publications

Journals

1. 'Diffusion of runaway electrons in TEXTOR-94', I.Entrop, N.J.Lopes Cardozo, R.Jaspers, K.H.Finken, Plasma Phys. and Contr. Fusion **40** (1998) 1513-1527
chapter 5
2. 'Runaway snakes in TEXTOR-94', I.Entrop, R.Jaspers, N.J.Lopes Cardozo, K.H.Finken, Plasma Phys. and Contr. Fusion **41** (1999) 377-398
chapter 7
3. 'Scale size of magnetic turbulence in tokamaks probed with 30 MeV electrons', I.Entrop, N.J.Lopes Cardozo, R.Jaspers, K.H.Finken, submitted to Phys. Rev. Letters
chapter 6
4. 'Runaway transport during additional heating in TEXTOR-94', I.Entrop, R.Jaspers, N.J.Lopes Cardozo, K.H.Finken, to be submitted to Plasma Phys. and Contr. Fusion
chapter 6
5. 'Control of runaway electron secondary generation by changing Z_{eff} ', I.M.Pankratov, R.Jaspers, K.H.Finken, I.Entrop, G.Mank, Nuclear Fusion **38** (1998) 279-286

Conference contributions

1. 'Runaway diffusion in TEXTOR-94', I.Entrop, R.Jaspers, K.H.Finken, N.J.Lopes Cardozo, Proc. 24th EPS on Contr. Fusion and Plasma Phys., Berchtesgaden (1997), Part IV, 1705-1708
2. 'Runaway snakes in TEXTOR-94', I.Entrop, R.Jaspers, N.J.Lopes Cardozo, K.H.Finken, Proc. 25th EPS Conf. on Contr. Fusion and Plasma Phys., Prague (1998) B090PR
3. 'Study of disruption generated runaway electrons in TEXTOR-94', R.Jaspers, I.M.Pankratov, I.Entrop, K.H.Finken, Proc. 25th EPS Conf. on Contr. Fusion and Plasma Phys., Prague (1998) B068PR

4. 'Secondary generation of runaway electrons and its detection in tokamak plasmas', I.M.Pankratov, R.Jaspers, K.H.Finken, I.Entrop, Proc. 26th EPS Conf. on Contr. Fusion and Plasma Phys., Maastricht (1999) P2.002

References

- [1] Wesson J 1987 *Tokamaks* Clarendon Press, Oxford
- [2] Giovanelli R G 1949 *Phil. Mag.* **40** 206
- [3] Finken K H, Watkins J G, Rusbüldt D, Corbett W J, Dippel K H, Goebel D M, Moyer R A 1990 *Nucl. Fusion* **30** 859
- [4] Jaspers R J E 1995 *Relativistic runaway electrons in tokamak plasmas*
PhD Thesis, Eindhoven University of Technology, The Netherlands

Chapter 2

Runaway electrons

This chapter summarizes the basic properties of runaway electrons. Generation processes, electron orbits, energy limits and transport properties are discussed. In [1], a specific study of the runaway electrons in TEXTOR is given. A more general review is given in e.g. [2].

2.1 Electron runaway

First, the phenomenon of electron runaway is treated in 1-dimensional phase space to define the basic runaway electron terminology. Later in this section, a 2-dimensional model is presented which is more accurate.

The phenomenon of electron runaway is a result of the toroidal electric field E in a tokamak. Electrons experience an accelerating electric force $F_e = eE$. On the other hand, electrons are slowed down by a drag force F_d . A (relativistic) derivation of the drag force [3], including electron-ion and electron-electron collisions, yields

$$F_d = -\frac{e^4 n_e \ln \Lambda}{4\pi \epsilon_0^2 m_0 v^2} \left(1 + \frac{Z_{\text{eff}} + 1}{\gamma} \right) \quad (2.1)$$

where e and m_0 are the electron charge and rest mass, n_e is the electron density, $\ln \Lambda$ the Coulomb logarithm, ϵ_0 the vacuum permittivity, v the electron velocity, $Z_{\text{eff}} \equiv \sum_i n_i Z_i^2 / n_e$ the effective charge of the ions with i the different ion species and $\gamma \equiv (1 - (v/c)^2)^{-1/2}$ the relativistic factor with c the speed of light. The first term in (2.1) accounts for the energy exchange in electron-electron collisions, the second term accounts for the pitch angle scattering (both due to the electron-ion and electron-electron collisions) and disappears for higher energies ($\gamma \gg 1$).

For a non-relativistic electron with $\gamma \rightarrow 1$, the collision frequency in a Maxwellian distributed plasma when no electric field is present follows from

$$\nu_e \equiv \frac{|dp/dt|}{p} = \frac{|F_d|}{\gamma m_0 v} = \frac{e^4 n_e \ln \Lambda (2 + Z_{\text{eff}})}{4\pi \epsilon_0^2 m_0^2 v^3} \quad (2.2)$$

In presence of an electric field, the effective collision frequency becomes $\nu_{e,\text{eff}} \equiv |dp/dt|/p = |eE + F_d|/\gamma m_0 v$. In a tokamak, the parameters E , n_e , T_e and Z_{eff} are usually of a value that $eE \ll F_d$, so that the collision frequency is $\nu_{e,\text{eff}} \approx |F_d|/\gamma m_0 v$. Balancing the drag force and electric force for the test electron yields a critical parallel velocity

$$v_{\text{crit}} = \sqrt{\frac{e^3 n_e \ln \Lambda (2 + Z_{\text{eff}})}{4\pi \epsilon_0^2 m_0 E}} \quad (2.3)$$

Electrons with a velocity $v > v_{\text{crit}}$ will be effectively accelerated and are called runaway electrons. These electrons have a (non-relativistic) kinetic energy of at least

$$W_{\text{crit}} = \frac{e^3 n_e \ln \Lambda (2 + Z_{\text{eff}})}{8\pi \epsilon_0^2 E} \quad (2.4)$$

The critical electric field for which a thermal electron with velocity $v_{\text{th}} = \sqrt{kT_e/m_0}$ (k the Boltzmann's constant and T_e the electron temperature) becomes a runaway electron, is

$$E_{\text{crit}} = \frac{e^3 n_e \ln \Lambda (2 + Z_{\text{eff}})}{4\pi \epsilon_0^2 m_0 v_{\text{th}}^2} \quad (2.5)$$

(which is about twice the Dreicer field [4] often encountered in literature). As long as the applied toroidal electric field is much smaller than this critical field, $\varepsilon \equiv E/E_{\text{crit}} \ll 1$, the distribution function of the electrons is approximately Maxwellian and only a small fraction of the electrons will run away. Note that several publications give a factor Z_{eff} instead of $(2 + Z_{\text{eff}})$ in the above given expressions for ν_e , v_{crit} , W_{crit} and E_{crit} , neglecting the electron-electron collisions in the derivation of the drag force (2.1).

For typical TEXTOR-94 parameters ($n_e = 10^{19} \text{ m}^{-3}$, $\ln \Lambda = 16$, $Z_{\text{eff}} = 2$, $E = 0.1 \text{ V/m}$), the critical velocity is $v_{\text{crit}}/c \approx 0.6$. This velocity corresponds to a critical energy of the order of 100 keV. Note that a value of $v_{\text{crit}}/c \approx 0.6$ corresponds to $\gamma \approx 1.25$ and that for this value of γ , the relativistically correct expression for kinetic energy, $W_{\text{crit}} = (\gamma - 1)m_0 c^2$, does not differ much from the above classical approximation. For the above mentioned TEXTOR-94 parameters and $T_e = 1.5 \text{ keV}$, an critical electric field of about 6 V/m is

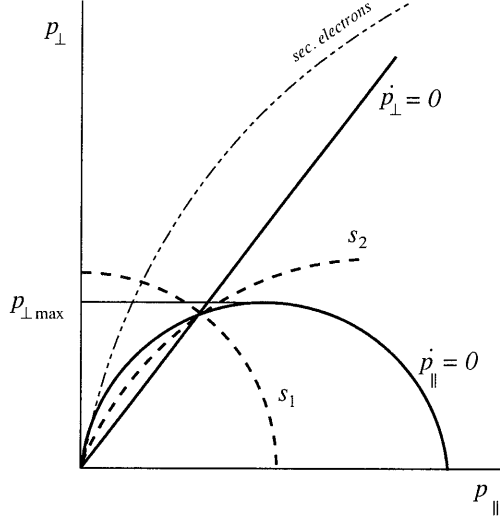


Figure 2.1: *Electron phase space; electrons with momentum above the separatrix s_1 will run away.*

calculated. Therefore, $\varepsilon \approx 0.02$, so in TEXTOR-94, the electron distribution indeed stays close to Maxwellian.

A 2-dimensional treatment of the electron runaway phenomenon is found in [5, 6]. The electron motion in phase space (p_\perp, p_\parallel) , with $p_\perp = \gamma m_0 v_\perp$ the perpendicular and $p_\parallel = \gamma m_0 v_\parallel$ the parallel electron momentum with respect to the magnetic field, is described by

$$\frac{dp_\parallel}{dt} = eE \left(1 - \frac{\gamma^2 p_\parallel p_{\text{cr}}^2}{(p_\parallel^2 + p_\perp^2)^{3/2}} \left(1 + \frac{Z_{\text{eff}} + 1}{\gamma} \right) \right) \quad (2.6)$$

$$p_\perp \frac{dp_\perp}{dt} = \frac{eE \gamma^2 p_{\text{cr}}^2}{p} \left(\left(1 + \frac{Z_{\text{eff}} + 1}{\gamma} \right) \frac{p_\parallel^2}{p^2} - 1 \right) \quad (2.7)$$

with total momentum $p \equiv \sqrt{p_\parallel^2 + p_\perp^2}$ and $p_{\text{cr}}^2 = (e^3 \ln \Lambda n_e m_0) / (4\pi \epsilon_0^2 E)$. The curves $dp_\parallel/dt = 0$ and $dp_\perp/dt = 0$ divide the phase space in 4 regions as shown in figure 2.1. They intersect at a saddle point. Also indicated in figure 2.1 are the two separatrices s_1 and s_2 . Electrons with initial momentum $(p_{\perp 0}, p_{\parallel 0})$ above separatrix s_1 will run away. It is clear that for small pitch angle, i.e. $p_\perp \ll p_\parallel$, the above expressions of electron motion in phase space lead to a force balance $|dp/dt| \approx |dp_\parallel/dt| = |eE + F_d| = 0$ with a drag force

as given by (2.1). The critical (parallel) electron velocity as given by (2.3) corresponds to the point where the curve $dp_{\parallel}/dt = 0$ intersects the p_{\parallel} -axis and where approximately $\gamma \rightarrow 1$. Figure 2.1 shows that also electrons with $v < v_{\text{crit}}$ can runaway, as long as their perpendicular momentum is non-zero.

2.2 Generation

In theory, two runaway electron generation mechanisms are known. In the following, the basic formulas concerning these generation processes are presented.

Primary generation

In section 2.1, the phenomenon of electron runaway in a tokamak plasma has been explained. The production rate of the runaway electrons is calculated from a solution of the electron distribution function using the Fokker-Planck equation. This equation gives a kinetic description of the plasma including multiple small angle collisions (large impact parameters). The diffusion rate in velocity space of electrons with velocities around $v = v_{\text{crit}}$ determines the creation rate. The runaway production due to the diffusion in velocity space is referred to as primary generation. It is found that the electron flow into the runaway region, i.e. the growth of the distribution with $v > v_{\text{crit}}$, is given by [7–10]

$$\frac{dn_{\text{r,pr}}}{dt} = \lambda_r \nu_e n_e \quad (2.8)$$

where ν_e is the collision frequency of thermal electrons¹ (2.2) and n_e the electron density and where λ_r is the runaway birth rate

$$\lambda_r = K(Z_{\text{eff}}) \varepsilon^{-3(Z_{\text{eff}}+1)/16} \exp\left(-\frac{1}{4\varepsilon} - \sqrt{\frac{Z_{\text{eff}}+1}{\varepsilon}}\right) \quad (2.9)$$

The birth rate is a strongly exponential function of $\varepsilon \equiv E/E_c$. Here, the critical electric field E_c is defined without any Z_{eff} -dependence, unlike (2.5), as $E_c = e^3 \ln \Lambda n_e / (4\pi \epsilon_0^2 m_e v_{\text{th}}^2)$ to give the birth rate an explicit Z_{eff} -dependence. $K(Z_{\text{eff}})$ is a weak function of Z_{eff} (see [10]: $K(1) = 0.32$, $K(2) = 0.43$).

For highly relativistic runaways ($v \approx c$, $\gamma \gg 1$), the drag force (2.1) is approximately constant. This limits the runaway production when $E \leq$

¹Here, it is assumed that the electron velocity distribution is close to a Maxwellian distribution despite the induced electric field. Because in TEXTOR-94, $\varepsilon \ll 1$, this assumption is justified.

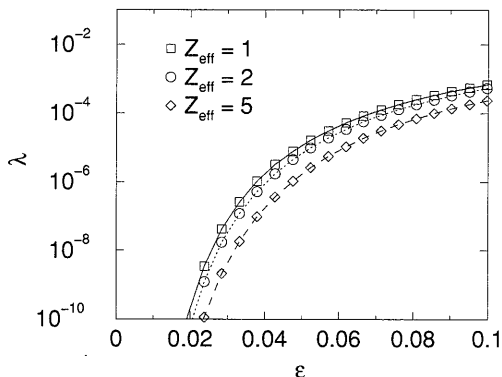


Figure 2.2: Runaway birth rate as function of the parameter $\varepsilon \equiv E/E_{\text{crit}}$ for different values of Z_{eff} . The lines show the non-relativistic birth rate, the symbols show the relativistic birth rate.

$F_d/e \approx 8 \times 10^{-3}$ V/m (with $n_e \approx 1 \times 10^{19}$ m $^{-3}$). In other words, since in TEXTOR-94 during steady state operation $E \approx 0.1$ V/m, no runaway production occurs if $n_e \geq 4\pi\epsilon_0^2 m_0 c^2 E/e^3 \ln\Lambda \approx 1.2 \times 10^{20}$ m $^{-3}$. This density is, however, higher than the Ohmic density limit. Nevertheless, the effect is noticeable at lower densities as a reduction of the runaway production. The relativistic birth rate is given by

$$\lambda_{\text{r,rel}} = \lambda_{\text{r}} \exp\left(-\frac{T_e}{m_0 c^2} \left(\frac{\varepsilon^2}{8} + \frac{2\varepsilon^{3/2}}{3} \sqrt{1 + Z_{\text{eff}}}\right)\right) \quad (2.10)$$

which gives for TEXTOR-94 parameters a birth rate that does not significantly differ from the non-relativistic birth rate (2.9). Figure 2.2 shows the non-relativistic (lines) and the relativistic (symbols) birth rate as function of ε for different values of Z_{eff} .

Secondary generation

Apart from the primary generation, a second generation mechanism of runaways exist [5, 11, 12]. Already existing runaway electrons can kick thermal electrons into the runaway regime by close Coulomb collisions (small impact parameter). Note that in the derivation of the runaway birth rate λ_{r} only the small angle collisions were taken into account. The energy-differential cross section for a Coulomb collision between a fast electron with velocity v

and an electron with velocity $v_{\text{th}} \ll v$ is given by [12]

$$\frac{d\sigma}{dW} = \frac{e^4}{8\pi\epsilon_0^2 m_0 v^2 W^2} \quad (2.11)$$

where W is the energy of the secondary electron. The increase of the runaway number due to this secondary process is given by

$$\frac{dn_{\text{r,sec}}}{dt} = n_{\text{r}} n_e v \int_0^\infty P(W') \frac{d\sigma}{dW'} dW' \quad (2.12)$$

where $P(W')$ is the probability that an electron that has energy W' after the collision, becomes a runaway electron. In [12], the simple model $P(W') = 0$ for $W' < W_{\text{crit}}$ and $P(W') = 1$ for $W' \geq W_{\text{crit}}$ is used. This model gives

$$\frac{dn_{\text{r,sec}}}{dt} = \frac{n_{\text{r}} e E}{m_0 v \ln \Lambda (2 + Z_{\text{eff}})} \quad (2.13)$$

which is more conveniently written as

$$\frac{dn_{\text{r,sec}}}{dt} = \frac{n_{\text{r}}}{t_0} \quad (2.14)$$

where t_0 is the avalanche time within which a runaway electron creates another, secondary, runaway electron. This process is referred to as secondary generation. Note that this secondary generation is independent of the electron density n_e .

In the previous section, a more detailed treatment of electron runaway was shortly discussed. Figure 2.1 showed the region in two-dimensional phase space at which electrons will run away. The secondary electrons are found in phase space on ellipses with major axis equal to the momentum of the incident high energetic runaway. An example is shown in figure 2.1. Most of the knocked-out electrons have relatively large perpendicular momentum, $p_{\perp} \gg p_{\parallel}$. A determination of the runaway region of the knocked-out electrons follows from the inequality $p_{\perp} > p_{\perp \text{crit}}$ with $p_{\perp \text{crit}} \approx p_{\perp \text{max}}$ which is the maximum value of perpendicular momentum in the curve $dp_{\parallel}/dt = 0$. This last approximation is valid for $Z_{\text{eff}} \leq 10$ (in TEXTOR-94, typically $Z_{\text{eff}} = 2 - 4$). In that approximation, the avalanche time t_0 is given by [13]

$$t_0 = \frac{\sqrt{12} \ln \Lambda m_0 c (2 + Z_{\text{eff}})}{9eE} \quad (2.15)$$

Because the secondary electrons have $p_{\perp} \gg p_{\parallel}$, there is the possibility of particle trapping. Trapped particles do not participate in the acceleration

until they are converted into passing electrons as a result of distant collisions with thermal particles. Hence, the trapping may increase the above value of t_0 .

In [1], the runaway density was calculated analytically as a function of time, including primary and secondary generation and runaway losses,

$$n_r(t) = \lambda_r \nu_e n_e t_{\text{eff}} (\exp(t/t_{\text{eff}}) - 1) + n_r(0) \exp(t/t_{\text{eff}}) \quad (2.16)$$

An effective time t_{eff} was introduced, $t_{\text{eff}}^{-1} = t_0^{-1} - \tau^{-1}$, where τ is the runaway confinement time. A small t_{eff} means a relatively strong exponential rise in n_r . When t_0 and τ are such that t_{eff} becomes negative, n_r decays in time.

It is expected that the runaway generation is concentrated in the center of the plasma, because the temperature profile is more peaked than the density profile. In [1], the width of the runaway creation zone is estimated using different parametric forms for the T_e - and n_e -profiles, e.g. profiles as follow from the profile consistency principle [14] that have been shown to describe the experimental tokamak T_e and n_e profiles well: $T_e = T_e(0)(1 + q_a(r/a)^2)^{-4/3}$ and $n_e = n_e(0)(1 + q_a(r/a)^2)^{-2/3}$ with q_a the edge safety factor. It is found that in that approximation for typical TEXTOR-94 parameters, the creation zone has a half width at half maximum (HWHM) of approximately 7 cm.

2.3 Orbits

The orbit of an electron in a tokamak is given in a toroidal coordinate system². Unit vectors in toroidal, poloidal and vertical direction are denoted by $\hat{\phi}$, $\hat{\vartheta}$ and \hat{z} as shown in figure 2.3. The direction of the helical magnetic field in this coordinate system is approximately given by $(r/R_0 q(r))\hat{\vartheta} + \hat{\phi}$ where $q(r)$ is the safety factor which is a function of radial position³ because of the non-uniform induced current density in tokamaks. For a parabolic current density profile, a parabolic magnetic q -profile is found

²The relation between toroidal coordinates (r, ϑ, ϕ) and Cartesian coordinates (x, y, z) is

$$\begin{aligned} \hat{r} &= -\cos\vartheta\cos\phi\hat{x} - \cos\vartheta\sin\phi\hat{y} + \sin\vartheta\hat{z} \\ \hat{\vartheta} &= \sin\vartheta\cos\phi\hat{x} + \sin\vartheta\sin\phi\hat{y} + \cos\vartheta\hat{z} \\ \hat{\phi} &= -\sin\phi\hat{x} + \cos\phi\hat{y} \end{aligned}$$

³Actually, q is also a function of ϑ . The field lines at the inner side of the torus (high field side (HFS)) make a smaller angle with the equatorial plane than those at the outer side. This effect is not taken into account here.

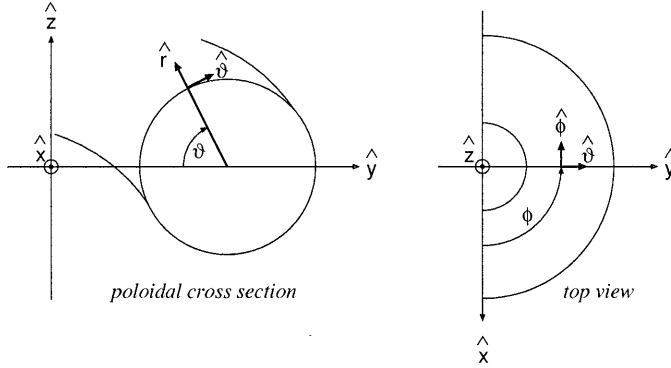


Figure 2.3: Cartesian (x, y, z) and toroidal (r, ϑ, ϕ) coordinate systems

$q(r) = q_0 + (q_a - q_0)(r/a)^2$ with q_0 and q_a the safety factor at the magnetic axis and at the plasma edge.

The electron orbit in a tokamak plasma is a superposition of three different motions. First, the electron gyrates around its guiding center, i.e. the center of mass of the electron averaged over the gyration motion, with a cyclotron frequency

$$\omega_{ce} = \frac{eB}{\gamma m_0} \quad (2.17)$$

and Larmor radius

$$\rho_{e,L} = \frac{\gamma m_0 v_{\perp}}{eB} \quad (2.18)$$

where B is the magnetic field strength and $v_{\perp} = \theta v_{\parallel}$ the perpendicular electron velocity with respect to the magnetic field direction. The velocity due to this gyration motion is given in the toroidal coordinate system by

$$v_{\perp}(\cos\alpha \hat{r} + \sin\alpha(\hat{\vartheta} - \frac{r}{q(r)R_0} \hat{\phi})) \quad (2.19)$$

where the angle α is the phase angle of the cyclotron gyration and given by $\dot{\alpha} = -\omega_{ce}$. Secondly, the guiding center of the electron follows the helicity of the magnetic field lines

$$\mathbf{v}_{gc} = v_{\parallel}(\frac{r}{R_0 q(r)} \hat{\vartheta} + \hat{\phi}) + v_z \hat{z} \quad (2.20)$$

where v_z results from the vertical magnetic field that is needed in tokamaks for stability reasons. Finally, the test electron orbit is displaced from the

magnetic field surface due to curvature and gradient magnetic field drifts. The drift velocity is given by

$$v_d = \frac{1}{R_m \omega_{ce}} (v_{\parallel}^2 + \frac{1}{2} v_{\perp}^2) \quad (2.21)$$

and points in direction of $\mathbf{R}_m \times \mathbf{B}/(R_m B) \approx \hat{\mathbf{z}}$ where \mathbf{R}_m is the radius of curvature of the magnetic field. The $\mathbf{E} \times \mathbf{B}$ drift can be neglected because it is generally much smaller than the other terms.

In summary, the total electron velocity vector can be written in the form [15]

$$\mathbf{v} = v_{\parallel} \left(\frac{r}{R_0 q(r)} \hat{\boldsymbol{\theta}} + \hat{\boldsymbol{\phi}} \right) + v_{\perp} (\cos \alpha \hat{\mathbf{r}} + \sin \alpha (\hat{\boldsymbol{\theta}} - \frac{r}{q(r) R_0} \hat{\boldsymbol{\phi}})) + (v_z + v_d) \hat{\mathbf{z}} \quad (2.22)$$

The position of the electron is given by

$$\mathbf{R} = R_0 (\cos \phi \hat{\mathbf{x}} + \sin \phi \hat{\mathbf{y}}) + r \hat{\mathbf{r}} + \frac{v_{\perp}}{\omega_{ce}} (\cos \alpha (\hat{\boldsymbol{\theta}} - \frac{r}{q(r) R_0} \hat{\boldsymbol{\phi}}) - \sin \alpha \hat{\mathbf{r}}) \quad (2.23)$$

The drift velocity v_d results, for runaways with $v_{\parallel} \gg v_{\perp}$, in an outward shift of the runaway orbit surface away from the magnetic field surface. This drift orbit displacement is given in first-order approximation by

$$d \approx \frac{\bar{q} \gamma m_0 v_{\parallel}}{eB} \approx \frac{\bar{q} W_r}{ecB} \quad (2.24)$$

where W_r is the runaway energy and \bar{q} the average safety factor of the shifted drift surface. In [16,17], a Hamiltonian description of the drift orbit topology of relativistic particles in a tokamak is given. The rotational transform ω_D of the particle orbit, the (dimensionless) minor radius of the drift orbit ρ_D and the (dimensionless) outward shift of the drift orbit δ_D are expressed in the variable I and the dimensionless energy parameter λ

$$\omega_D(I, \lambda) = \frac{1}{q(I)} + O(\lambda) \quad (2.25)$$

$$\rho_D(I, \lambda) = (2I)^{1/2} + O(\lambda) \quad (2.26)$$

$$\delta_D(I, \lambda) = \lambda q(I) + O(\lambda^2) \quad (2.27)$$

Here, $\lambda = \gamma m_0 v_{\parallel} / eB R_0$ is a measure of the particle energy and $I = \frac{1}{2}(r/R_0)^2 + O(\lambda)$ is a canonical momentum introduced in the Hamiltonian description, which is proportional to the toroidal magnetic flux for $\lambda = 0$. $q(I)$ is the safety factor of the magnetic field at the position of the drift orbit, whereas $q_D(I, \lambda) \equiv 1/\omega_D(I, \lambda)$ denotes the structure of the drift orbit itself. When

a parabolic q -profile is assumed, $q(r) = q_0 + (q_a - q_0)(r/a)^2$, we can write $q(I) = q_0 + 2(q_a - q_0)I(R_0/a)^2$ because of the characteristic $I = \frac{1}{2}x^2 + O(\lambda)$. It is not important to know the exact dependences of I on physical quantities. When the topology of the drift orbit $q_D \equiv 1/\omega_D$ and the energy of the particles λ is known, the corresponding $I = I_{q_D}(\lambda)$ can be calculated from (2.25) and the result can be used to determine ρ_D and δ_D with (2.26) and (2.27).

The classical view on drift orbits is obtained by taking only the zeroth order terms in λ in rotational transform (2.25) and drift orbit radius (2.26), and by taking the first order term in the shift (2.27). With $I = \frac{1}{2}(r/R_0)^2$, it is indeed found $q_D = q$, $\rho_D = r/R_0$ and $\delta_D = d/R_0$, i.e. the drift orbit topology is equal to the magnetic field topology apart from a shift d . Higher order terms in energy λ make the real behavior of the drift orbits more complex. First, the rotational transform decreases, that is q_D increases, with increasing particle energy. The drift orbit radius is almost constant during the acceleration. As a consequence, the minor radius of the drift surface with a fixed q_D is smaller than the minor radius of the magnetic field surface with $q = q_D$ from which the particle started with zero energy. Secondly, the shift of the drift orbit surface from the corresponding magnetic surface is larger than the shift that would follow from the classical view.

2.4 Energy limits

An electron with a velocity $v > v_{\text{crit}}$ is effectively accelerated. The energy that a runaway electron reaches can be limited by the synchrotron radiation, the drift orbit radius and shift, the flux swing, the magnetic field ripple and instabilities.

Synchrotron radiation

Because of the toroidal acceleration of the runaway electrons, they emit electromagnetic radiation. The change in energy W_r for one runaway electron is determined by the difference between the amount of power that is absorbed from the accelerating electric field, which is approximately $P_E \approx ecV_{\text{loop}}/2\pi R_0$, and the amount of power lost by radiation $P \approx 2m_0c^3r_e\gamma^4/3R_c^2$. The energy loss due to friction can be neglected in comparison with the radiation loss. Here, V_{loop} is the loop voltage, $r_e = e^2/4\pi\epsilon_0m_0c^2$ the classical Thomson electron radius, γ the relativistic factor and R_c can be approximated by [18]

$$\frac{1}{R_c} \approx \frac{1 - \theta^2}{R_0} + \frac{eB\theta}{\gamma m_0 c} \quad (2.28)$$

with $\theta = v_{\perp}/v_{\parallel}$ the runaway pitch angle. From

$$\frac{dW_r}{dt} = m_0 c^2 \frac{d\gamma}{dt} = P_E - P \quad (2.29)$$

the energy evolution of one runaway electron is calculated. The maximum energy that can be reached is given by the equilibrium $P_E - P = 0$. For the TEXTOR-94 parameters and the experimentally observed pitch angle $\theta = 0.1$ [1], the equilibrium is reached at $\gamma_{\text{eq}} \approx 60$ which corresponds with an energy of about $W_r \approx 30$ MeV. Note that for this energy and pitch angle, and $B = 2.2$ T, $v_{\parallel} \approx c$, it follows $\omega_{ce} \approx 1$ GHz and $\rho_{e,L} \approx 5$ mm. Furthermore, from (2.25), (2.26) and (2.27), it follows that for the TEXTOR-94 runaway energy range the correction on the drift surface shift δ_D due to higher order energy terms is negligible. These higher order energy terms, however, do have an effect on $q_D \equiv 1/\omega_D$ and the drift surface radius ρ_D in this energy range. In section 3.1, the synchrotron radiation emitted by runaway electrons is discussed in detail.

Drift orbits

Runaways can be confined within the tokamak as long as the sum of their orbit shift and drift orbit radius is smaller than the minor radius a . In zero-order approximation, the drift orbit radius is equal to the radius of the magnetic surface with $q = q_D$, so an energy limit for a runaway with its orbit on the magnetic axis, follows from the shift (2.24) $W_{\text{max}} = aecB/q_a \approx 80$ MeV where $q_a = 3.8$ for a plasma current $I_p = 350$ kA and $B = 2.2$ T. In section 2.3, we have seen that the drift orbit radius and shift are in fact a function of the particle energy parameterized by λ and of the canonical momentum I . The minor radius of a drift surface with a fixed q_D becomes smaller than the minor radius of the magnetic surface with $q = q_D$ with increasing particle energy. This shrinking of drift surface radius goes faster than the increase in drift orbit shift. Eventually the drift surface falls entirely within the magnetic flux surface. Hence, the energy limit is not so much determined by the drift orbit shift but more by the decreasing drift surface radius. The energy at which a drift surface with $q_D = 1$ ceases to exist (for $I_p = 350$ kA, i.e. $q_a = 3.8$), is $W_{\text{max}} \approx 60$ MeV. For higher q_D and for lower q_a , this critical energy is larger.

Acceleration time

The energy that a runaway can reach depends on the time that is available for its acceleration. When no radiation losses are considered in (2.29), a

maximum energy follows from

$$W_{\max}(t) = \int_0^t \frac{dW}{dt'} dt' = \frac{ec}{2\pi R_0} \int_0^t V_{\text{loop}}(t') dt' = \frac{ec}{2\pi R_0} \Phi(t) \quad (2.30)$$

where $\Phi(t)$ is the flux swing applied to the plasma. This leads to $W_{\max}(t) = 27\Phi(t)$ MeV. The radiation limit already occurs at 30 MeV, so only when $\Phi(t) < 1.1$ Wb, it will determine the maximum runaway energy. This value is already reached at approximately 1 s whereas the typical duration of a TEXTOR-94 discharge is 6 s.

Magnetic field ripple

The toroidal magnetic field is generated by a finite number of coils N . This slightly modulates the magnetic field and runaways experience this modulation at frequencies $\omega_{\text{ripple}} = nNc/R_0$ with n the harmonic number. In [19], a mechanism is described in which the relativistic electron cyclotron frequency (2.17) is resonant with the magnetic field ripple. A resonance occurs for $\gamma_{\text{res}} = eBR_0/nNm_0c$ which corresponds to an energy $W_{\text{res}} = 70/n$ MeV. The second and higher harmonics are in the same range of energy as the radiation limit. According to [19], the strength of the resonance decreases with increasing harmonic number. In TEXTOR-94, only the second harmonic is expected to be of any importance in blocking the energy increase of runaways.

When a resonance occurs, the electrons are scattered in pitch angle θ . Because of the increase in θ , the power radiated per electron P will increase. This increased P leads to a lower radiation limit. In [1], this pitch angle scattering effect is estimated by a Monte Carlo simulation. It was found that an effective energy blocking due to the increase in θ occurs already before the resonance energy W_{res} . For $n = 2$, a radiation equilibrium is found at about 25 MeV with a pitch angle distribution centered around $\theta = 0.13$. Maximum energy that can be reached is about 30 MeV, where $\theta = 0.10$.

Instabilities

The free energy in the plasma due to the non-Maxwellian component in the electron velocity distribution can be exchanged between resonant electrons and plasma oscillations. Above a certain threshold, instabilities can be excited which can limit either the runaway energy or the runaway confinement.

The general resonance condition is $\omega_k - n\omega_{ce} = k_{\parallel}v_{\parallel}$ with ω_k the wave frequency, k_{\parallel} the wave number parallel to the magnetic field, n the harmonic number, ω_{ce} the electron cyclotron frequency and v_{\parallel} the electron velocity (parallel to the magnetic field). When $n = 0$ the interaction is called

Cerenkov resonance. The wave grows unstable if the electron distribution function has a positive slope, $df(v)/dv > 0$. This leads to an energy exchange between the electrons and the wave. When $df(v)/dv < 0$, the wave will be damped (Landau damping). For negative n , the anomalous Doppler resonance, longitudinal energy of the electron is converted into transverse energy. For positive n , the interaction is called normal Doppler resonance. These waves convert transverse energy of the electron into longitudinal energy. Because of the comparatively small perpendicular energy of runaways, runaways are not expected to excite unstable waves by this last resonance.

An example of an energy limiting instability is the so-called Parail-Pogutse instability [20]. The anomalous Doppler resonance is responsible for an unstable interaction between accelerating runaways exceeding some critical energy W_{beam} and plasma waves. The excited waves are simultaneously damped on the thermal electrons at the Cerenkov resonance. When the damping saturates (which happens when the distribution function at the thermal resonance becomes flat), the growth rate of the waves increases and runaway electrons are pitch angle scattered by the anomalous Doppler mechanism. The mechanism has a repetitive character because after the energy isotropization, the runaway electrons are accelerating exceeding W_{beam} again. The range of runaway energies for which this instability occurs, is 0.1-1 MeV. The synchrotron measurements as described in this thesis require the presence of runaway electrons with an energy of about 20 MeV. Plasma parameters in typical runaway discharges are chosen in such a way that these instabilities at lower energy do not occur.

In [1], the observation of an instability at higher energy is presented. The infrared pictures show an increase in pitch angle $\theta = v_{\perp}/v_{\parallel}$ within a few hundred microseconds, which gave this instability the name 'fast pitch angle scattering event' (FPAS). The most plausible explanation of this FPAS is that due to a change in plasma conditions, the Parail-Pogutse instability occurs at which a broad spectrum of waves is excited, among which lower hybrid waves. In [1], it was estimated that runaway electrons of 23 MeV energy will be pitch angle scattered by these lower hybrid waves. Experimentally, it is determined, that the pitch angle scatters from about 0.1 to a value of 0.17. This will decrease the radiation limit to 20 MeV. The FPAS instability is discussed in more detail in chapter 8.

2.5 Transport

The experimentally observed cross field energy transport via electrons is up to two orders of magnitude larger than predicted by neoclassical theory (col-

lisional transport in toroidal geometry). This enhancement in transport is called anomalous transport and is caused by turbulence, of either electrostatic or magnetic nature. In case of electrostatic turbulence, the magnetic field topology is intact and fluctuating electric field drive particle fluxes. In the picture of magnetic turbulence, magnetic field fluctuations destroy the topology of nested surfaces. Field lines can make radial excursions and particles moving along the field lines show an enhanced radial transport. Because it is assumed, that runaway electrons are mainly sensitive to the magnetic turbulence, a thorough study of the runaway transport under different plasma conditions could lead to conclusions on the role of magnetic turbulence in anomalous transport. Before going into that detailed study, a short overview of these transport mechanisms is given below.

Collisions

The collisional diffusion of particles can be regarded as a random walk process and is characterized by a coefficient D determined by a radial step size Δx and a time τ equal to the collision time of the particle

$$D = \frac{\langle(\Delta x)^2\rangle}{\tau} . \quad (2.31)$$

In classical transport theory, a plasma in a cylindrical system is considered. For electrons, the radial step size is then equal to the electron Larmor radius $\rho_{e,L}$ (2.18) with which the electrons gyrate around the magnetic field lines. The electron collision time τ_e follows from the collision frequency (2.2) $\tau_e = 1/\nu_e$.

In neoclassical theory, the toroidal geometry of a tokamak is included. The main consequence of the toroidal geometry is the existence of 'banana' orbits of electrons. Because the toroidal magnetic field strength decreases with increasing major radius, the inner side of the torus functions as a magnetic mirror and electrons can be trapped on the outboard side. Such trapped electrons carry out a banana-shaped orbit. In a toroidal system the appropriate radial step length is the width of the banana orbit, which is typically one order of magnitude larger than $\rho_{e,L}$.

In the regime of low collisionality, the electrons are free to complete their banana orbits. The typical distance along a field line from the inside to the outside of the torus is $\sim Rq$ with R major radius and q safety factor. Hence, this regime of low collisionality is determined by collision times $\tau > Rq/(v_{th}\epsilon^{3/2})$ where v_{th} is the (thermal) electron velocity and $\epsilon \equiv r/R$. Because the electrons can complete their banana orbits, this regime is called the banana regime. In a plasma with high collisionality, a particle suffers a

collision before it moves the typical distance along a field line from the inside to the outside of the torus. The particles cannot carry out banana-orbits. Typical collision time is $\tau < Rq/v_{\text{th}}$. The diffusion coefficient is the classical one increased by a factor $(1 + q^2)$. This regime is called the Pfirsch-Schlüter regime. The regime of intermediate collisionality, $Rq/v_{\text{th}} < \tau < Rq/(v_{\text{th}}\epsilon^{3/2})$ is referred to as plateau regime. The diffusion coefficient is independent of collisions and matches the coefficient found with low and high collisionality at the appropriate collision frequencies.

Because for high energetic runaways in TEXTOR-94, $\rho_{e,L} \approx 5$ mm and $\tau \approx \nu_{e,\text{rel}}^{-1} \approx 10$ s (where $\nu_{e,\text{rel}}$ is estimated from equation (2.2) with $\gamma = 60$), the order of magnitude of the classical runaway diffusion coefficient $D_{r,c} = \rho_{e,L}^2/\tau \sim 10^{-6}$ is expected. Runaway collisionality is low, but runaway electrons can not be trapped because of their high parallel velocity and, hence, they do not carry out banana orbits. Because of the curved magnetic field lines in toroidal geometry, runaway electrons experience an outward drift orbit displacement, that is typically one order of magnitude larger than the Larmor radius. When this orbit shift is taken as a measure of the typical neoclassical step length (although it is only an overall outward shift), the neoclassical runaway diffusion coefficient is estimated $D_{r,\text{neo}} \sim 10^{-4}$ which is still very small.

Electrostatic fluctuations

Apart from collisions, also fluctuations in the electric field can decorrelate particles from the magnetic field lines by fluctuating $\mathbf{E} \times \mathbf{B}$ drifts. Fluctuating electric fields \tilde{E} , perpendicular to the magnetic field, give rise to a drift velocity $\tilde{v} \sim \tilde{E}/B$. In a random walk estimate, the drift velocity causes a displacement $\Delta x \approx \tilde{v}\tau_{\text{trans}}$ with transit time $\tau_{\text{trans}} = \pi qR/v_{\parallel}$. This leads to a diffusion coefficient

$$D = \frac{\langle(\Delta x)^2\rangle}{\tau} \approx \tilde{v}^2\tau_{\text{trans}} \approx \frac{\pi qR}{v_{\parallel}} \left(\frac{\tilde{E}}{B}\right)^2. \quad (2.32)$$

When the anomaly of the measured heat diffusivity in TEXTOR-94, $\chi_e \approx 1$ m²s⁻¹, is assumed to be caused only by electrostatic turbulence, runaway transport due to these electric field fluctuations is at least a factor $c/v_{\text{th}} \approx 30$ smaller. The runaway diffusion coefficient due to electrostatic turbulence is then $D_{r,\text{es}} \approx 0.03$ m²s⁻¹.

Magnetic fluctuations

Electrons follow the magnetic field lines, when collisions and the drift motion due to the magnetic field gradient and curvature are neglected. When these

field lines 'diffuse', the particles that follow those field lines diffuse as well. Rechester and Rosenbluth [21] give a quasilinear estimate for the diffusion coefficient of the field lines in a fully stochastic, static magnetic field B

$$D_M \sim L_{\parallel} \left(\frac{\tilde{B}}{B} \right)^2 \quad (2.33)$$

where $L_{\parallel} \approx \pi q R$ is the correlation length of the fluctuations along B and \tilde{B} is the radial magnetic field fluctuation. The diffusion coefficient for electrons is, according to [21], proportional to the parallel velocity, $D \sim v_{\parallel} D_M$. Hence, when the anomalous heat conductivity, $\chi_e \sim 1 \text{ m}^2\text{s}^{-1}$, is assumed to be caused only by magnetic turbulence, the runaway diffusion coefficient due to magnetic turbulence is $D_{r,m} \sim 30 \text{ m}^2\text{s}^{-1}$.

In [22], it is shown that magnetic field lines in a stochastic region do not make a Gaussian random walk as is assumed in [21]. Furthermore, in typical tokamak conditions, magnetic shear can not be neglected in models of transport in chaotic magnetic fields as is usually done. Test particle transport treated in a sheared and non-Gaussian behavior of magnetic field lines shows a smaller scaling with velocity than the treatment in [21]. It is calculated $D \sim v_{\parallel}^{1/3} v_{\perp}^{1/3} D_M$. This model gives an estimate of the runaway diffusion coefficient $D_{r,m} \sim 3 \text{ m}^2\text{s}^{-1}$ when it is assumed that χ_e is determined completely by magnetic turbulence.

Several processes are thought to reduce the diffusion of relativistic runaways by magnetic field fluctuations. In e.g. [23, 24], the effect of the drift orbit displacement of the electrons is discussed. If the drift orbit shift d is large compared to the typical scale size of the magnetic turbulence, $d > \delta$, the effect of the turbulence on the runaway transport is small. With increasing drift orbit displacement, i.e. with increasing energy, the runaway electron is less sensitive to the turbulence, which results in a reduction in transport due to the magnetic turbulence. In [23], this reduction is expressed in an energy dependent drift parameter Υ , so that the diffusion coefficient is written as $D \sim \Upsilon v_{\parallel} D_M$. This drift parameter is calculated as function of the ratio between orbit shift and typical mode width d/δ . In [24], the ratio between the runaway confinement time, τ_r , including the effect of drift orbit averaging, and the confinement time without this effect, $\tau_{r,0}$, is numerically calculated as function of the ratio d/δ . The relation is approximated by

$$\frac{\tau_r}{\tau_{r,0}} = \left(1 + 1.1 \frac{d}{\delta} \right)^{5.7} \quad (2.34)$$

which is plotted in figure 2.4. In [24], the driftless case is calibrated to thermal

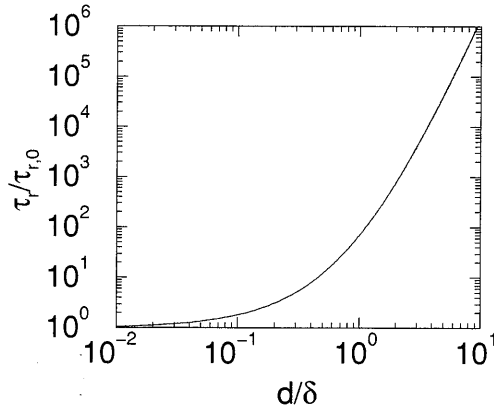


Figure 2.4: Runaway confinement time τ_r as function of the ratio between the orbit shift d and the typical size of magnetic turbulence δ , normalized to the 'driftless' case, $\tau_{r,0}$. This curve is an approximation of the numerically calculated curve shown in figure 2 in [24].

transport with a correction factor for velocity, $\tau_{r,0} = \tau_E v_{th}/c$. In chapter 6, the drift orbit averaging is discussed more extensively.

Most models of test particle transport describe the transport in chaotic magnetic fields. In a tokamak, however, the magnetic field can consist of regions with good magnetic surfaces and regions with a slightly perturbed magnetic field. In [25], the transport properties of fast electrons in such a mixed magnetic field topology was studied. It was found, that transport of fast electrons is already considerably reduced when only a small number of good magnetic confinement regions are present.

References

- [1] Jaspers R J E 1995 *Relativistic runaway electrons in tokamak plasmas* PhD Thesis, Eindhoven University of Technology, The Netherlands
- [2] Knoepfel H, Spong D A 1979 *Nucl. Fusion* **19** 785
- [3] Fussmann G 1979 *Nucl. Fusion* **19** 327
- [4] Dreicer H 1959 *Phys. Rev.* **115** 238
- [5] Besedin N T, Pankratov I M 1986 *Nucl. Fusion* **26** 807
- [6] Pankratov I M, Jaspers R, Finken K H, Entrop I 1999 *Proc. of the 26th EPS Conf. on Contr. Fusion and Plasma Phys.* Maastricht, P2.002
- [7] Kulsrud R M, Sun Y C, Winsor N K, Fallon H A 1973 *Phys. Rev.Lett.* **31** 690
- [8] Connor J W, Hastie R J 1975 *Nucl. Fusion* **15** 415
- [9] Gurevich A V 1961 *Sov. Phys. JETP* **21** 931
- [10] Cohen R H 1976 *Phys. Fluids* **19** 239
- [11] Parail V V, Pogutse O P 1986 *Reviews of Plasma Physics* **11** Consultants Bureaus, New York
- [12] Jayakamur R, Fleischmann H H, Zweben S J 1992 PPPL-2849
- [13] Pankratov I M, Besedin N T 1996 *Proc. of the 23th Conf. on Contr. Fusion and Plasma Phys.* (Kiev) Part I 279
- [14] Schüller F C, Schram D C, Konings J et al 1991 *Proc. of the 18th EPS Conf. on Contr. Fusion and Plasma Phys.* Berlin, Vol. 15C-IV 185
- [15] Pankratov I M 1996 *Plasma Phys. Rep.* **22** 535
- [16] de Rover M, Lopes Cardozo N J, Montvai A 1996 *Phys. Plasmas* **3** 4468;
- [17] de Rover M, Lopes Cardozo N J, Montvai A 1996 *Phys. Plasmas* **3** 4478
- [18] Russo A J 1991 *Nucl. Fusion* **31** 117
- [19] Laurent L, Rax J M 1989 EUR-CEA-FC-1374
- [20] Parail V V, Pogutse O P 1978 *Nucl. Fusion* **18** 303

- [21] Rechester A B, Rosenbluth M N 1978 *Phys. Rev. Lett.* **40** 38
- [22] de Rover M, Schilham A M R, Montvai A, Lopes Cardozo N J 1999 *Phys. Plasmas* **6** 2443
- [23] Myra J R, Catto P J 1992 *Phys. Fluids* **B4** 176
- [24] Mynick H E, Strachan J D 1981 *Phys. Fluids* **24** 695
- [25] Hegna C C, Callen J D 1993 *Phys. Fluids* **B5** 1804

Chapter 3

Runaway detection

In TEXTOR-94, runaway electrons are detected by measurement of the synchrotron radiation that they emit. This chapter presents the theory of synchrotron radiation. It is discussed how the synchrotron radiation is observed in TEXTOR-94. Other runaway diagnostics are shortly mentioned.

3.1 Synchrotron radiation

A brief summary of synchrotron radiation is given in a classical treatment [1–4]. Quantum effects do not come into play for electrons with energies less than 200 MeV [4]. This energy is far beyond the maximum that runaways can reach in TEXTOR-94. Hence, the classical treatment is justified.

Radiation from a moving charged particle

The Liénard-Wiechert potentials for the field produced by a point charge q that is moving along a path $\mathbf{r}(t)$ are given by

$$\phi = \frac{1}{4\pi\epsilon_0} \frac{q}{R(1 - \mathbf{v} \cdot \mathbf{n}/c)} \quad (3.1)$$

$$\mathbf{A} = \frac{\mu_0}{4\pi} \frac{q\mathbf{v}}{R(1 - \mathbf{v} \cdot \mathbf{n}/c)} \quad (3.2)$$

where $\mathbf{R} = R\mathbf{n} = \mathbf{R}_{\text{obs}} - \mathbf{r}$ is the distance taken from the point charge to the point of observation at \mathbf{R}_{obs} , ϵ_0 the vacuum permittivity, μ_0 the vacuum permeability and the quantities on the right-hand sides of the equations must be evaluated at the time $t' = t - R(t')/c$. Using the formulas $\mathbf{E} = -(\partial\mathbf{A}/\partial t) - \nabla\phi$ and $\mathbf{B} = \nabla \times \mathbf{A}$, it is found

$$\mathbf{E} = \frac{q}{4\pi\epsilon_0} \frac{(1 - v^2/c^2)(\mathbf{n} - \mathbf{v}/c)}{R^2(1 - \mathbf{n} \cdot \mathbf{v}/c)^3} + \frac{\mu_0 q}{4\pi} \frac{\mathbf{n} \times ((\mathbf{n} - \mathbf{v}/c) \times \dot{\mathbf{v}})}{R(1 - \mathbf{n} \cdot \mathbf{v}/c)^3} \quad (3.3)$$

$$\mathbf{B} = \sqrt{\mu_0 \epsilon_0} \mathbf{n} \times \mathbf{E} \quad (3.4)$$

where again the quantities on the right-hand sides refer to the time t' . At large distances, only the terms of lowest order in $1/R$ remain, i.e. only the second term in (3.3). The electromagnetic field takes at large distance the form of a plane wave which propagates in direction of \mathbf{n} . The energy flux carried off by the waves is given by the Poynting vector which, for a plane wave, has the form

$$\mathbf{S} = c \epsilon_0 E^2 \mathbf{n} = \frac{c}{\mu_0} B^2 \mathbf{n} \quad (3.5)$$

where $c = 1/\sqrt{\mu_0 \epsilon_0}$ is the speed of light. The power dP radiated into the element of solid angle $d\Omega$ is defined as the amount of energy passing in unit time through the element $R_{\text{obs}}^2 d\Omega$ (where $R_{\text{obs}} \approx R + \mathbf{r} \cdot \mathbf{n}$, $R_{\text{ob}} \gg r$) of the spherical surface with radius R_{obs}

$$dP = c \epsilon_0 E^2 R_{\text{obs}}^2 d\Omega \quad (3.6)$$

The energy during the time dt that is radiated into the element of solid angle $d\Omega$ is then $dP dt$. Here, dt is the time interval at the field point of observation at \mathbf{R}_{obs} . Because of the retardation during the propagation of the wave from the particle to the field point, the interval dt is not the same as the time interval dt' during which the energy $dP dt$ was radiated by the particle. Because $dt = (\partial t / \partial t') dt' = (1 - \mathbf{n} \cdot \mathbf{v}/c) dt'$, the power defined as the energy radiated by the particle per unit time is

$$\begin{aligned} \frac{dP}{d\Omega} &= c \epsilon_0 E^2 (1 - \mathbf{n} \cdot \mathbf{v}/c) R_{\text{obs}}^2 \\ &= \frac{c \epsilon_0 \mu_0^2 q^2 (\mathbf{n} \times ((\mathbf{n} - \mathbf{v}/c) \times \dot{\mathbf{v}}))^2}{(4\pi)^2 (1 - \mathbf{n} \cdot \mathbf{v}/c)^5} \end{aligned} \quad (3.7)$$

Circular motion

A particle that executes a circular motion at radius R_c , has a velocity perpendicular to its acceleration. When ϑ denotes the angle between \mathbf{n} and \mathbf{v} , and φ denotes the azimuthal angle of \mathbf{n} with respect to the plane through \mathbf{v} and $\dot{\mathbf{v}}$, then the power per unit solid angle is

$$\frac{dP}{d\Omega} = \frac{c q^2}{(4\pi \epsilon_0) 4\pi R_c^2} \frac{\beta^4}{(1 - \beta \cos \vartheta)^3} \left(1 - \frac{\sin^2 \vartheta \cos^2 \varphi}{\gamma^2 (1 - \beta \cos \vartheta)^2} \right) \quad (3.8)$$

where $\beta \equiv v/c$ and $\gamma = (1 - \beta^2)^{-1/2}$ is the relativistic factor. In the relativistic limit, $\beta \approx 1$. The radiated power is largest at those angles for which $1 - \beta \cos \vartheta$

is small, i.e. when $\vartheta = 1/\gamma$. A relativistic particle radiates mainly along the direction of its own motion. The total power radiated at time t' by an electron moving on a circular path is given by

$$P = 2r_e m_0 c^3 \beta^4 \gamma^4 / (3R_c^2) \quad (3.9)$$

where $r_e = e^2/4\pi\epsilon_0 m_0 c^2$ is the classical electron radius.

Spectrum

The radiated energy is spread over a wide range of frequencies. Using Fourier analysis, the spectrum can be estimated. In [1, 3], the energy radiated per unit solid angle per frequency interval, by a relativistic particle moving on a circular orbit is derived

$$\frac{d^2 I}{d\omega d\Omega} = \frac{q^2}{4\pi\epsilon_0} \frac{1}{3\pi^2 c} \left(\frac{\omega R_c}{c}\right)^2 \left(\frac{1}{\gamma^2} + \vartheta\right)^2 \left(K_{2/3}^2(\xi) + \frac{\vartheta^2}{(1/\gamma^2) + \vartheta^2} K_{1/3}^2(\xi)\right) \quad (3.10)$$

where $\xi = (\omega R_c/3c)(1/\gamma^2 + \vartheta^2)^{3/2}$, and $K_{1/3}$ and $K_{2/3}$ are modified Bessel functions. Integration over the solid angle yields the spectrum. Using relations of modified Bessel functions, it is found

$$\frac{dI}{d\omega} = \frac{q^2}{4\pi\epsilon_0} \frac{2R_c\omega}{\sqrt{3}\gamma^2 c^2} \int_C^\infty K_{5/3}^2(\xi) d\xi \quad (3.11)$$

with $C = 2\omega R_c/3\gamma^3 c$. To obtain the power detected at observation point at R_{obs} per frequency interval, the above result should be multiplied by the repetition frequency of the particle circular motion, $c/2\pi R_c$

$$\frac{dP}{d\omega} = \frac{q^2}{4\pi\epsilon_0} \frac{\omega}{\pi\sqrt{3}\gamma^2 c} \int_C^\infty K_{5/3}^2(\xi) d\xi \quad (3.12)$$

The spectrum as function of wavelength λ is obtained by substituting $\omega = 2\pi c/\lambda$. The result still contains the modified Bessel function $K_{5/3}(x)$. When $x \gg 1$, this function can be approximated by

$$K_{5/3}(x) \rightarrow \sqrt{\frac{\pi}{2x}} e^{-x} \quad (3.13)$$

The power radiated by an electron with charge $-e$ moving in a circular orbit with radius R_c per wavelength interval is therefore

$$\frac{dP}{d\lambda} \approx \pi m_0 c^3 r_e \sqrt{\frac{2}{R_c \lambda^5 \gamma}} \exp\left(-\frac{4\pi R_c}{3\lambda \gamma^3}\right) \quad (3.14)$$

This approximation is valid as long as $C = 4\pi R_c/3\gamma^3 \lambda \gg 1$, i.e. $\lambda \ll 4\pi R_c/3\gamma^3$.

Radius of curvature in a tokamak

The electrons in a tokamak do not execute a pure circular orbit with R_c . First, the guiding center of the electrons follows the helical topology of the magnetic field lines and, secondly, the electrons gyrate around the field lines. Furthermore, runaway electron experience a considerable drift motion due to the gradient and curvature of the magnetic field.

The vector equation for the radius of curvature of a bent helix is given by

$$\frac{1}{R^2} = \frac{(\mathbf{v} \times \dot{\mathbf{v}})^2}{v^6} \quad (3.15)$$

This expression is approximated by an average radius of curvature $R_{c,av}$ [5]

$$\frac{1}{R_{c,av}} \approx \frac{(1 - \theta^2)}{R_0} + \frac{eB\theta}{m_0c\gamma} \quad (3.16)$$

where $\theta = v_\perp/v_\parallel$ is the runaway pitch angle and R_0 is the major radius of the tokamak. In this approximation, a purely toroidal motion in combination with the gyration is taken into account.

In section 2.3, an expression was given for the velocity of electron velocity in a tokamak according to [6]. In tokamaks, terms of the order of $r/R_0 \ll 1$ can be neglected (r is the minor radius of the magnetic surface). Furthermore, we consider the case $v_\parallel \gg v_\perp$. Including the helical motion of the guiding center, the gyration and the drift, equation (3.15) can be written as

$$\frac{1}{R^2} = \frac{1}{R_0^2}(1 + \eta^2 + 2\eta\sin(\vartheta + \alpha)) \quad (3.17)$$

where $\eta \equiv v_\perp/v_d$ with drift velocity (from (2.21)) $v_d = \gamma v_\parallel^2 m_0/eBR_0$ and ϑ is here the poloidal angle of the particle guiding center averaged over the period of cyclotron gyration, and α is the phase angle of the gyration, $\dot{\alpha} = -\omega_{ce}$. Note that (3.16) can be rewritten, with $v_\parallel \approx c$, as

$$\frac{1}{R_{c,av}^2} = \frac{1}{R_0^2}(1 + \eta^2 + 2\eta(1 - \theta^2) + \theta^4 - 2\theta^2) \quad (3.18)$$

which gives for small θ the (maximum) value of (3.17).

The above approximations of the radius of curvature can be applied to the power per wavelength interval (3.14) to obtain the spectrum of synchrotron radiation in a tokamak. This equation (3.14) is, however, still based on the assumption of a pure circular motion of the particle. The above approximations of radius of curvature should actually be used in the general

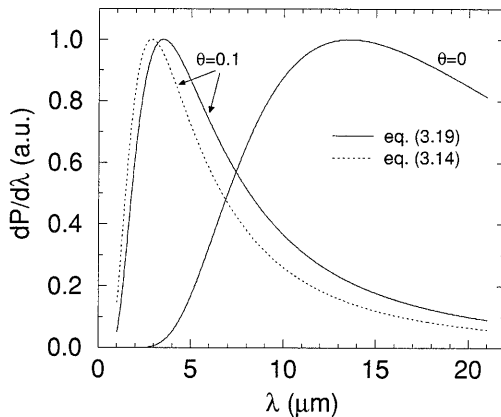


Figure 3.1: *Spectrum of a runaway electron with energy $W_r = 30$ MeV ($\gamma = 60$) for pitch angle $\theta = 0$ and $\theta = 0.1$ (recall that $\eta = eB\theta R_0/m_0c\gamma$).*

formula (3.7). In [7], the spectrum of synchrotron radiation for runaways in TEXTOR-94 is calculated, using radius (3.17) and starting from the power distribution of an arbitrarily moving charged particle. The result is

$$\frac{dP}{d\lambda} \approx \pi m_0 c^3 r_e \sqrt{\frac{2\sqrt{1+\eta^2}}{R_0 \lambda^5 \gamma}} \times \left(I_0(\zeta) + \frac{4\eta}{1+\eta^2} I_1(\zeta) \right) \exp\left(-\frac{4\pi R_0}{3\lambda\gamma^3 \sqrt{1+\eta^2}}\right) \quad (3.19)$$

where $\zeta = 4\pi R_0 \eta / 3\lambda\gamma^3 (1+\eta^2)^{3/2}$, I_0 and I_1 are modified Bessel functions and r_e the classical electron radius. The spectrum is shifted to smaller wavelengths compared with the case $\eta = 0$ as is shown in figure 3.1 for a runaway electron with energy $W_r = 30$ MeV. Note that η can be written as $eB\theta R_0/m_0c\gamma$ with θ the runaway pitch angle, so that the case $\theta = 0$ corresponds to $\eta = 0$.

3.2 Infrared measurements

Experimental set-up

The synchrotron radiation from the runaway electrons in TEXTOR-94 is emitted in the infrared (IR) spectral range [8]. A thermographic camera (Inframetrics 600) is used for the detection of the radiation. The camera

consists of a liquid nitrogen cooled HgCdTe detector, a focusing lens and two scanning mirrors. One mirror scans horizontally, one vertically. In this way, a two dimensional TV picture is generated according to NTSC standard. One horizontal line is scanned in about $65 \mu\text{s}$, a complete picture consists of 256 lines and is scanned in 16.7 ms. Each point of the observed area is probed once in the 16.7 ms. One complete frame contains, therefore, information on space and time simultaneously.

The synchrotron radiation of the runaways falls onto a concave mirror mounted in the vacuum vessel in the equatorial plane. The radiation is guided through an optical system, consisting of the concave mirror, a lens at the vessel window, a plane mirror, and is finally projected on a field lens. The IR camera focuses on this field lens. A sketch of the experimental set-up is drawn in figure 3.2.

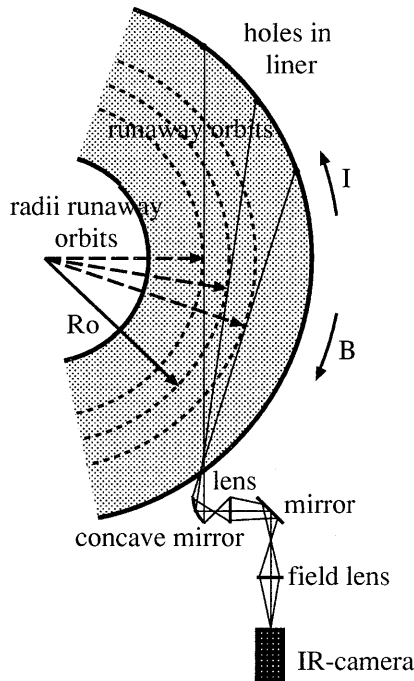


Figure 3.2: Schematic top view of TEXTOR-94 with experimental set-up for infrared measurements.

The detector in the IR camera is sensitive in the wavelength range of $3 - 14 \mu\text{m}$. The use of CaF_2 for the lenses and window limits this range to about $3 - 8 \mu\text{m}$. Thermal radiation from the limiter, liner or RF antennas in TEXTOR-94 has its maximum emission in the wavelength range where the camera is sensitive. Because this radiation is not absorbed by the plasma, it is present in the camera picture. On the one hand this limits the sensitivity of synchrotron radiation measurements when at low runaway intensity the radiation is lost in the thermal background. On the other hand, the thermal background provides a tool for aligning the camera and it is used for position calibration in the two-dimensional synchrotron projections. In figure 3.3, first a picture made with a visible light camera is shown. Here, the liner and limiter can be observed clearly. The same picture, now made with the IR camera is also shown. Because the temperature differences in the background are not large, it is difficult to distinguish the different objects (holes in the liner, the limiter) in the IR picture. In figure 3.4, an IR picture of synchrotron radiation is shown (including thermal background). The IR pictures are recorded on video tape during the experiments and analyzed afterwards.

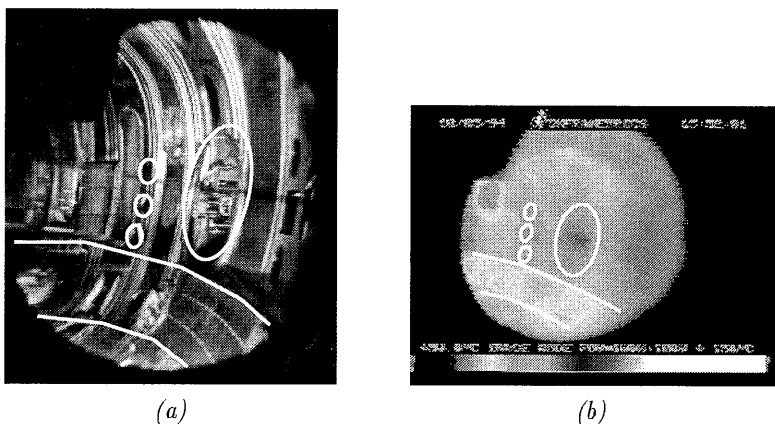


Figure 3.3: (a) View into TEXTOR-94 with normal camera. High field side (HFS) is on the left hand side. Indicated are a few holes in the liner (circles) and the limiter (below). (b) View into TEXTOR-94, now with an infrared camera, taken from same point as picture in (a). Also, same holes and limiter as in (a) are indicated in the thermal background.

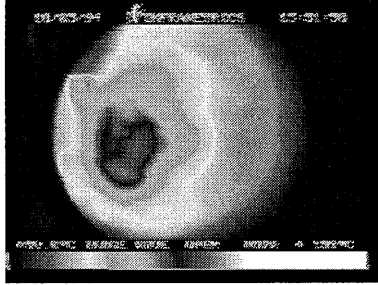


Figure 3.4: *Typical infrared picture during a runaway discharge (at $t = 4$ s). The darker spot is synchrotron radiation.*

Analysis

Position of holes in the liner and the limiter are used to calibrate the IR pictures of the synchrotron radiation projections. The toroidal position in the equatorial plane is estimated by drawing the tangents from recognizable objects in the thermal background to the concave mirror along toroidal 'orbits'. In this way, objects in the thermal background, i.e. pixel numbers in the IR picture, correspond to toroidal positions R . Interpolation between these points using a continuous function gives the position R of every pixel in the equatorial plane. This calibration construction is shown in figure 3.2. In vertical direction of the IR pictures, an analogous method is used that gives the correspondence between pixel numbers and positions in toroidal geometry in that direction.

The time evolution of the synchrotron radiation is deduced by integration of the synchrotron intensity within a software defined box in the IR pictures. This box can contain the complete synchrotron spot or only a small part of it. When a narrow slit-shaped box is taken, at the equatorial plane, it is possible to measure synchrotron radiation profiles. An example of a defined box in an IR picture and the resulting radiation evolution is shown in figure 3.5.

Interpretation

The detected power from a beam of runaway electrons is dependent on the energy spectrum of the runaway electrons and the number of runaways. Apart from previous rough measurements and from Monte Carlo simulations of the energy distribution [9], the exact distribution is not measured. The measurements and simulations in [9] and the calculated energy distribution in section 4.1 indicate that the assumption of a mono-energetic distribution is justified

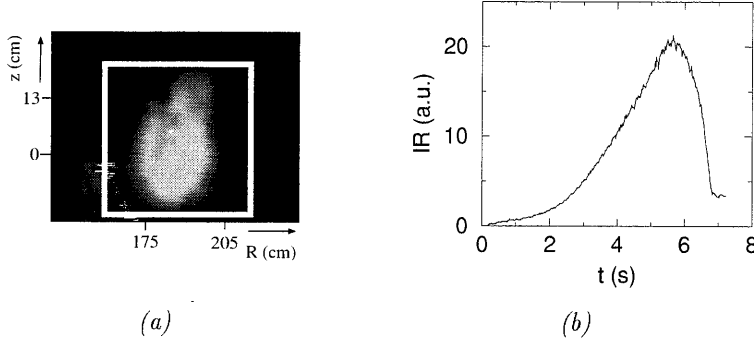


Figure 3.5: (a) IR picture of synchrotron radiation with software defined box. Thermal background is subtracted. (b) Typical radiation evolution. At $t \approx 5.5$ s, the current decay phase starts.

within an error of 15%.

Under the assumption of mono-energetic energy distribution, the measured intensity evolution can be interpreted as the evolution of total number of runaways. When the volume of the toroidal runaway beam does not change significantly, the measured intensity is proportional to the total runaway density n_r .

In [8–10], the absolute number of runaway electrons N_r is calculated from

$$N_r \int \frac{dP}{d\lambda} T(\lambda) d\lambda = A\Omega \int L_\lambda^s T(\lambda) d\lambda \quad (3.20)$$

where $T(\lambda)$ is the transmission function of the optical system, A the cross-sectional area of the ring filled with runaways, $\Omega = 2\pi \times 2\theta$ the solid angle into which the synchrotron radiation is emitted and L_λ^s the measured spectral radiance of synchrotron radiation. $dP/d\lambda$ is the average of equation (3.14) over the energy distribution function. $\int L_\lambda^s T(\lambda) d\lambda$ is obtained by comparing the synchrotron radiation with the thermal radiation of the limiters of which the temperature is independently measured (about 450 K in normal discharges) and the emissivity is known (graphite limiter surface, emission coefficient ≈ 0.8). Although the absolute intensity can be determined rather accurately, N_r can only be estimated within an order of magnitude due to the uncertainty in the exact energy distribution function. Nevertheless, in [10], it was estimated $N_r \approx 2 \times 10^{14}$, in an Ohmic runaway discharge¹. The runaway

¹In [10], it was noted that this estimate is a factor 50 less than the value derived in [8]

current, $I_r = N_r e c / 2\pi R_0$, is, therefore, about 1 kA in an Ohmic runaway discharge, which is less than 1% of the total plasma current. Furthermore, the above estimate implies that the runaway density n_r is approximately $N_r / ((\pi r_b^2)(2\pi R_0)) \approx 1 \times 10^{14}$ with $r_b \approx 0.20$ m the radius of the runaway beam. In normal runaway discharges $n_r/n_e \sim 10^{-5}$. The runaway electrons can be regarded as test particles, not bound to the ion cloud by ambipolar effects. However, in case of a rapid loss of runaway electrons, ambipolar effects can become more significant.

3.3 Other runaway diagnostics

When runaway electrons are lost from the plasma, they hit the limiter and generate hard x-ray radiation. These hard x-rays can produce neutrons by photo-nuclear reactions. The threshold energy for carbon, the limiter material, is about 10 MeV. The loss of runaways with an energy of at least 10 MeV is clearly visible on the neutron signal. Note that under the plasma conditions of runaway generation (low density) the amount of fusion neutrons is negligible.

In TEXTOR-94, the presence of large numbers of low energetic runaway electrons that are not observed by detection of synchrotron radiation with the IR camera, can be recognized from the electron cyclotron emission (ECE) measurements. Under plasma conditions of large production of lower energetic runaways, the so-called slide-away regime (e.g. [11]), the ECE signals show a strong rapid rise and get into saturation. This regime occurs in plasmas with low density and low loop voltage. The formation of the regime is explained by Parail and Pogutse [12]. Their model involves an instability which causes pitch angle scattering of runaway electrons. This instability limits the runaway energy. Therefore, no synchrotron radiation is measured in a plasma in the slide-away regime.

There is always the possibility that during low density runaway experiments, the density is chosen too low and that the plasma goes into the slide away regime. Hence, to protect the ECE detection system from too extensive exposure of radiation, only a few ECE channels are available during most of the runaway experiments. In discharges with sufficient generation of high energetic runaways, where synchrotron radiation is observed, the ECE signals normally do not show a saturation.

The interpretation of the ECE signals in a plasma with high energetic runaways is not so straightforward as in a normal plasma. The signals consist of a thermal and non-thermal contribution. Normally, the absorption

because of an incorrect normalization of the synchrotron power in [8].

and emission of ECE in a plasma is in equilibrium. Therefore, ECE is a measure of temperature. In the presence of runaway electrons, down-shifted (due to the relativistic motion) higher harmonics are measured too. An exact temperature measurement is, therefore, difficult during the runaway experiments.

References

- [1] Jackson J D 1975 *Classical Electrodynamics* John Wiley & Sons, New York
- [2] Landau L D, Lifshitz E M 1972 *A shorter course of theoretical physics, Volume I: Mechanics and Electrodynamics* Pergamon Press, Oxford
- [3] Schwinger J 1949 *Phys. Rev.* **75** 1912
- [4] Sokolov A A, Ternov I M 1968 *Synchrotron Radiation* Akademie Verlag, Berlin
- [5] Russo A J 1991 *Nucl. Fusion* **31** 117
- [6] Pankratov I M 1996 *Plasma Phys. Rep.* **22** 535
- [7] Pankratov I M 1999 *Plasma Phys. Rep.* **25** 145
- [8] Finken K H, Watkins J G, Rusbüldt D, Corbett W J, Dippel K H, Goebel D M, Moyer R A 1990 *Nucl. Fusion* **30** 859
- [9] Jaspers R J E, 1995 *Relativistic runaway electrons in tokamak plasmas* PhD Thesis, Eindhoven University of Technology, The Netherlands
- [10] Jaspers R, Finken K H, Mank G, Hoenen F, Boedo J, Lopes Cardozo N J, Schüller F C 1993 *Nucl. Fus.* **33** 1775
- [11] Oomens A A M, Ornstein L T H, Parker R R, Schüller F C, Taylor R J 1976 *Phys. Rev. Letters* **36** 255
- [12] Parail V V, Pogutse O P 1978 *Nucl. Fusion* **18** 303

Chapter 4

Simulations

In this chapter, a closer look is taken at what can be expected from the synchrotron measurements in TEXTOR-94. The formulas presented in chapter 3 are implemented into a computer code to simulate the time evolution of the synchrotron radiation. Also, it is investigated how the emitted synchrotron cone is projected on the poloidal cross section in the TEXTOR-94 geometry.

4.1 Radiation evolution

In this section, a code is presented that simulates the synchrotron radiation evolution. The calculated evolutions that are expected to be measured in TEXTOR-94 are discussed.

Code

The energy evolution of one electron in a tokamak, $\gamma(t)$, is determined from the difference in power gained from the electric field and the power lost by radiation, $dW_r/dt = m_0c^2(d\gamma/dt) = P_E - P$. The power gain from the electric field is $P_E = eEc$. For the power lost by radiation, equation (3.9) is used with the approximated radius of curvature (3.16), which means that only the toroidal motion and the cyclotron gyration of the electron are taken into account. In this way, a γ_j for every j th time step is calculated for one runaway electron. The maximum energy that is reached by a runaway electron, follows from the equilibrium $P_E - P = 0$. Because the energy loss due to collisions is small compared to the radiation loss, it is not taken into account.

The total amount of power radiated by one electron P_j is given by (3.9) for every γ_j . It is assumed that all the emitted radiation falls into the detector, but only a fraction of the total emitted wavelength spectrum is detected with

the infrared camera used at TEXTOR-94 ($\lambda \in [3, 8] \mu\text{m}$). With the spectral power density (3.14), the power per electron per wavelength interval is calculated for every γ_j . Integration over the detected wavelength range gives the amount of power that is actually detected. For every electron energy γ_j , the integrated power $P_{\text{det},j} = \int_3^8 (dP/d\lambda) R_{\text{cam}}(\lambda) d\lambda$ is determined, where $R_{\text{cam}}(\lambda)$ denotes the response function of the camera. In the model, $R_{\text{cam}}(\lambda) = 1$ is taken for the whole detectable wavelength range. In the simulation, the integral of detected power is approximated by $P_{\text{det},j} = \sum_k (dP/d\lambda) R_{\text{cam}}(\lambda) \Delta\lambda_k$ where the detectable wavelength range is divided in $k = 50$ intervals.

At every time step, dn_{rij} runaways are born, by both primary (2.8) and secondary generation (2.14). After this runaway birth, every i th fraction of density is followed in time. Because the runaways in TEXTOR-94 carry a negligibly small current, no decrease in electric field is considered in the model during the acceleration of the density fractions. At later time steps, a finite confinement time τ_r results in a continuous loss of runaways. In this way, a matrix of density fractions is generated. At every $i = j$ th row a new fraction of density is added, which is followed in time (matrix elements dn_{rij} with $j > i$). The matrix elements dn_{rij} with $j < i$ are all equal to zero.

Every j th time step now corresponds with $i = j$ fractions of density dn_{rij} and an electron energy γ_j , and, therefore, with an amount of power per electron P_j and detected power per electron $P_{\text{det},j}$. The total density at time $t_j \equiv j dt$ follows from the summation over all i fractions of density at that particular time j , $\sum_i dn_{rij}$. The total power radiated by one density fraction (that has energy γ_j) is equal to the product $dn_{rij} P_j$. Here, it is assumed that the distance between relativistic runaways within one density fraction is sufficiently large to neglect the mutual interaction between the electric and magnetic fields of the electromagnetic waves emitted by the runaway electrons. The total amount of power radiated at a time t_j is the summation of these products over all density fractions i , $\sum_i dn_{rij} P_j$. For the total detected power, it is found $\sum_i dn_{rij} P_{\text{det},j}$. The simulated evolution of the synchrotron radiation, detected in TEXTOR-94, is given by this sum calculated for every time j .

After a certain time span, an energy distribution can be calculated. For each energy interval $d\gamma$, the density fractions of runaways with an energy within the energy interval are summed. Also, a distribution of radiated power and of detected power can be estimated by adding the corresponding power per energy interval.

Results

The maximum γ that is reached in TEXTOR-94 according to the above described model is about 60 (see figure 4.1), which corresponds with an energy of 30 MeV. This energy limit is a consequence of the radiation equilibrium.

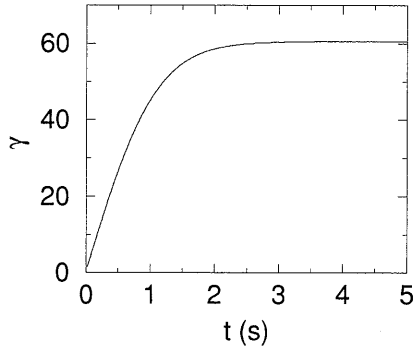


Figure 4.1: *Energy development of one runaway electron in TEXTOR-94.*

In the calculation, $\beta \equiv v/c \approx 1$. Furthermore, no evolution of the runaway pitch angle distribution is taken into account, but $\theta = 0.1$ for all energies. At the time of runaway birth, however, $\theta \approx v_{th}/v_{crit}$. During the acceleration, the pitch angle decreases, so that at the moment when the electrons are radiating significantly, the distribution peaks at $\theta \approx 0.1$. An increase in θ due to the ripple resonance (see section 2.4) is not taken into account. Finally, no possible density dependence of θ is taken into account. Other parameters are chosen to be $E \approx 0.1$ V/m, $Z_{eff} = 2$, $\ln\Lambda = 16$. These values are typical in TEXTOR-94.

In figure 4.2, the radiated power of one electron and the detected power (wavelength range $3 - 8 \mu\text{m}$) of one electron, both as function of time, are shown. These evolutions are based on radiation calculations of an electron in circular motion with an averaged radius of curvature due to toroidal motion and cyclotron gyration (3.16).

The evolution of total runaway density is shown in figure 4.3. When the runaway confinement time τ_r is shorter than the avalanche time t_0 , needed for existing runaway electrons to kick out thermal electrons into the runaway region (see figure 2.1), then the runaway density n_r saturates. At the level of saturation, the runaway generation equals the runaway loss. In the simulation, $\tau_r = 0.1$ s and $t_0 = 0.5$ s were taken. When, on the other hand, the avalanche time t_0 is much smaller than the typical runaway confinement

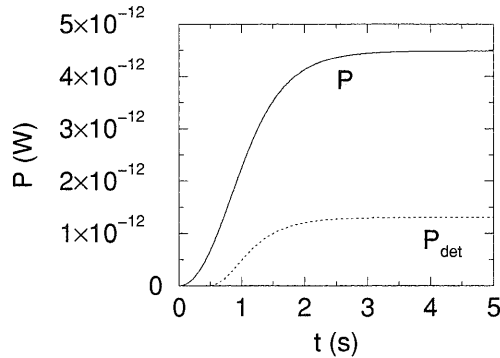


Figure 4.2: Total power radiated by one electron (P_j) and power emitted by one electron as detected by the IR camera ($P_{\text{det},j}$).

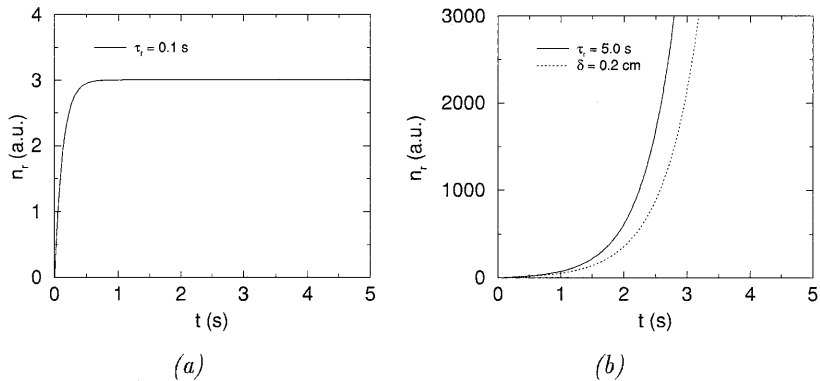


Figure 4.3: Evolution of runaway density for $t_0 = 0.5$ s and (a) constant runaway time $\tau_r = 0.1$ s, (b) constant runaway time $\tau_r = 5$ s and energy dependent confinement time according to [1] with $\delta = 0.2$ cm. (Curves are all normalized at same value of n_r .)

time, the secondary generation process is dominant. This is clear from the exponential rise in density n_r in figure 4.3. In this particular case, $\tau_r = 5$ s and $t_0 = 0.5$ s were taken.

In section 2.5, a description of an energy dependent runaway confinement time by Mynick and Strachan [1] was discussed. A density evolution according to that model is also shown in figure 4.3. The confinement reduction curve is calibrated to thermal confinement of 20 ms, scaled with a velocity factor v_{th}/v_r with v_r the runaway velocity. A mode width $\delta = 0.2$ cm is taken.

The simulated evolutions of the synchrotron radiation for an Ohmic runaway discharge are shown in figure 4.4. In figure 4.4(b), a dominant secondary

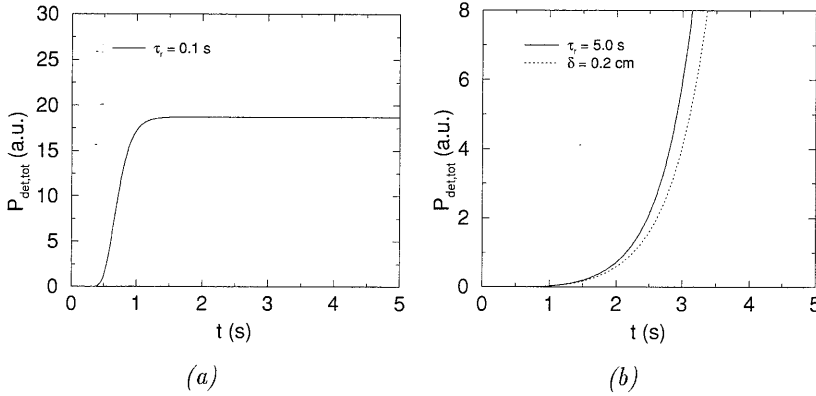


Figure 4.4: *Simulation of the total power emitted by all runaways as detected by the IR detector for a typical Ohmic runaway discharge (a) with constant $\tau_r = 0.1$ s, (b) with constant $\tau_r = 5.0$ s and with an energy dependent confinement time according to [1] with $\delta = 0.2$ cm.*

generation mechanism was assumed which is usually the case in TEXTOR-94. Observations of a steady state radiation signal are scarce. An example is found in [2]. The radiation evolutions in figure 4.4 are calculated for a density development where $t_0 = 0.5$ s and $\tau_r = 0.1$ s, $\tau_r = 5$ s and $\delta = 0.2$ cm as shown in figure 4.3.

Finally in figure 4.5, the energy distribution and radiated and detected power distributions at $t = 5$ s are shown. When secondary generation is the dominant generation process, the energy distribution is much broader than is the case when primary generation is the dominant production mechanism. At $\gamma \approx 60$ the radiation limit is reached. When the runaway confinement time τ_r is small, the energy spectrum remains narrow because of the small available

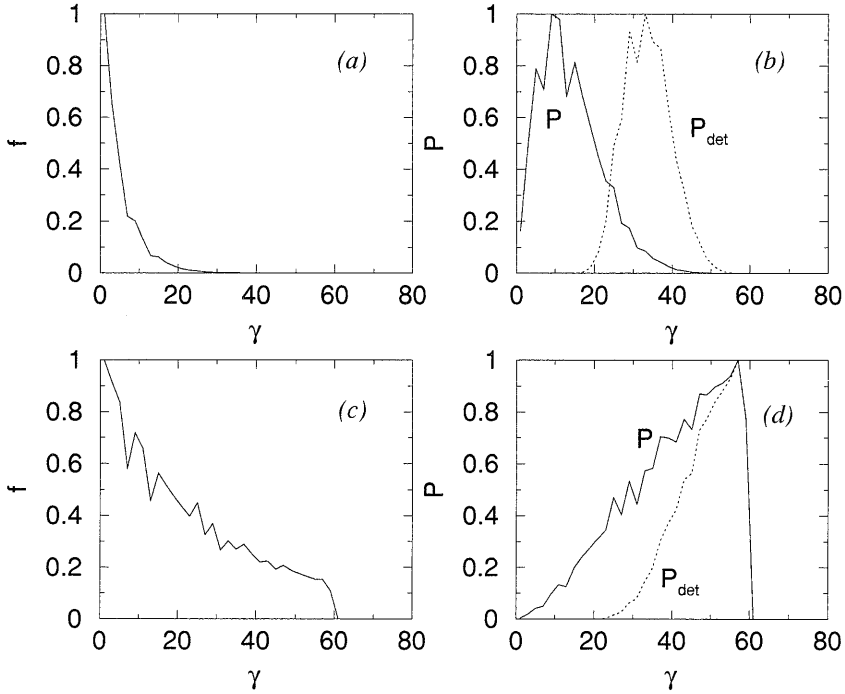


Figure 4.5: (a) Distribution function and (b) power distribution (emitted and detected) for $\tau_r = 0.1$ s (c) Distribution function and (d) power distribution (emitted and detected) for $\tau_r = 5$ s

time for acceleration. The distribution of emitted synchrotron power differs from the distribution of detected power, because in the latter case only a small fraction of the total wavelength spectrum is observed. The spectra show that runaways are significantly radiating when they have at least an energy of 10 MeV. The distribution of detected power P_{det} (wavelength range $\lambda \in [3, 8] \mu\text{m}$) show that most of the detected radiation is, however, emitted by the highest energetic runaways. This justifies the assumption of a 'mono-energetic distribution' in the interpretation of the radiation measurements.

4.2 Poloidal projection of radiation cone

The synchrotron radiation is measured with a camera that views tangentially into TEXTOR-94 in direction of electron approach. In this section, it is investigated what is observed from the radiation cone emitted by the runaway beam.

Code

The guiding center of runaway electrons follow the magnetic field lines. Locally, these field lines make a smaller angle with the equatorial plane at the high field side (HFS) than at the low field side (LFS). At normal TEXTOR-94 operation (plasma current I_p in counter clockwise direction, toroidal magnetic field in clockwise direction), the field lines at the HFS point upwards. The guiding center of a runaway electron has a similar topology.

From [3], we know that in case of relativistic particle energy, the topology of the particle drift orbits differs from the topology of magnetic field lines. The particle topology is characterized by a drift orbit safety factor q_D which is, however, still a function of r and ϑ . So, also in higher order approximation, the drift orbits have a smaller inclination at the HFS with respect to the equatorial plane than at the LFS.

A runaway electron gyrates around its guiding center. The gyrating velocity vector forms a cone with vertex angle 2θ , i.e. twice the runaway pitch angle. In [4], the effect of the pitch angle on the synchrotron spot was already studied. The horizontal extent of the synchrotron pattern was found to be broader at the HFS than the diameter of the original runaway beam by $R(1 - \cos \theta)$ where R is the major radius of the runaway orbits forming the beam.

In the first section of this chapter, it was derived that for relativistic electrons, the radiation is emitted in a small cone with half vertex angle of $1/\gamma$. The runaway electrons that contribute significantly to the detected synchrotron radiation have energies of more than 20 MeV. These electrons have a total vertex angle of about 2° or even less. Hence, runaways that are detected by the IR camera emit their radiation practically along their velocity vector.

In conclusion, the synchrotron radiation of one electron is in good approximation emitted along its velocity vector. Due to the gyration of the electron, the velocity vector runs along the surface of a cone with vertex angle 2θ . The top of the cone follows the guiding center motion, which is similar to the helical topology of the magnetic field lines. The synchrotron radiation is observed by looking tangentially into the tokamak in direction of electron ap-

proach. The infrared camera records a poloidal projection of the synchrotron radiation coming from the toroidal runaway beam. The synchrotron radiation emitted along the electron velocity vector \mathbf{v} (see equation (2.22)) falls into the detector when $\mathbf{v} \times (\mathbf{D} - \mathbf{R}) = 0$, where \mathbf{D} denotes the position of the detector and \mathbf{R} is the runaway position (see equation (2.23)), both with respect to the axis of symmetry of the tokamak. This condition is treated analytically in [5] where use is made of certain assumptions on position of detector and runaway beam size compared to toroidal geometry. Results of a numerical calculation are presented below.

Results

Figure 4.6 shows a few examples of calculated synchrotron patterns coming from a set of nested runaway drift surfaces ($\gamma = 60$) with radius $r_{\max} = 15$ cm and pitch angle $\theta = 0$, $\theta = 0.05$ and $\theta = 0.1$. \mathbf{D} is taken in the equatorial plane. In figure 4.7, the positions of the runaways from which these patterns originate are shown in a schematic top view of TEXTOR-94. In the calculation, a parabolic $q(r) = q_D(r)$ profile was assumed with edge safety factor $q_a = 3.8$. No drift orbit shift was taken into account.

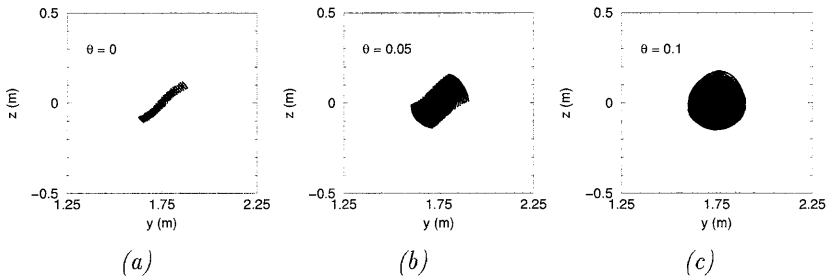


Figure 4.6: *Poloidal projections of emitted synchrotron radiation for pitch angle $\theta = 0$, $\theta = 0.05$ and $\theta = 0.1$ ($r_{\max} = 15$ cm). The axes correspond to the Cartesian coordinate system as given in figure 2.3.*

The effect of the helical topology of the drift orbits on the synchrotron pattern becomes clear from the runaway beam with pitch angle $\theta = 0$. Only the velocity vectors of the lower left and the upper right part of the circular runaway beam point into direction of the detector. The angle that the velocity vector, which is tangential to the helical drift orbit in case of $\theta = 0$, makes with respect to the equatorial plane varies for different minor radius with approximately $r/R_0 q_D(r)$. Hence, the part of the circular runaway beam of which the velocity vector hits the detector changes with minor radius. This

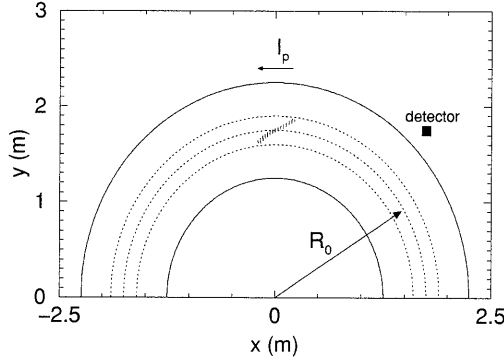


Figure 4.7: *Position in toroidal geometry (top view) of the runaway electrons (dotted region) from which the synchrotron radiation falls into the detector when $\theta = 0$. When $\theta > 0$, the region of runaway electron positions becomes broader.*

is clearly seen when a strongly varying q_D profile is considered in the pattern simulation. The synchrotron pattern from the circular runaway beam has in that case a wave shape. In [5], the angle of the observed inclination with respect to the equatorial plane is derived analytically, $\tan\beta \approx (D - R)/q_D$.

The angle of the velocity vector with the equatorial plane, determined by the ratio between the poloidal and toroidal magnetic field strength, is at the HFS smaller than at the LFS. This causes an asymmetry in the synchrotron pattern. For TEXTOR-94 geometry, the upper half of the pattern is larger than the lower part. Because the difference between the HFS and LFS angles is small, this effect is hardly observed from the calculated patterns in figure 4.6.

The effect of a finite pitch angle θ is a broadening of the synchrotron pattern in direction perpendicular to the line that matches the inclination of the pattern. When θ is chosen large enough, the radiation from the complete runaway beam can fall onto the detector.

References

- [1] Mynick H E, Strachan J D 1981 *Phys. Fluids* **24** 695
- [2] Entrop I, Lopes Cardozo N J, Jaspers R, Finken K H 1998 *Plasma Phys. and Contr. Fusion* **40** 1513
- [3] de Rover M, Lopes Cardozo N J, Montvai A 1996 *Phys. Plasmas* **3** 4468;
de Rover M, Lopes Cardozo N J, Montvai A 1996 *Phys. Plasmas* **3** 4478
- [4] Jaspers R J E, 1995 *Relativistic runaway electrons in tokamak plasmas*
PhD Thesis, Eindhoven University of Technology, The Netherlands
- [5] Pankratov I M 1996 *Plasma Phys. Rep.* **22** 535

Chapter 5

Runaway transport in Ohmic plasmas

In this chapter, a method is presented how to derive the runaway diffusion coefficient from the synchrotron measurements. We first restrict ourselves to Ohmically heated plasmas. In the next chapter, the runaway transport properties during auxiliary heating are discussed. This chapter is a reproduction of the article 'Diffusion of runaway electrons in TEXTOR-94' by I.Entrop, N.J.Lopes Cardozo, R.Jaspers and K.H.Finken, published in Plasma Physics and Controlled Fusion **40** 1998, 1513, reproduced with kind permission of the journal editor.

Diffusion of Runaway Electrons in TEXTOR-94

I. Entrop^{1,2}, N.J. Lopes Cardozo¹,
R. Jaspers¹, K.H. Finken²

Partners in the Trilateral Euregio Cluster:

¹FOM Instituut voor Plasmafysica Rijnhuizen, EURATOM Association,
PO Box 1207, 3430 BE Nieuwegein, The Netherlands

²Institut für Plasmaphysik, Forschungszentrum Jülich GmbH, EURATOM
Association, D-52425 Jülich, Germany

Abstract

In the TEXTOR-94 tokamak, radial profiles of synchrotron radiation from relativistic runaway electrons have been measured. From these and measurements of the evolution of the radiation, a radial profile of the diffusion coefficient for the runaway electrons in the plasma core with $W_r \approx 25$ MeV was derived. At half radius, $D_r < 0.01 \text{ m}^2\text{s}^{-1}$ was found. This result is compared with several other measurements of runaway diffusion coefficients derived mainly from runaway losses at the plasma edge.

5.1 Introduction

It is well known that thermal electron diffusivity in a tokamak plasma is much larger than neoclassical theory predicts. A possible source for this anomalous loss are magnetic field perturbations. In the study of the magnetic perturbations runaway electrons could be helpful. Highly energetic runaways are almost collisionless. They experience a drag force [1]

$$F_{\text{drag,rel}} = -\frac{e^4 n_e \ln \Lambda}{4\pi \epsilon_0^2 m_e v^2} \left(1 + \frac{Z_{\text{eff}} + 1}{\gamma} \right) \quad (5.1)$$

where e and m_e are the electron charge and the electron rest mass, n_e is the electron density, $\ln \Lambda$ the Coulomb logarithm, v the electron velocity, Z_{eff} the effective charge and γ the relativistic factor. The first term is due to collisions with bulk electrons and will limit as $v \rightarrow c$ to a smaller value as for electrons with thermal velocity. The second term comes from collisions with ions and will be negligible small for relativistic runaways. The runaway dynamics, e.g. diffusion, is therefore mainly determined by magnetic turbulence.

In the past, many experimental and theoretical studies on runaway transport have been made, e.g. [2–10], of which several concentrated on the estimation of the magnetic turbulence level with the help of runaway measurements in tokamaks, for both the plasma edge and the plasma core. It has been pointed out that a potential difficulty with using runaways as a probe for magnetic fluctuations is the fact that the topology of runaway trajectories is not necessarily the same as the topology of the magnetic field lines [11]. Also, the large drift displacement of runaway electrons could decouple them from field lines and so make them less sensitive to magnetic turbulence [11–13].

Most experiments on edge runaway transport are based on measurements of hard x-ray bremsstrahlung. In [2], this x-ray bremsstrahlung comes from a tungsten probe. For stable discharges with runaways of energy $W_r < 300$ keV, a runaway diffusion coefficient is found $D_r = 1 - 50 \text{ m}^2\text{s}^{-1}$. Runaway flux fluctuations due to machine-driven oscillations were studied at PLT [3] to deduce $D_r = 0.05 - 0.1 \text{ m}^2\text{s}^{-1}$ for runaways with $W_r \approx 0.4 - 1$ MeV. The plasma column in ORMAK [4] was shifted inward, which decreased the major radius. The shift left the runaways a longer distance at the low field side to diffuse, and from the resulting changes in the hard x-ray bremsstrahlung, an estimate of $D_r = 10^{-2} - 1 \text{ m}^2\text{s}^{-1}$ was made. A similar experiment was done in TEXT [5, 6] with the result $D_r \approx 2 \text{ m}^2\text{s}^{-1}$. Other experiments in TEXT concerning runaway diffusion are the generation of a stochastic layer in the plasma edge by applying resonant magnetic fields. Switching on and off the coils that produce these resonant magnetic fields caused changes in the hard x-ray bremsstrahlung signal. From these changes, $D_r \approx 0.25 \text{ m}^2\text{s}^{-1}$ could be estimated, determined at $r \approx 0.9a$, i.e. a few centimeters more inward than with the shift experiment. Finally, in ASDEX [7], the hard x-ray bremsstrahlung at a radially movable target at the plasma edge was measured, produced by runaways that are generated only in the start-up phase of discharges and that reach an energy of about 1 MeV. The characteristic time for the decrease of the x-ray bremsstrahlung was interpreted as the runaway confinement time τ_r . For Ohmic discharges, a value of $\tau_r = 600$ ms was measured, about 12 times the energy confinement time. Photoactivation measurements on the PLT limiter [8] lead to estimates of $\tau_r = 50 - 90$ ms for runaways with $W_r = 8 - 23$ MeV, which is in the range of 2-10 times the thermal electron energy confinement time.

Diffusion of core runaways has been studied in JET and TEXTOR. In JET [9], the perpendicular x-ray emission of runaways with energies up to a few MeV was measured. A diffusion model simulating the evolution of the line integrated x-ray signals was used to determine $D_r \approx 0.2 \text{ m}^2\text{s}^{-1}$ for $r < 0.5a$. In the TEXTOR tokamak, runaways with energies larger than 20 MeV have been observed with an infrared (IR) camera [10, 14–16], which

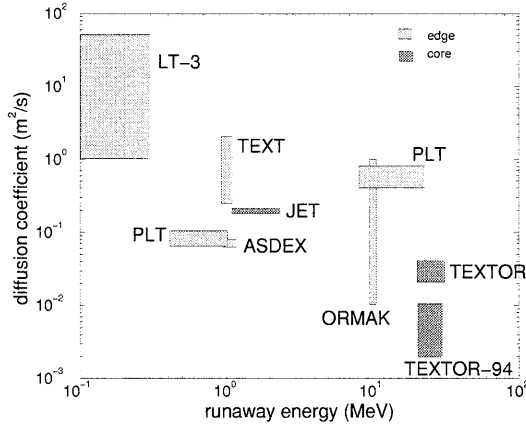


Figure 5.1: Summary of results on runaway diffusion in tokamaks, including the result in the present paper for TEXTOR-94. For calculation of a diffusion coefficient from confinement time (in case of ASDEX and PLT), the relation (5.13) is taken.

measures the synchrotron radiation these highly relativistic electrons in the plasma core emit. For Ohmic discharges, $\tau_r > 1$ s [10]. In a so-called runaway snake [16], $D_r < 0.02$ m²s⁻¹ is estimated. In figure 5.1, the above mentioned results of the different runaway experiments are summarized.

Figure 5.1 shows that in the high energy range, a lack of experimental data exists, mostly because of the differences in tokamak sizes and because of limited working ranges of diagnostics. In that energy range, runaway dynamics is the least influenced by collisions and, therefore, could be most useful for turbulence measurements. Drift effects, however, will probably play a significant role in this high energy range and could reduce the applicability of runaway measurements for turbulence estimation, depending on the kind of turbulence model that is assumed.

Runaway confinement in TEXTOR [10,16] was not studied in great detail and only roughly estimated. The previous runaway experiments in TEXTOR were, furthermore, limited by the fact that only a small part of the plasma cross section could be viewed. This inhibited the determination of radial profiles of runaway densities. The present paper reports on experiments in which the field of view was expanded to cover the full plasma. This allows the determination of the profile of the runaway diffusion coefficient.

In section 5.2 a detailed description of the experimental set-up for the observation of runaways, the image processing and a typical example of a runaway discharge are given. In section 5.3, a simple diffusion model and the assumptions needed for applying that model to the runaway case are discussed. Measurements and the corresponding estimate of the runaway diffusion coefficient are presented in section 5.4. The magnetic turbulence level at the TEXTOR-94 plasma core is estimated and discussed in the last section.

5.2 Experiment

5.2.1 Set-up

Experiments were performed in the TEXTOR-94 tokamak, which has a major radius $R_0 = 1.75$ m and minor radius $a = 0.46$ m. Typical plasma parameters used for this set of experiments are: toroidal magnetic field $B_T = 2.25$ T, plasma current $I_p = 350$ kA, flat-top time of about 5 s, flat-top loop voltage $V_{loop} \approx 1.0$ V. The line averaged electron density \bar{n}_e was kept below $1.0 \times 10^{19} \text{ m}^{-3}$ to obtain typical Ohmic runaway discharges. The synchrotron radiation, originating from the movement of the highly relativistic runaways, is measured with an Inframetrics thermographic camera. This camera uses a single HgCdTe detector and a scanning mirror (NTSC-TV standard, i.e. one two-dimensional picture in 16 ms). It is sensitive in the wavelength range of 3 – 14 μm , but as CaF_2 optics are used, the working range is 3 – 8 μm . The line of sight of the camera is tangential to the plasma in the direction of electron approach. Figure 5.2 shows a schematic set-up used for synchrotron radiation measurements.

The difference of the present set-up with earlier experiments [10, 14–16], is the use of a concave mirror (see figure 5.2). This mirror views a complete poloidal cross section instead of only a part of it. This complete overview enables us to study the radial distribution of the synchrotron radiation.

5.2.2 Image processing

In figure 5.3, a typical example of an image made with the NTSC infrared camera is shown. In this image taken at $t \approx 4$ s, the synchrotron radiation originating from the runaways is visible as a clear spot. The images are deformed due to the concave mirror. In images taken before the synchrotron radiation is observed, thermal radiation from the ALT limiter and windows in the liner is detected. Using these window and limiter positions as points of

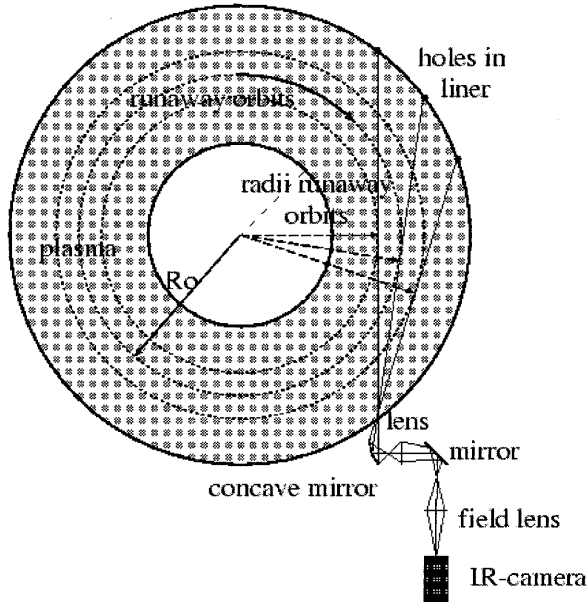


Figure 5.2: Schematic set-up for synchrotron measurements. The plasma current direction is counter-clockwise, the direction of the toroidal magnetic field is clockwise. Using reference points in the vessel wall, the runaway orbits are constructed for pitch angle $\theta = 0$.

reference, it is possible to correct for the image deformation. Figure 5.2 shows this construction of the major radii of runaway orbits. For this construction, a pitch angle of the runaways $\theta = v_{\perp}/v_{\parallel} = 0$ is assumed, which means that the synchrotron radiation would be emitted only in forward direction. In TEXTOR, typically $\theta = 0.12$ [10] which leads to an error in orbit major radius of only a few percent.

During a discharge, an image is scanned every 16 ms and recorded on video tape. The images are software processed afterwards. Integration boxes are defined, e.g. a box which contains the total synchrotron spot or a narrow slit across the image in the equatorial plane (see figure 5.3). The integrated signal within the boxes can be used as a time trace of the synchrotron radiation intensity, after background correction.

In case a narrow slit in the equatorial plane is considered, it is possible to obtain the intensity as a function of horizontal, i.e. radial, position. For every position in horizontal direction, the image signal is integrated only in

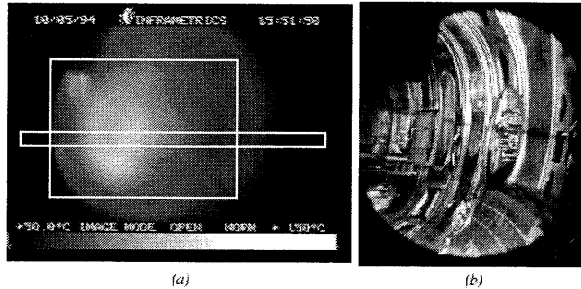


Figure 5.3: (a) Typical IR image of a runaway discharge, here at $t \approx 4$ s, with synchrotron radiation as the brighter spot. In the IR image, 2 examples of software defined integration boxes are shown, 1) including total synchrotron spot and 2) a narrow slit in equatorial plane. (b) A view inside TEXTOR-94, made with a normal photocamera from the same position and in the same direction as the IR camera takes its pictures.

the vertical direction over the slit width. The error made in the obtained profile due to the finite width of the slit is small when the slit is narrow. The result from this kind of image processing is a radial distribution profile of the synchrotron radiation.

5.2.3 Typical measurement

From the integration box that includes the total synchrotron spot (see figure 5.3(a)), the evolution of synchrotron radiation for two different discharges normalized to number of pixels is plotted in figure 5.4. For one of the discharges, also the result taken from the slit-shaped integration box is shown. In one case (#62788), the radiation level reaches a steady state at $t \approx 4$ s. Other cases have been observed where the synchrotron radiation does not reach a steady state, but rises continuously, which is ascribed to secondary generation [15]. An example of this is also shown in figure 5.4 (#64720). In this paper, we will not address the question why those two modes exist. Only cases for which the radiation reaches an equilibrium are considered.

In figure 5.5, the radial distribution at $t \approx 4$ s, taken from the narrow slit in figure 5.3(a), is shown. The maximum is shifted due to the Shafranov shift and the large drift of the runaway orbits. These and other aspects of the measurements are treated in detail in section 5.4.

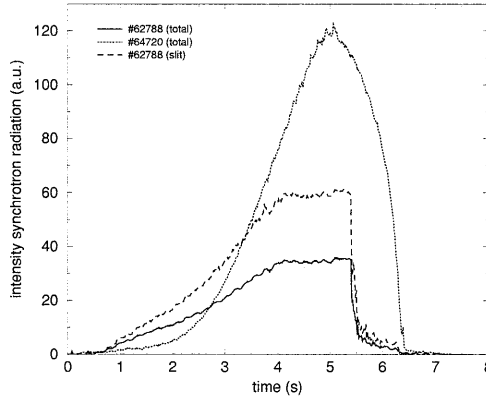


Figure 5.4: Two types of evolution of synchrotron radiation taken from the total spot integration box (see figure 5.3(a)) and the evolution of synchrotron radiation taken from the slit integration box (intensity normalized to pixel number). In the present paper, discharge #62788 is considered.

5.3 Method of data analysis

5.3.1 Transport model

In this paper, we assume that the transport of the runaways is diffusive. In general, diffusive processes are described by the diffusion equation

$$\frac{\partial n}{\partial t} = -\nabla \cdot \mathbf{\Gamma} + S \quad (5.2)$$

where n is the particle density, $\mathbf{\Gamma}$ the particle flux and S a source density. Possible convection is not taken into account, therefore the particle flux is related to the gradient of the density by Fick's law only

$$\mathbf{\Gamma} = -D \nabla n \quad (5.3)$$

where D is the diffusion coefficient. For the tokamak case, an axisymmetric cylindrical coordinate system is chosen. We consider the diffusion during steady state, where the loss of particles equals the generation, i.e. $\frac{\partial}{\partial t} n = 0$. Assuming the source density of the particles is only a function of r , i.e.

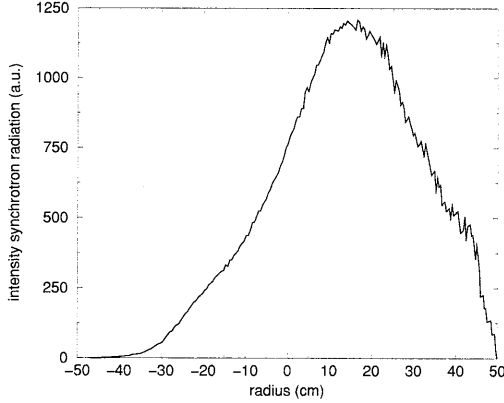


Figure 5.5: *Radial distribution of synchrotron radiation, taken from narrow slit (see figure 5.3), as function of minor radius.*

$S(r, \theta, z) = S(r)$, and taking the volume integral of (5.2), an expression for the radial particle flux is found

$$\Gamma(r) = \frac{1}{r} \int_0^r r' dr' S(r') \quad . \quad (5.4)$$

Combining (5.3) and (5.4), the relation between the radial diffusion coefficient to the (integrated) source density and gradient of the particle density is

$$D(r) = \left(\frac{1}{r} \int_0^r r' dr' S(r') \right) / \left(-\frac{\partial n}{\partial r}(r) \right) \quad . \quad (5.5)$$

If the source density and the gradient of the particle density could be measured, (5.5) provides a direct way of deriving the diffusion coefficient profile for particles under consideration.

5.3.2 Relation between intensity of radiation and number of runaways

To calculate the diffusion coefficient profile (5.5) for runaway electrons, the gradient of the runaway particle density n_r and information about the source

density has to be known. In this and the next subsection we will give a thorough justification, how to derive these runaway quantities from the intensity measurements.

According to Schwinger [17], the power emitted by one electron in a circular orbit in all directions and per wavelength interval is

$$\begin{aligned} \frac{dP^e}{d\lambda} &= \frac{4\pi m_e c^3 r_e}{\sqrt{3} \gamma^2 \lambda^3} \int_w^\infty K_{5/3}(\xi) d\xi \\ w &= \frac{4\pi R}{3\lambda\gamma^3} \end{aligned} \quad (5.6)$$

where m_e is the electron rest mass, c the speed of light, r_e is the classical Thomson electron radius, γ the relativistic factor and a measure of the electron energy, λ the wavelength of the emitted synchrotron radiation, R the radius of curvature and $K_{5/3}$ the modified Bessel function. The effect of changes in energy (i.e. in γ), pitch angle (which influence the effective radius of curvature R) and energy distribution on the synchrotron spectrum (5.6) was studied in [10]. With decreasing λ , the spectrum strongly decreases and because of strong energy and pitch angle dependence, the highest energy and largest pitch angle dominate the spectrum. Runaways that emit radiation in the wavelength range of the IR detector (i.e. $3 - 8 \mu\text{m}$), have an energy of at least 20 MeV. Therefore, all conclusions derived from the IR measurements only apply to these high energetic electrons. When a source profile is mentioned, then the source of these runaways with energy $W_r \geq 20$ MeV is meant, i.e. it is not the same as the birth rate of runaways [15]. Another consequence is that the effect of energy loss of a runaway below the 20 MeV limit is treated as a ‘particle loss’.

The power of the synchrotron radiation is determined by the number of runaways N_r and by their energy W_r (see (5.6)), $P = P(N_r, W_r)$. In fact, not the power, but the intensity of the synchrotron radiation is measured. This radiation is emitted in a cone shape as a consequence of the relativistic runaway energies. The pitch angle θ could in addition enhance the vertex angle of the radiation cone. This pitch angle does not change significantly after runaways reached energies of ca. 25 MeV and, therefore, approximately a constant part of this cone falls within the detector size. Averaging over a full toroidal transit of an electron, the measured intensity is proportional to the emitted power, and, hence, $I = I(N_r, W_r; r, \theta)$. To relate the measured intensity time trace to runaway quantities, it is necessary to know the energy distribution of the runaway population. However, this distribution is unknown and, therefore, assumptions concerning the runaway energy distribution function need to be made. To interpret the radial intensity profiles

as particle density profiles, the shape of the radial energy profile must be assumed as well.

In [10], a mono-energetic and a flat energy distribution have been considered. Measurements with three different filters in front of the IR camera showed that the determination of the energy is not very sensitive to the exact shape of the distribution function; the results for the two different extreme cases differ only 15%. Monte Carlo simulations show a fairly peaked energy dependence in the synchrotron radiation, with a maximum at 25 MeV. Moreover, runaways are first detected by the IR camera at an energy of about 20 MeV. They will gain only a few more MeV, up to an energy of about 25 MeV, because an equilibrium between energy gain from the accelerating electric field and energy loss because of interaction between magnetic field ripple and runaway motion is reached after $\Delta t \approx 1.5$ s [10]. In addition, as we noted before, the highest energy will dominate the spectrum. If we consider the measured data at $t > 2$ s, the assumption of mono-energetic distribution function will lead to a maximal error of 15%.

Such a mono-energetic distribution function implies a constant radial runaway energy profile. However, from drift orbit calculations [18], it is well known that the higher the runaway energy, the larger the drifts are that the orbits experience. For runaways with different energies, this leads, in a poloidal cross section, to a configuration of shifted, non-concentric, orbits. The energy profile of the runaways is therefore in the case of nonmono-energetic electrons an increasing function of major radius. Because the emitted intensity is energy-dependent (from (5.6)) and the density of higher energetic runaways is larger at the low field side, the nonmono-energetic case leads to an asymmetric I -profile. This gives a systematic error in determining ∇n_r from ∇I , assuming a mono-energetic distribution function. However, such a strong asymmetry is not observed, which is consistent with assumption of mono-energetic energy distribution and, therefore, also of the constant energy profile.

Based on these considerations, a mono-energetic distribution is assumed for the present experiment, so that the radiated power is a direct measure of the number of runaways N_r , or, the measured intensity is a measure of runaway density n_r . The gradient of the particle density, needed to determine the diffusion coefficient profile (5.5) for runaways, is therefore estimated from the intensity profiles $I(r) = I_0 i(r)$ normalized to the profile maximum I_0 , where $i(r)$ defines the profile shape.

5.3.3 Source density profile

The complete expression for the diffusion coefficient profile (5.5) in measured quantities is obtained by additionally determining the integrated source density of the 25 MeV runaways. First, we assume that the source is constant in time. This is justified, because only discharges that reach a steady state are considered.

The strength of the source density profile follows from the diffusion equation (5.2),

$$\left. \frac{\partial n}{\partial t} \right|_{t=t_0} = S \quad (5.7)$$

where t_0 is when the IR signal starts to rise and, therefore, the first term of the righthandside of (5.2) $-\nabla \cdot \mathbf{\Gamma}$ is negligible small (negligible amount of 25 MeV runaways). The total source, i.e. the volume integrated source density, is determined from the intensity time trace \tilde{I} , by measuring the time derivative at t_0 and normalizing to the value in steady state. Unfortunately, a calculation of the source density strength from the birth rate λ [15] using the plasma parameters is only possible within large uncertainty.

Because the shape of the source density profile can be derived only rather inaccurately, two extreme forms are considered, leading to an upper and lower limit of the diffusion coefficient. A self-consistent solution is found by iteration.

The first approximation of the source profile is given by a δ function

$$S_{\text{upper}}(r) = \frac{s\delta(r)}{r}, \quad \varepsilon < r < a \quad (5.8)$$

where a is the minor radius of the tokamak and $\varepsilon > 0$ small ¹. The source is located at $r = 0$, i.e. at the cylinder axis, and has an amplitude s . Earlier experiments [10] show that the birth rate λ is a strongly increasing function of the parameter ε , which scales with $T_e n_e^{-1}$. Because temperature profiles are more peaked in the plasma center than density profiles, λ is largest at the center. Consequently, runaways most likely reach the 20 MeV-threshold of the detection system first at the center of the plasma, which justifies (5.8). For this extreme of the source density profile, an upper limit $D_{r,\text{upper}}$ is found, because at a surface at radius r clearly too much of the source density is assumed within the cylindrical volume enclosed by the surface compared to a more realistic case with broader profiles and finite diffusion.

¹This footnote is not part of the reproduced paper. Actually, the source S_{upper} is zero on the given range of r because the delta function is only non-zero at $r = 0$. The source should be defined for all $0 < r < a$. Because of the cylindrical coordinate system, there is a factor $1/r$ in the definition, which drops out when S_{upper} is volume integrated.

The other extreme is a constant profile

$$S_{\text{lower}}(r) = \frac{2s}{a^2} \quad , \quad r < a \quad .$$

This extreme case of source density profile leads to a lower limit of the diffusion coefficient $D_{r,\text{lower}}$ of the runaways.

A self-consistent solution is found by assuming that the runaway distribution has a given width at the critical energy, and that this profile broadens during the acceleration due to diffusion with a constant D_r . In [10], it is derived that the width (HWHM) of the runaway creation zone is approximately 7 cm in TEXTOR. Therefore, for the third approximation of the source profile, a Gaussian birth rate distribution is assumed

$$S_{\text{it}} = sC \exp\left(-\left(\frac{r}{\sigma_1}\right)^2\right) \quad (5.9)$$

where C is a normalization constant and $\sigma_1 = [(\Delta r_{\text{HWHM}})^2/\ln 2]^{1/2}$ with $\Delta r_{\text{HWHM}} = 7$ cm. This iteration process converges to $D_{r,\text{it}}$, with the corresponding width of the 25 MeV runaway source profile.

We remark that it is likely that the diffusion coefficient is a decreasing function of the runaway energy (e.g. because larger orbit drifts result in a stronger averaging over fluctuations that could cause the diffusion). Therefore, $D_{r,\text{it}}$ is still an upper estimate.

5.3.4 Diffusion coefficient

Now, the different estimates of the runaway diffusion coefficient can be expressed in terms of the measured quantities I (from the profile measurements) and \tilde{I} (from the time trace measurements) depending on which shape is taken for the source density profile. From section 5.3.2, the density gradient

$$\frac{\partial n}{\partial r} \sim I_0 \frac{\partial i}{\partial r}$$

From section 5.3.3, the total source is given by

$$\int_0^a S(r) dV_r \sim \dot{I}(a)|_{t=t_0} / \tilde{I}(a)|_{t \rightarrow \infty}$$

where V_r is the volume within a surface with radius r , a is the minor radius and ∞ denotes steady state. For S_{upper} we finally find a diffusion coefficient

profile

$$D_{r,\text{upper}}(r) = - \frac{k \left(\frac{\dot{I}(a)|_{t=t_0}}{\dot{I}(a)|_{t \rightarrow \infty}} \right)}{r \left(\frac{\partial i}{\partial r} \right)} \quad (5.10)$$

where k is a constant depending on the chosen parametrization of the measured intensity profile $i(r)$. For S_{lower} ,

$$D_{r,\text{lower}}(r) = \left(\frac{r}{a} \right)^2 D_{r,\text{upper}}(r) \quad . \quad (5.11)$$

Since the upper limit is obtained for a narrow source profile, which implies a low D_r in the accelerating phase, whereas the flat source profile leading to $D_{r,\text{lower}}$ implies a high D_r , it is ensured that a self-consistent solution exists that is in between $D_{r,\text{lower}}$ and $D_{r,\text{upper}}$.

For the third approximation, C in S_{it} (5.9) is calculated from the total source strength. The expression for the diffusion coefficient becomes

$$D_{r,n} = \frac{\left[1 - \exp \left(- \left(\frac{r}{\sigma_n} \right)^2 \right) \right]}{\left[1 - \exp \left(- \left(\frac{a}{\sigma_n} \right)^2 \right) \right]} D_{r,\text{upper}} \quad (5.12)$$

where σ_n is the width calculated from $D_{r,n-1}$ after Δt .

5.4 Results

Figure 5.6 shows the line integrated density, the current, the loop voltage and the neutron signal for an Ohmic runaway discharge. The density is kept below $1.0 \times 10^{19} \text{ m}^{-3}$ to get a reasonable amount of high energetic runaways. The typical operation scenario for runaway discharges may be different from that in other tokamaks: in TEXTOR-94, it was verified that the runaways are not predominantly born at the start of the discharge during the high loop voltage phase, but throughout the low density discharge. The sudden bursts in the neutron signal at the end of the discharge are a result of runaway loss. For this shot, an evolution of the synchrotron radiation is measured within a slit as is discussed in section 5.2. In figure 5.4 the result was already shown (#62788). The figure shows that for this particular discharge, it takes about 0.5 s before the first synchrotron radiation is to be seen, i.e. before the 20 MeV energy threshold is reached. The amount of radiation is rising, until it becomes constant and a steady state is reached at $t \approx 4$ s. At $t \approx 5.5$ s, the

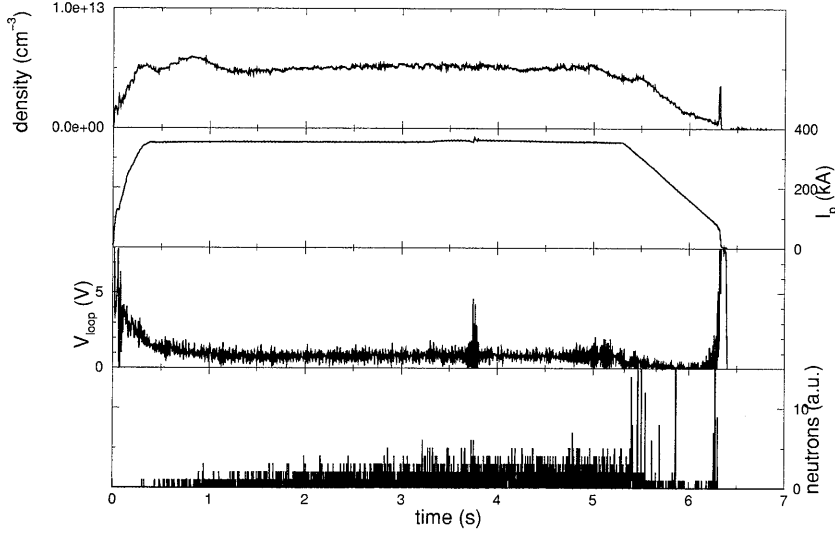


Figure 5.6: \bar{n}_e , I_p , V_{loop} and neutron signal of the analyzed discharge (#62788).

current decays and the synchrotron radiation disappears rapidly. From this figure, $t_0 = 0.5$ s, $\tilde{I}|_{t=0.5s}$ and $\tilde{I}|_{t \rightarrow \infty}$ are measured. At this time t_0 , the first synchrotron radiation appears, while the quantities n_e , T_e and electric field E are approximately in steady state.

In figure 5.7, the radial distribution profiles at different times of this shot are plotted. The dotted vertical line corresponds to the geometrical center of TEXTOR-94. The difference between the maxima of the profiles at $t = 4$ s and $t = 5$ s is 15 %, which is equivalent to the 'noise' in figure 5.4 (#62788) for $t > 4$ s. The maxima of the distributions are shifted by $\delta = 14 \pm 2$ cm to the low field side. This shift is a combination of the Shafranov shift (in TEXTOR-94 approximately 4 cm) and the drift due to the high energy of the runaways from which the radiation originates. Considering the profile at $t = 5$ s, i.e. at steady state, a triangle profile is a good first approximation, if the gradient $\partial i / \partial r$ is determined only in the range $r \in [20, 35]$ cm. For this parametrization, k in diffusion coefficient (5.10) is $a^2/6$.

The effect of the pitch angle θ is, according to [10], only measurable at the high field side of the tokamak. For this experiment, it means a correction of only a few centimeters. There is a negligible effect on the determination of the gradient $\partial n / \partial r$ by measuring $\partial I / \partial r$, because in the range that we consider,

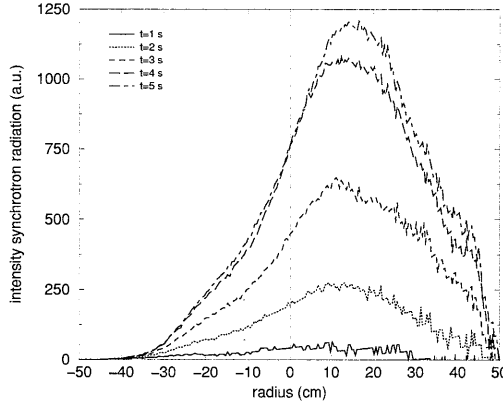


Figure 5.7: *Radial profiles of synchrotron radiation at different times as function of minor radius.*

θ has the same effect for all $r \in [20, 35]$ cm. The intensity measured at a radius $r_1 \in [20, 35]$ cm originates from runaways at $r_1 \leq r < r_{\max}$, where r_{\max} depends on θ and $r_{\max} - r_1 \equiv \Delta r$ is constant for all $r_1 \in [20, 35]$ cm. From the linearity of the gradient in I , it follows that the same must be valid for the gradient in n_r , so that the relation between $\partial I / \partial r$ and $\partial n / \partial r$ is independent of θ .

The measurements give the following upper limit for the runaway diffusion coefficient (using (5.10))

$$D_{r,\text{upper}}(r) = \frac{(2.2 \pm 0.1) \times 10^{-3}}{r[\text{m}]} \text{ m}^2\text{s}^{-1} .$$

The lower estimate of the diffusion coefficient is (from (5.11))

$$D_{r,\text{lower}}(r) = (10 \pm 1) \times 10^{-3} r[\text{m}] \text{ m}^2\text{s}^{-1} .$$

Starting with S_{it} , the iteration converges at a width of $\sigma \approx 23$ cm. The results for the different estimates are plotted in figure 5.8. At $r = 0.5a$, we find for the different coefficients

$$\begin{aligned} D_{r,\text{upper}} &\approx 10 \times 10^{-3} \text{ m}^2\text{s}^{-1} \\ D_{r,\text{lower}} &\approx 2 \times 10^{-3} \text{ m}^2\text{s}^{-1} \\ D_{r,\text{it}} &\approx 6 \times 10^{-3} \text{ m}^2\text{s}^{-1} . \end{aligned}$$

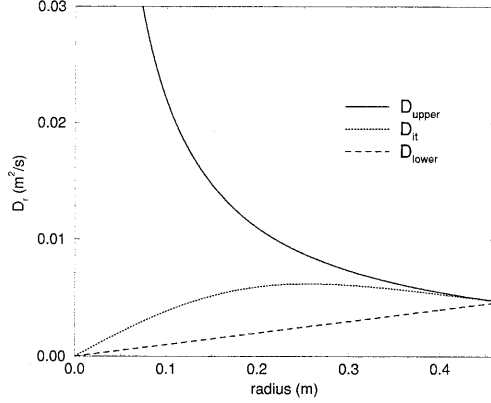


Figure 5.8: *r*-dependence of radial runaway diffusion coefficient. The figure shows the upper limit, lower limit, and the self-consistent solution found by iteration. The curves are based on measurements in the range $r \in [20, 35]$ cm.

The runaway diffusion coefficient D_r in the range $r \in [20, 35]$ cm is, therefore, to be expected to be of the order $10^{-2} \text{ m}^2\text{s}^{-1}$.

A rough estimate for the corresponding runaway confinement time (in the cylindrical case)

$$\tau_r \approx \frac{a^2}{5.6D_r} \quad (5.13)$$

gives $\tau_r > 3.5$ s, derived from $D_{r,\text{upper}}$.

5.5 Discussion

With the use of a simple diffusion model, it is possible to give an estimate of the radial diffusion coefficient for runaway electrons in TEXTOR-94 for the range of radii $r \in [20, 35]$ cm. Figure 5.8 shows that for $r = 0.5a$ this is $2 \times 10^{-3} \text{ m}^2\text{s}^{-1} < D_r < 10 \times 10^{-3} \text{ m}^2\text{s}^{-1}$.

Earlier runaway experiments at TEXTOR [10, 15] show for Ohmic discharges a lower limit of runaway confinement time of $\tau_r > 1$ s. This corresponds (using (5.13)) to an upper limit of the diffusion coefficient of $D_r < 0.04 \text{ m}^2\text{s}^{-1}$. In a so-called runaway snake [16], this upper limit was found

to be even lower, $D_r < 0.02 \text{ m}^2\text{s}^{-1}$, at $r \approx 0.3a$. The result derived in the present paper is in good agreement with these earlier results.

Runaway diffusion is best compared to thermal transport. Since runaways are effectively test particles, they are not subjected to ambipolar diffusion. Furthermore, runaways do not experience recycling effects as thermal particles do. Electron heat transport as determined by power balance analysis, for the type of discharges at hand, typically has $\chi_e \sim 1 \text{ m}^2\text{s}^{-1}$ [19], where χ_e denotes the electron diffusivity.

Hence, the measured runaway diffusion coefficient is found to be two to three orders smaller than the thermal electron diffusivity, a result that is in qualitative agreement with earlier experiments [5, 6]. There are several possible causes for this difference. Firstly, if classical, collision induced diffusion were prevailing, a similar difference would be expected. However, in that case both D_r and χ_e would be orders of magnitude smaller than the observed values. So, mechanisms are required to enhance both D_r and χ_e . In [5], it is suggested that thermal electron diffusion is dominated by electrostatic turbulence, which leaves the runaways unaffected. However, this leaves open the question of the small but finite runaway diffusion. Magnetic turbulence is another possible cause of enhanced transport of both runaway electrons and heat. Estimates of runaway diffusion in the presence of magnetic turbulence, commonly follow [20], which presumes a fully stochastic field throughout the tokamak. The test particle diffusion coefficient is estimated by

$$D \sim v_{\parallel} D_M \quad (5.14)$$

where v_{\parallel} is the velocity along the magnetic field lines. For the magnetic diffusion coefficient D_M is taken the quasilinear estimate

$$D_M = \pi q R_0 \langle b_e^2 \rangle \quad (5.15)$$

where $\langle \rangle$ denotes a flux surface average and $b_e = (\tilde{B}_r)/(B_T)$ with \tilde{B}_r the radial component of the perturbing magnetic field. This estimate leads to a higher diffusion rate for runaway electrons than thermal energy, in disagreement with the experimental result. Moreover, according to this estimate, the allowed level of $b_e < 10^{-6}$ for the measured runaway diffusion rate. Such a low level of magnetic turbulence is not expected in view of the measurements in Tore Supra [21]. However, there are several mechanisms that can reduce the effect of magnetic turbulence on runaway electrons.

It is unlikely that at acceptable perturbation levels of $b_e < 10^{-3}$ the entire field will be chaotic. Instead, chains of islands and good surfaces will remain [22]. As was pointed out in [23], in this situation the net diffusion of runaway electrons is determined by the insulating layers. Since in those

layers the runaway diffusion is much lower than that of the thermal electrons, the net value of D_r may be lower than χ_e . In this picture of turbulent layers, profile measurements of synchrotron radiation interpreted as runaway density profiles, would show steps in the gradient, which has not been observed. We note, however, that due to their high curvature B drift velocity runaway electrons do not follow an individual field line but average the B field over their drift orbit and have a smoothing effect on the measured profiles. The reduction of transport due to this averaging is estimated in [13], and could amount to two orders of magnitude for the 25 MeV runaway electrons in TEXTOR-94.

Another view of turbulent structure are stochastic cells, which exist for some time randomly distributed in space, decay and reappear at another location. This model is inspired by the observed filaments of the plasma current in RTP [24, 25]. Filaments are observed with a width of the order of 5-10 mm with a lifetime of hundreds of microseconds. Runaways complete a toroidal circle in ca. 30 ns. If a stochastic cell with a width of 1 cm lives for a few 100 μ s, the runaways will sufficiently often pass the cell to be deflected by one cell diameter $\Delta x \sim 0.01$ m. For $D_r < 10 \times 10^{-3} \text{ m}^2\text{s}^{-1}$ and with $D_r \approx (\Delta x)^2/\tau_{\text{cell}}$, a time scale $\tau_{\text{cell}} > 10$ ms is obtained. This time τ_{cell} is interpreted as the time after which a new stochastic cell close to the old one is born. The creation time of neighboring cells should be of the same order of magnitude as the decay time of the cell, to maintain a finite number of filaments. The measured lifetime of filaments and τ_{cell} differ a few orders of magnitude, which is not in favor for this turbulence model. It could be expected that the lifetime of filaments in TEXTOR-94 is larger than in RTP, which would lead to more consistency. It may be worth noting that a transport reducing effect of drift orbit shifts will be smaller in this turbulence model than the case of turbulent layers due to the randomness of the cells.

Finally, (5.14) is derived for conditions that may not be satisfied in a tokamak. In [22] the collisionless test particle diffusion is estimated based on a numerical treatment of the chaotic magnetic field. This resulted in a different scaling, with $D_r v_{\parallel}^{1/3}$, which strongly reduces the enhancement of runaway diffusion with respect to thermal diffusion. In conclusion, in the absence of a quantitative theory for test particle transport in a mixed field topology, it is not possible to estimate the magnetic turbulence level on the basis of the runaway confinement measurements.

At first glance, large differences exist between the results on runaway transport, quoted in the introduction. Figure (5.1) shows, however, that the runaway diffusion coefficient tends to decrease with increasing energy. Furthermore, we note that most of the prior experiments deal with runaway transport in the plasma edge. It is expected that the magnetic turbulence

Table 5.1: Summary of results on runaway diffusion and corresponding drift orbit shifts.

	LT-3	PLT	ORMAK	TEXT	ASDEX	JET	TEXTOR-94
W_r (MeV)	<0.3	0.4-1 8-23	10	1	1	1	25
D_r (m ² s ⁻¹)	1-50	0.06-0.1 0.4-0.8	0.01-1	0.25-2	0.07	0.2	<0.01
d (cm)	0.3	0.3 4-11	15	0.5	0.5	0.5	15
d/a (%)	4	1 10-30	65	2	1	0.5	10-30

in the plasma edge is higher than in the plasma core, which leads to a larger transport in the edge region than in the core. This, however, can not account for all the differences and certainly not for the differences between experiments both concerning the plasma core (e.g. in JET and TEXTOR-94). If we assume that the magnetic turbulence occurs as chains of islands between good surfaces, we can compare the transport reducing effect of the drift orbit shift for the different experiments. According to [10], the drift displacement can be given by

$$d = \frac{\bar{q}W_r}{ecB_T} \quad (5.16)$$

where \bar{q} is the average safety factor along the runaway orbit and W_r the runaway energy. In table 5.1, an overview is given of d and of the drift compared to minor radius. From [13], it follows that the reduction of transport due to the drifts in ASDEX, TEXT, LT-3 and JET could amount up to only one order of magnitude, whereas the reduction in TEXTOR-94 is two orders of magnitude. In [12], it is actually shown that in TEXT drift corrections are small. In ORMAK and PLT (results from photoactivation of limiter), the drift effect is comparable with that in TEXTOR-94. We suggest that in ORMAK and PLT (in case of high energy runaways), different from the other experiments, drift effects play a non-negligible role and that the differences in diffusion coefficient estimates between ORMAK and TEXTOR-94 are mainly due to a difference in turbulence level respectively in the edge and the core of a plasma. Note that most results of larger D_r for lower energetic runaways, as shown in fig 5.1 and again in table 5.1, are consistent with the statement in section 5.3.3 that during the acceleration phase runaways in TEXTOR-94 have a larger D_r than is assumed for calculation of $D_{r,it}$.

In conclusion, using synchrotron radiation profiles and evolution of the

synchrotron radiation from runaways, an upper limit of the runaway diffusion coefficient could be made, $D_r < 0.01 \text{ m}^2\text{s}^{-1}$. The measurement method we used in our experiments, gives, compared with most of the methods used in other tokamaks, direct information from the runaways and enables us to determine a relatively accurate diffusion rate of these runaways. Unfortunately, these runaway confinement measurements turn out to be less suitable for estimating the magnetic turbulence level, first of all because of failing quantitative theory of test particle transport in mixed field topologies, but also because of the large energy of the runaways in TEXTOR-94 which leads to a large reduction in diffusion in case of turbulence as chains of islands between good surfaces.

Acknowledgments

This work was performed under the Euratom-KFA and Euratom-FOM association agreements with financial support from NWO and Euratom.

References

- [1] Fussmann G 1979 *Nucl. Fusion* **19** 327
- [2] Strachan J D 1976 *Nucl. Fusion* **16** 743
- [3] Barnes C W, Strachan J D 1983 *Phys. Fluids* **26** 2668
- [4] Zweben S J, Swain D W, Fleischmann H H 1978 *Nucl. Fusion* **18** 1679
- [5] Catto P J, Myra J R, Wang P W, Wootton A J, R.D. Bengtson R D 1991 *Phys. Fluids B* **3** 2038
- [6] Myra J R, Catto P J, Wootton A J, Bengtson R D, Wang P W 1992 *Phys. Fluids B* **4** 2092
- [7] Kwon O J, Diamond P H, Wagner F, Fussmann G, ASDEX and NI Teams 1988 *Nucl. Fusion* **28** 1931
- [8] Barnes C W, Stavely J M, Strachan J D 1981 *Nucl. Fusion* **21** 1469
- [9] Esposito B, Martin-Solis R, van Belle P, Jarvis O N, Marcus F M, Sadler G, Fischer F, Froissard P, Adams J M, Cecil E, Watkins N 1996 *Plasma Phys. and Contr. Fusion* **38** 2035

- [10] Jaspers R J E 1995 *PhD Thesis* Eindhoven University of Technology, The Netherlands
- [11] de Rover M, Lopes Cardozo N J, Montvai A 1997 *Phys. Plasmas* **3** 4468
de Rover M, Lopes Cardozo N J, Montvai A 1997 *Phys. Plasmas* **3** 4478
- [12] Myra J R, Catto P J 1992 *Phys. Fluids B* **4** 176
- [13] Mynick H E, Strachan J D 1981 *Phys. Fluids* **24** 695
- [14] Finken K H, Watkins J G, Rusbüldt D, Corbett W J, Dippel K H, Goebel D M, Moyer R A 1990 *Nucl. Fusion* **30** 859
- [15] Jaspers R, Finken K H, Mank G, Hoenen F, Lopes Cardozo N J, Schüller F C 1993 *Nucl. Fusion* **33** 1775
- [16] Jaspers R, Lopes Cardozo N J, Finken K H, Schokker B C, Mank G, Fuchs G, Schüller F C 1994 *Phys. Rev. Lett.* **72** 4093
- [17] Schwinger J 1949 *Phys. Rev.* **75** 1912
- [18] Knoepfel H, Spong D A 1979 *Nucl. Fusion* **19** 785
- [19] Krämer-Flecken A, Waidmann G 1994 *Proc. of 21st EPS Conference on Controlled Fusion and Plasma Physics* (Montpellier) **18BI** 122
- [20] Rechester A B, Rosenbluth M N 1978 *Phys. Rev. Lett.* **40** 38
- [21] Zou X L, Colas L, Paume M, Chareau J M, Laurent L, Devynck P, Gresillon D 1995 *Phys. Rev. Lett.* **75** 1090
- [22] de Rover M 1996 *PhD Thesis* Eindhoven University of Technology, The Netherlands
- [23] Hegna C C, Callen J D 1993 *Phys. Fluids B* **5** 1804
- [24] Lopes Cardozo N J, Schüller F C, Barth C J, Chu C C, Pijper F J, Lok J, Oomens A A M 1994 *Phys. Rev. Lett.* **73** 256
- [25] Beurskens M N A, Barth C J, Lopes Cardozo N J, van der Meiden H J, RTP-team 1997 *Proc. of the 24th EPS Conference on Controlled Fusion and Plasma Physics* (Berchtesgaden) **21AII** 597

Chapter 6

Runaway transport during additional heating

In this chapter, runaway experiments with auxiliary heating are discussed. The first part of this chapter presents experimental evidence of the energy dependence of the runaway confinement time which is expected when magnetic turbulence is the main cause for runaway transport. This section is a reproduction of the letter 'Scale size of magnetic turbulence in tokamaks probed with 30 MeV electrons', by I.Entrop, N.J.Lopes Cardozo, R.Jaspers, K.H.Finken, that is submitted to Phys. Rev. Letters. The second part of this chapter is a more detailed discussion of the runaway transport measurements during heating. This part is meant to be submitted to Plasma Phys. and Contr. Fusion and, therefore, presented in paper format.

6.1 Scale size of magnetic turbulence in tokamaks probed with 30 MeV electrons

I. Entrop¹, N.J. Lopes Cardozo¹, R. Jaspers¹, K.H. Finken²
Partners in Trilateral Euregio Cluster:

¹FOM-Instituut voor Plasmafysica 'Rijnhuizen', Association

Euratom-FOM, P.O. Box 1207, 3430 BE Nieuwegein, The Netherlands

²Institut für Plasmaphysik, Forschungszentrum Jülich GmbH, EURATOM
 Association, D-52425 Jülich, Germany

Abstract

Measurements of synchrotron radiation emitted by 30 MeV runaway electrons in the TEXTOR-94 tokamak show that after switching on Neutral Beam Injection (NBI), the runaway population decays. The decay only starts after a significant delay, which decreases with increasing NBI heating power. This delay provides first direct evidence of the energy dependence of runaway confinement, which is expected if magnetic modes govern the loss of runaways. Application of the theory by Mynick and Strachan (Phys. Fluids **24**, 695 (1981)) yields estimates for the 'mode width' (δ) of magnetic perturbations: $\delta < 0.5$ cm in Ohmic discharges, increasing to $\delta = 4.4$ cm for 0.6 MW NBI.

One of the outstanding issues in thermonuclear fusion research remains the anomalous conduction of heat by the electrons in the plasma. In a tokamak, the hot plasma is confined in a toroidal geometry by means of magnetic fields. The field topology is such that field lines lie on nested toroidal surfaces. Transport in the direction perpendicular to the surfaces is reduced by many orders of magnitude by the presence of the field. However, the measured heat fluxes carried by the electrons exceed the theoretically achievable minimum by 1-2 orders of magnitude. This anomaly is generally ascribed to turbulence, which may be of electrostatic or of magnetic nature, or both. There has been extensive research into transport caused by electrostatic fluctuations. Recently, means have been found to greatly reduce the heat loss caused by these [1]. Magnetic turbulence is more difficult to diagnose, since perturbing fields of the order $\tilde{B}/B = 10^{-5}$ can already contribute significantly to the heat flux carried by the electrons. The only direct measurements of \tilde{B} in the core of a tokamak plasma, using the cross-polarization scattering of microwaves, did show the presence of \tilde{B} at transport relevant levels in Tore Supra [2, 3].

Electrons with energy much higher than the thermal energy in principle can provide a probe to study magnetic turbulence, since diffusion due to

electrostatic turbulence scales with v^{-1} , whereas the magnetically induced diffusion scales as v , where v is the electron velocity. Moreover, since in a plasma the mean free path of an electron scales as v^4 , collisional transport is negligibly small for high energy electrons. The absence of collisions is also the reason why in tokamak plasmas of sufficiently low density a small fraction of the electrons (so-called runaway electrons) undergo a free fall acceleration and can reach energies in the MeV range, in a background plasma with a temperature of ~ 1 keV.

In several studies runaway electrons have been used to assess magnetic turbulence. One principal difficulty is that runaway electrons in the 1 MeV energy range cannot be diagnosed until they leave the plasma and hit the wall and produce X-rays. Thus, in [4] experimental techniques have been used to probe magnetic turbulence in the edge of the plasma. Direct observation of runaway electrons in the center of the plasma column has been performed at the TEXTOR-94 experiment, making use of the synchrotron emission. This method diagnoses runaway electrons in a much higher energy range, typically 25–30 MeV. The high energy poses another problem. The orbits of electrons of such high energy are shifted with respect to the magnetic field topology by a few cm, which strongly reduces their sensitivity to magnetic perturbations with a radial correlation length smaller than this orbit shift [5]. In fact, this orbit shift is the reason why high energy runaway electrons are often observed to have much better confinement than thermal electrons (e.g. [6, 7]).

So, the question is: how can the observable high energy runaway electrons be used to probe magnetic turbulence with a scale much smaller than their orbit shift.

In this Letter, an analysis is presented based on a novel observation: when auxiliary heating is applied to a plasma with a pre-existing runaway population, this population is observed to decrease. Clearly, the runaway confinement is deteriorated by the power input, which is expected since it is well known that confinement of heat and thermal particles also degrades with increasing heating power. However, the decline of the runaway population does not start instantaneously after the heating is switched on, but is significantly delayed. It is shown that this delay is due to loss of runaway confinement at a lower energy, which only later appears as reduced influx of observable runaway electrons at high energy. If there is a critical energy below which the runaway electrons are lost, the delay time is the time electrons at the critical energy need to be accelerated to the energy where they become observable. Thus, the delay time can be related to the critical energy, and so to the radial scale length of the magnetic turbulence.

In [5] the energy dependence of runaway confinement, based on the averaging effect of the orbit shift, is calculated and related to the 'mode width' δ

of the magnetic perturbations. This theory has been applied to the present data to refine the estimate of the radial scale length of the magnetic perturbations. Since the delay depends on the level of NBI, so does the δ . Thus, from the dynamic evolution after NBI switch-on, of a runaway population at 30 MeV, conclusions can be drawn on the grain size of magnetic turbulence as a function of NBI power.

The experiments were carried out in the TEXTOR-94 tokamak, with major radius $R_0 = 1.75$ m, minor radius $a = 0.46$ m, toroidal magnetic field $B_\phi = 2.2$ T, toroidal plasma current $I_p = 350$ kA, circular cross section. The target plasmas had line averaged electron density $\bar{n}_e = 0.6 \times 10^{19} \text{ m}^{-3}$. In such discharges a runaway population develops which is diagnosed by measuring the synchrotron emission with an infrared camera viewing the plasma tangentially, in the direction of electron approach (see Fig. 6.1). The measuring technique is described in Refs. [7–9].

In these discharges, both the primary generation (electrons in the tail of the velocity distribution crossing the critical runaway energy) and secondary generation process (in which an already existing runaway kicks a thermal electron across the critical runaway energy [10]), are important. The latter process results in an exponential growth of the population, as witnessed by the infrared signal (Fig. 6.1) [11], and is independent of the plasma density.

The balance between the energy gain from the toroidal electric field and the energy loss through synchrotron radiation is reached at ~ 30 MeV [9]. Monte Carlo simulations showed that the velocity distribution develops a broad peak near this energy. The synchrotron emission is a strong function of the runaway energy, so that the infrared signal is dominated by the most energetic electrons in the distribution.

In the experiments described in this paper, additional plasma heating is applied using NBI, with power levels up to 0.6 MW. The Ohmic dissipation in the target plasma is ~ 0.4 MW. The NBI is switched on at $t = 3$ s, for an interval of 1.5 s. For comparison, the energy confinement time of the target plasma is $\tau_E \approx 20$ ms, the global current diffusion time $\tau_c \approx 300$ ms. After the switch-on of the NBI, \bar{n}_e increases. This is a spurious effect in the present experiment, which will be discussed later.

In the Ohmic phase the runaway confinement time (τ_r) is excellent, $\tau_r > 3.5$ s [7], and the infrared signal shows an exponential rise. During the NBI interval, the infrared signals start to decrease, with a rate depending on the NBI power. Typical traces are shown in Fig. 6.2.

Note that, especially for the lower power levels, the signals continue to rise for up to 1 s, before the decay starts. It is this continued rise for which a physical mechanism must be found.

To interpret these signals, a simulation code has been used which calculates the synchrotron emission taking into account the primary and secondary generation, the evolution of the runaway population in velocity space, and the diffusion in real space.

First, the effects of i) a change of the runaway diffusion coefficient, and ii) a change of the toroidal electric field as a result of NBI (either due to heating, or to current drive) were investigated. Also the combination of i) and ii) was studied. It was found that while these mechanisms do lead to a decay of the synchrotron emission, the response is immediate. The continued growth of the signal could not be reproduced.

Secondly, the possible increase of \bar{n}_e is considered. Since the signals are well into the domain where secondary generation dominates, an increase of \bar{n}_e does not affect the generation rate. Experiments were carried out in which gas puffs were applied to a target plasma without additional heating, to study the effect of the density increase alone. In those experiments the \bar{n}_e increase was typically 200%. It was found that the gas puff did result in a roll over of the IR signals, with delay times of 0.6 to more than 1.5 s. In comparison, for the NBI discharges presented here, the increase of \bar{n}_e is negligible for < 0.2 MW NBI, about 70% for 0.4 MW, increasing to 100% at 0.6 MW. We conclude that the contribution of the spurious \bar{n}_e increase to the roll over of the signals is small. Finally, since an increase of \bar{n}_e does not affect the runaway generation its effect on the IR signal must be ascribed to a deterioration of runaway confinement. It can therefore be treated on the same footing as the application of NBI power.

As a third possibility, an energy dependent change of runaway confinement was investigated, along the lines set out in the introduction. Simulations were performed in which it was assumed that before NBI, $\tau_r = 5$ s independent of the electron energy, whereas during NBI $\tau_r = 0.1$ s for $W < W_{\text{step}}$, and $\tau_r = 5$ s for $W \geq W_{\text{step}}$, where W is the energy of the runaway electron. Typical results are given in Fig. 6.3, showing that this energy dependence does produce signal shapes very similar to those observed in the experiment.

From these simulations we conclude, that of the various mechanisms that were considered, only an energy dependent runaway confinement can qualitatively reproduce the observations. This constitutes the first experimental proof of an energy dependent runaway confinement such as might be expected due to the averaging effect of the orbit shift.

There is a degree of arbitrariness in the choice of τ_r below W_{step} . Further, the step function is only the simplest choice to test the viability of the concept, and has no physical justification. Nonetheless, the result is fairly robust: to achieve delay times that are in the range from 1 s (which is approximately the time a 100 keV electron needs to be accelerated to the 'visible'

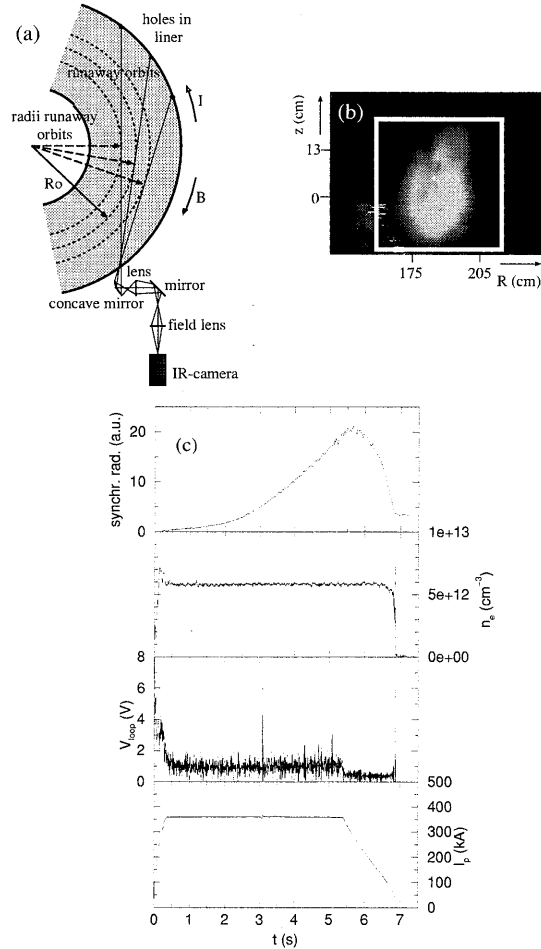


Figure 6.1: (a) Set-up for detection of runaway electrons in TEXTOR-94. (b) Typical IR picture showing the synchrotron radiation in a poloidal projection. Indicated is a software defined integration box. The evolution of the synchrotron radiation follows from the integrated signal within this box. Thermal background is subtracted. (c) Time evolution of synchrotron radiation, line averaged density, loop voltage and plasma current in an Ohmic runaway discharge.

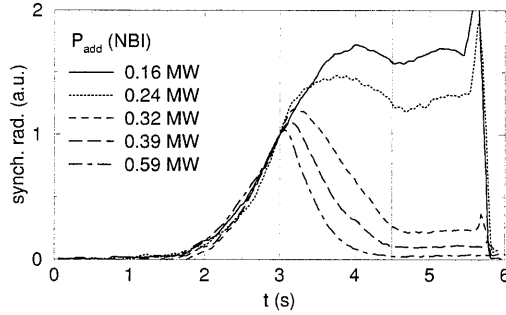


Figure 6.2: Measured radiation evolutions of runaway discharges. At $t = 3$ s, NBI is applied for 1.5 s, as indicated by the lines. The current flat top ends at about $t = 5$ s. The curves are normalized at their synchrotron radiation level at $t = 3$ s.

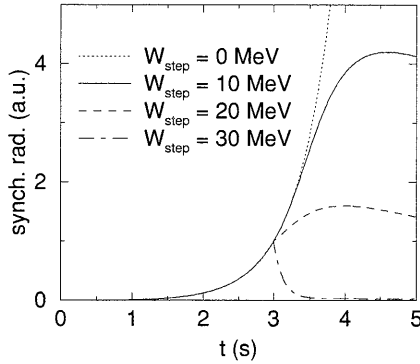


Figure 6.3: Simulated radiation signals where at $t = 3$ s the confinement time of runaways changes from 5 s to 0.1 s for runaways with $W < W_{\text{step}}$.

30 MeV) down to 0.1 s or less, clearly the critical energy must vary in the range 100 keV to 30MeV. The orbit shifts corresponding to these energies are 0.02 – 6 cm.

To estimate the grain size of the magnetic turbulence, a further analysis has been made adopting the theory of transport reduction due to orbit shift averaging by Mynick and Strachan [5]. This gives a prescription of the runaway confinement as a function of energy, determined by two parameters: a) the width δ of the magnetic mode; b) the background transport, i.e. the confinement of runaway electrons at an energy at which no transport reduction occurs. Further, the discharge parameters R_0 , B_ϕ and I_p are used to evaluate the absolute value of the orbit shift d_r according to $d_r(W) = qW/(eB_\phi c)$ with q the average safety factor. The energy dependent reduction of confinement, presented in a graph in [5], is represented by the expression

$$\frac{\tau_r}{\tau_{r,0}} \approx \left(1 + 1.1 \frac{d_r}{\delta} \right)^{5.7}$$

in the present simulations. Simulations are made in which the mode width δ is a control parameter, which is systematically varied between simulations. The reduction curve is calibrated in absolute sense by equating the test particle transport at low energy ($\tau_{r,0}$) to thermal confinement, with a correction factor for velocity, as is prescribed in [5].

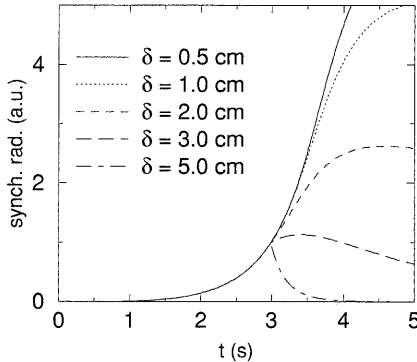


Figure 6.4: *Simulated radiation signals where at $t = 3$ s the averaged mode width δ is changed. Before $t = 3$ s, $\delta = 0.2$ cm, after $t = 3$ s, $\delta = 0.5 - 5$ cm. $\tau_E = 20$ ms.*

Figure 6.4 depicts examples of simulated signals, showing that with the theoretical expression for the energy dependent confinement reduction indeed

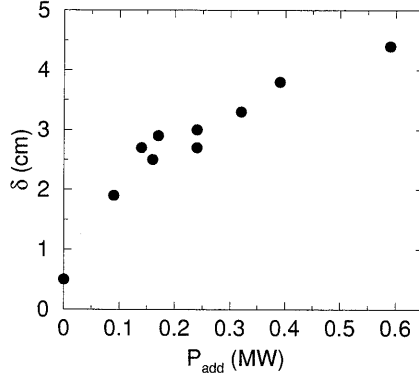


Figure 6.5: *Relation between averaged mode width δ and additional heating power P_{add} derived from a comparison between simulated and measured radiation signals.*

signals are obtained that are similar to the observed ones. From a comparison of the simulated and measured signals, the free parameter δ , i.e. the width of the perturbing modes is found for the different NBI power levels used in the experiment. The result is given in Fig. 6.5.

The figure shows that δ is an increasing function of the NBI power. The absolute values depend on the calibration of the reduction curve, which is rather uncertain. However, since the reduction curve is very steep, the absolute calibration is not a sensitive parameter; varying it by an order of magnitude changes the resulting value of δ by only a factor two.

The values are quite similar to measurements of the radial correlation length of density fluctuations measured with correlation reflectometry in JET [12].

Interpreting the mode width as the width of chains of magnetic islands, the perturbing field can be estimated. Here it is important to note that in order for the runaways to be lost due to magnetic turbulence, the plasma must be filled with chains of islands. A region with good surfaces would act as a very effective transport barrier [13]. This, together with the estimated mode width of several cm, implies poloidal mode numbers of at least ≈ 10 . The typical perturbing field is then estimated at $\tilde{B}/B = 2 \times 10^{-5}$ for Ohmic discharges increasing to $\tilde{B}/B = 10^{-3}$ for 0.6 MW NBI. This compares well with the values of \tilde{B}/B measured in Tore Supra [2,3].

In conclusion, we have shown that upon application of NBI, the population of 30 MeV runaway electrons in TEXTOR-94 decays, but that this

decay only starts after a delay of up to 1 s. Simulations showed that only an energy dependent runaway confinement can account for this delay. The delay times are associated to critical energies below which the increased runaway loss sets in. Electrons at these energies have an orbit shift of typically 0.02 – 6 cm. By application of the theory for orbit shift suppression of runaway transport in the presence of magnetic turbulence, it was found that the perturbing magnetic modes have a typical mode width of < 0.5 cm in Ohmic discharges, increasing to 4.4 cm at 0.6 MW NBI.

This work was done under the Euratom-KFA and Euratom-FOM association agreements with financial support from NWO and Euratom.

References

- [1] C.M. Greenfield *et al*, Phys. Plasmas **4** 1596 (1997); E. Mazzucato *et al*, Phys. Rev. Lett. **77**, 3145 (1996).
- [2] X.L. Zou *et al*, Phys. Rev. Lett. **75**, 1090 (1995).
- [3] L. Colas *et al*. Nucl. Fusion **38**, 903 (1998).
- [4] J.D. Strachan, Nucl. Fusion **16**, 743 (1976); C.W. Barnes, J.M. Stavelly and J.D. Strachan, Nucl. Fusion **21**, 1469 (1981); C.W. Barnes and J.D. Strachan, Phys. Fluids **26**, 2668 (1983); S.J. Zweben, D.W. Swain and H.H. Fleischmann, Nucl. Fusion **18**, 1679 (1978); P.J. Catto *et al*, Phys. Fluids B **3**, 2038 (1991); J.R. Myra *et al*, Phys. Fluids B **4**, 2092 (1992); O.J. Kwon *et al*, Nucl. Fusion **28**, 1931 (1988).
- [5] H.E. Mynick and J.D. Strachan, Phys. Fluids **24**, 695 (1981).
- [6] R. Jaspers *et al*, Phys. Rev. Lett. **72**, 4093 (1994).
- [7] I. Entrop, N.J. Lopes Cardozo, R. Jaspers and K.H. Finken, Plasma Phys. and Contr. Fusion **40**, 1513 (1998).
- [8] K.H. Finken *et al*, Nucl. Fusion **30**, 859 (1990).
- [9] R. Jaspers, Ph.D. thesis, Eindhoven University of Technology, The Netherlands, 1995.
- [10] N.T. Besedin and I.M. Pankratov, Nucl. Fusion **26**, 807 (1986).
- [11] R. Jaspers *et al*, Nucl. Fusion **33**, 1775 (1993).

- [12] A.E. Costley, P. Cripwell and T. Fukuda, in *Proceedings of the 21st EPS Conf. of Contr. Fusion and Plasma Physics* (Innsbruck, 1994), Part I, p.199.
- [13] C.C. Hegna and J.D. Callen, *Phys Fluids* **B4**, 1804 (1993).

6.2 Runaway electron transport during additional heating in TEXTOR-94

I. Entrop¹, R. Jaspers¹, N.J. Lopes Cardozo¹,
K.H. Finken²

Partners in the Trilateral Euregio Cluster:

¹FOM Instituut voor Plasmafysica 'Rijnhuizen', Association
Euratom-FOM, PO Box 1207, 3430 BE Nieuwegein, Netherlands

²Institut für Plasmaphysik, Association Euratom-KFA, Forschungszentrum
Jülich GmbH, 52425 Jülich, Germany

Abstract

Measurements of synchrotron radiation emitted by 30 MeV runaway electrons in the TEXTOR-94 tokamak are reported. The effect of auxiliary heating (neutral beam injection (NBI) and ion cyclotron resonance heating (ICRH)) on the confinement of runaways is investigated. In the Ohmic phase of the discharge runaway confinement is extremely good, and the population grows exponentially. Some time (up to 1 s) after the heating is switched on, the runaway population starts to decrease. The time delay and the rate of decay are functions (decreasing and increasing, resp.) of the heating power.

The signals are interpreted using a simulation code, in which various loss processes can be implemented. To explain the delayed reaction of the synchrotron radiation signal after switching on the heating, an energy dependence of runaway confinement must be invoked; the loss of lower energy runaways appears as a lack of radiating high energy runaways only after the time necessary for acceleration.

This energy dependent confinement has been predicted theoretically by Mynick and Strachan, *Phys. Fluids* 24 (1981) p. 695, based on the energy dependent orbit shift which averages out the effect of magnetic perturbations. Application of this theory to the present data leads to an estimate of $\delta < 0.5$ cm in Ohmic discharges, to $\delta \approx 4$ cm for 0.6 MW neutral beam heating, δ being the typical 'mode width' of the magnetic perturbations. Correspondingly, typical magnetic field perturbations $\tilde{B}_r/B = 2 \times 10^{-5}$ for Ohmic discharges and 1×10^{-3} for 0.6 MW NBI are estimated.

6.2.1 Introduction

The phenomenon of electron runaway plays a role in different fields of research within plasmaphysics. For future fusion reactors, it is important to avoid large amounts of runaway electrons with high energy, because they can

severely damage the reactor vessel. A good understanding of the different generation processes is therefore necessary [1–3]. Another field of investigation concerns the understanding of anomalous transport. Because runaway transport is assumed to be mainly dominated by magnetic field perturbations, the study of runaway confinement could be a tool to investigate the role of magnetic perturbations in anomalous transport [4–6]. Also, large magnetic structures can be studied using runaways [7]. This paper concentrates on the study of runaway transport during additional heating. The aim is to investigate the influence of the heating on magnetic turbulence.

In [8], measurements of runaway transport in Ohmic runaway discharges have been described. An expression was found for the diffusion coefficient as function of minor radius. At half radius, typical values are $0.002 \text{ m}^2\text{s}^{-1} < D_r < 0.010 \text{ m}^2\text{s}^{-1}$. Following [9], the upper limit for the runaway diffusion coefficient led to an extremely low estimate for the magnetic turbulence level \tilde{B}_r/B of 10^{-6} , where \tilde{B}_r is the radial component of the perturbing magnetic field and B the magnetic field. Suggested explanations for that were, first, the drift orbit averaging effects due to the relatively large orbit shift of the high energetic runaways and, secondly, the fact that the magnetic field structure during a steady state, non-disrupting, discharge is far from completely stochastic as is the starting point for the derivation in [9].

Despite the drift orbit averaging effects of high energetic runaway electrons, it is interesting to study runaway confinement during additional heating. First experiments [10,11] have shown a degradation of runaway confinement when increasing amounts of heating power were applied. In this paper, a detailed study of runaway discharges with additional heating is presented. The main questions to be answered are: What is the effect of additional heating on runaway confinement? How is this effect related to magnetic turbulence? Can high energy runaway electrons, with an orbit shift of several cm, be used to probe magnetic turbulence with a scale smaller than that?

To answer these questions, additional heating at different amounts of power, either by neutral beam injection (NBI) or by ion cyclotron resonance heating (ICRH), is applied to typical runaway discharges. The synchrotron radiation emitted by the relativistic runaways is measured. The behavior of the runaway electrons under heating conditions is derived from the radiation signals. To account for the different effects in the interpretation, a simulation code has been developed which computes the evolution of the runaway population in phase space, accounting for possible variations in the source (generation) and loss (enhanced transport) terms, as well as the measured loop voltage. It is essential to carefully model the evolution in velocity space, since e.g. a loss on runaway electrons at low energy only shows up in the synchrotron emission after this 'gap' in distribution function has been ac-

celerated to the energy where significant synchrotron radiation is emitted, typically 25 – 30 MeV. In the measured signals, indeed a delayed response is observed after the auxiliary heating is switched on. This delay is characteristic of a reduction of confinement of runaways at low energy. The theory of Mynick and Strachan [4] is used to relate the energy dependence of runaway confinement time to the typical size and level of magnetic turbulence.

In section 6.2.2, relevant formulas concerning runaway generation processes and synchrotron radiation which are implemented into the code for simulating the radiation evolutions are presented. Runaway electron transport is shortly discussed. The detection method of runaways in TEXTOR-94 and the observations are presented in section 6.2.3 and 6.2.4, respectively. In section 6.2.5, simulations of radiation signals of runaway discharges with additional heating that qualitatively explain the observed shape of radiation signals are shown. In section 6.2.6, the theoretical model of Mynick and Strachan is used to derive size and level of magnetic turbulence from the observed shape of radiation evolutions. Finally, in section 6.2.7, the results are discussed.

6.2.2 Theory

Runaway generation

Two runaway generation processes are known. First, there is the primary generation where the change in runaway density n_r is given by

$$\frac{dn_{r,pr}}{dt} = \lambda_r \nu_e n_e \quad (6.1)$$

with λ_r the runaway birth rate, ν_e the collision frequency of (thermal) electrons and n_e the electron density. Birth rate λ_r is an exponential function of $\varepsilon = E/E_c$, with the critical electric field $E_c = e^3 \ln \Lambda n_e / (4\pi \epsilon_0^2 m_e v_{th})$, where e and m_e are the electron charge and mass, $\ln \Lambda$ the Coulomb logarithm and v_{th} the thermal electron velocity (to give the birth rate an explicit effective ion charge number Z_{eff} -dependence (see for instance [12]), the above definition of E_c does not contain Z_{eff}).

Second, already existing runaway electrons can kick thermal electrons into the runaway regime by close Coulomb collisions

$$\frac{dn_{r,sec}}{dt} = \frac{n_r}{t_0} \quad (6.2)$$

where according to [13]

$$t_0 = \frac{\sqrt{12} \ln \Lambda m_e c (2 + Z_{eff})}{9eE} \quad (6.3)$$

is the time within which a runaway electron creates another runaway electron. This process is referred to as secondary generation. The secondary generation process is in first approximation independent of n_e . The n_e dependence in the collision frequency of the already existing runaways, $\nu_{\text{sec}} \approx \sigma(\Delta W)n_e c$ with σ the cross section, cancels out when the critical electron energy at which a runaway is created, $W_c \approx e^3 \ln \Lambda n_e (2 + Z_{\text{eff}}) / (8\pi \epsilon_0^2 E)$, is taken for the minimum energy transfer, $\Delta W \approx W_c$. In TEXTOR-94, the critical energy is about 100 keV.

In [12], the runaway density is calculated analytically as function of time, including primary and secondary generation,

$$n_r(t) = \lambda_r \nu_e n_e t_{\text{eff}} (\exp(t/t_{\text{eff}}) - 1) + n_r(0) \exp(t/t_{\text{eff}}) \quad (6.4)$$

An effective time t_{eff} was introduced, $t_{\text{eff}}^{-1} = t_0^{-1} - \tau_r^{-1}$, where τ_r is the runaway confinement time. A small t_{eff} means a relatively strong exponential rise in n_r . When t_0 and τ_r are such that t_{eff} becomes negative, n_r decays in time.

Synchrotron radiation

The power radiated by one electron that moves on a circular orbit per wavelength interval is approximated by [14,15]

$$\frac{dP}{d\lambda} \approx \pi m_e c^3 r_e \sqrt{\frac{2}{R\lambda^5 \gamma}} \exp(-4\pi R/3\lambda\gamma^3) \quad (6.5)$$

with r_e the classical Thomson electron radius, γ the relativistic factor and measure of runaway electron energy and R the radius of curvature. The power of a runaway electron in a tokamak is approximated by eq. (6.5) with R the helical runaway orbit, $R^{-1} \approx (1 - \theta^2)/R_0 + eB\theta/(m_e c\gamma)$. Here, R_0 is the major radius and $\theta = v_{\perp}/v_{\parallel}$ is the runaway pitch angle. Integration over the full wavelength spectrum gives $P_{\text{syn}} = 2r_e m_e c^3 \gamma^4 / (3R^2)$. The energy evolution of one electron, $\gamma(t)$, is determined from the difference between the amount of runaway energy W_r gained from the electric field and the amount of energy lost by radiation, $dW_r/dt = m_e c^2 (d\gamma/dt) = P_E - P_{\text{syn}}$ with $P_E = eEc$. In TEXTOR-94, the radiation equilibrium ($P_E - P_{\text{rad}} = 0$) limits the runaway energy at 30 MeV ($\theta = 0.1$).

Several other mechanisms can limit the runaway electron energy. In TEXTOR-94, the most relevant of these mechanisms is a resonance between the runaway electron motion and the magnetic field ripple [16]. Monte Carlo simulations [10] have shown that an effective energy blocking occurs already at energies < 30 MeV. This is approximately equal to the radiation energy limit (for $\theta = 0.1$).

Runaway transport

A quasilinear collisionless estimate of the perpendicular electron transport coefficient due to magnetic perturbations is given by [9] as $D \approx \pi q R_0 v_{\parallel} (\tilde{B}_r/B)^2$ with v_{\parallel} the electron velocity parallel to the magnetic field and q the averaged safety factor along the runaway electron orbit. Transport due to electrostatic fluctuations is proportional to v_{\parallel}^{-1} . Because of the relativistic energies of runaway electrons, we assume that the runaway transport is mainly determined by magnetic fluctuations.

In [4, 5], it is pointed out that the electron drift orbit shift, d_r , due to magnetic field gradient and curvature, averages the effect of magnetic field perturbations on runaway transport. A particle without drift runs along a constant-phase line in the (ϑ, ϕ) plane of the mode rational flux surface. The magnetic field runs parallel to the lines of constant phase. The driftless particle receives a kick from the mode in the same direction at all points along its trajectory. Particles with large orbit shifts, i.e. particles with large energy, have an oscillating trajectory in the (ϑ, ϕ) plane. Hence, these particles experience perturbations from the mode of varying phase in one transit period. This phase average of the radial displacement due to the mode is less than the maximum amplitude of the mode for drifts $d_r \gtrsim \pi/k_{\perp}$ where k_{\perp} is the perpendicular wave number of the perturbation. Secondly, a runaway electron with $d_r \gtrsim \delta$, where δ is the average mode width of the perturbation, senses the mode only a fraction of its transit period due to the shift. This causes an additional reduction in coupling strength of the electron with the mode. The total transport arising from the sum of the contributions of all modes, is therefore reduced.

The runaway electrons in TEXTOR-94 reach relativistic energies which lead to a considerable drift orbit shift, in first order approximation given by

$$d_r \approx qW_r/eBc = q\gamma m_e c/eB \quad (6.6)$$

where again q is the averaged safety factor along the runaway electron orbit and γ is the relativistic factor. In [17], in which the drift orbit topology of relativistic particles is described, it is shown that higher order energy effects increase the drift orbit shift. For the energy range of the runaway electrons in TEXTOR-94, the correction to eq. (6.6) due to these higher order energy effects is, however, smaller than 1% and negligible for the purposes of this paper.

6.2.3 Runaway detection in TEXTOR-94

Runaways in TEXTOR-94 are detected by the measurement of the synchrotron radiation they emit forwardly in a small cone with half vertex angle $1/\gamma$. The radiation is in the infrared (IR) range of wavelengths. With an IR camera, viewing tangentially into the plasma in direction of electron approach, poloidal projections of the synchrotron radiation cone coming from the toroidal runaway beam are made (detected wavelengths at TEXTOR-94 $\lambda \in [3, 8] \mu\text{m}$). The IR pictures are stored on video tape during the experiments and processed afterwards. The time evolution of the synchrotron radiation is deduced by integration of the synchrotron intensity within a software defined box in the IR pictures. Figure 6.6 shows the set-up, a typical IR picture of the poloidal projection and the evolution of the radiation for an Ohmic runaway discharge. Also, the evolutions of line averaged density \bar{n}_e , loop voltage V_{loop} and plasma current I_p are shown.

When a constant part of the synchrotron radiation cone is falling into the detector and when we average over a full toroidal transit of an electron, then the measured intensity is a function of the total number of runaway electrons and of their energy. No measurements on the exact energy distribution are available. In the interpretation of previous experiments [7, 8, 11], a mono-energetic energy distribution of 25 MeV runaways was assumed. Monte Carlo simulations show a peaked energy dependence of synchrotron radiation with a maximum at 25 MeV and also measurements show that within an error of 15%, no difference between a flat or a mono-energetic distribution can be recognized from spectral measurements [10]. Under the assumption of mono-energetic energy distribution, the intensity evolution can be interpreted as the evolution of total number of runaways N_r .

6.2.4 Observations

Experiments

Experiments were done in the TEXTOR-94 tokamak, which has major radius $R_0 = 1.75$ m and minor radius $a = 0.46$ m. During the experiments, the toroidal magnetic field was $B = 2.2$ T, and the plasma current I_p varied from experiment to experiment in the range 350-450 kA. Ohmic runaway discharges can be made very reproducible in TEXTOR-94. As long as the line averaged density is kept low, $\bar{n}_e < 1 \times 10^{19} \text{ m}^{-3}$, the generation of runaways in the plasma center during the flat top phase of the discharge is achieved. For the experiments presented in this paper, NBI was applied in a power range from 0.1 to 1.3 MW. The beam was injected in co-direction

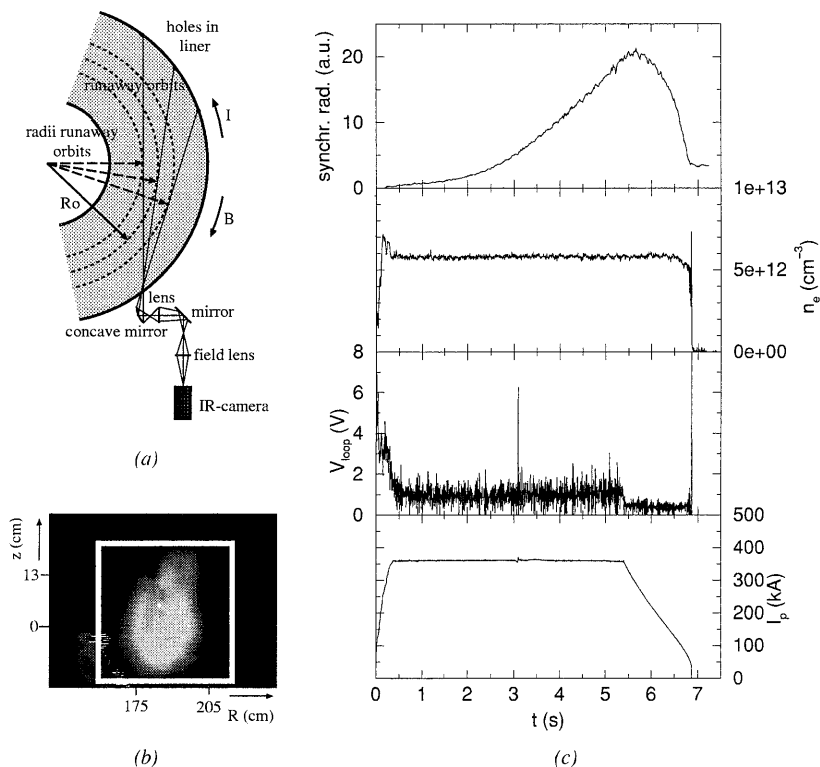


Figure 6.6: (a) Set-up for detection of runaways in TEXTOR-94. (b) Typical IR picture showing the synchrotron radiation in a poloidal projection. Indicated is a software defined integration box. Thermal background is subtracted. (c) Time evolution of synchrotron radiation, line averaged density, loop voltage and plasma current in an Ohmic discharge. In this plot of the synchrotron radiation signal, the thermal background is not subtracted.

with respect to the plasma current. ICRH was applied in a power range from 0.15 to 0.85 MW. There are a few discharges with both NBI and ICRH.

During application of NBI, \bar{n}_e rises. The increase in \bar{n}_e is depending on the injected power and is in the range 0% up to 190%. It takes up to 300 ms to reach the maximum density. For comparison, also discharges were made with a \bar{n}_e increase by means of a gas puff without any heating. The \bar{n}_e -increases in these gas puff experiments were in the range of 135% up to 340%.

In table 6.1, an overview is given of the discharges analyzed in the present paper. Indicated are density \bar{n}_e and loop voltage V_{loop} , both before and after the heating or gas puff, and the time at which the heating or gas puff starts, t_{heat} or t_{puff} , and the length of the heating or gas puff interval, Δt_{heat} or Δt_{puff} . Also, the energy confinement time determined from diamagnetic energy measurements, τ_E , is indicated for several discharges. Because of the low densities, the error in τ_E is relatively large, about 25%. During all runaway discharges, at the most two channels of the electron cyclotron emission (ECE) system were available. The central temperature in Ohmic runaway discharges can only be roughly estimated to be 1–2 keV. In several discharges with NBI heating, a density increase was programmed to avoid the beam shine through. An additional density increase during heating can be caused by the heating mechanism itself and its effect on the vessel wall. The radiation signals of a few typical discharges with increasing amounts of applied power either by NBI or ICRH listed in table 6.1 are shown in figure 6.7.

Ohmic part of discharge

All of the discharges listed in table 6.1 exhibit an approximately exponential rise in the radiation signal in the Ohmic part of the discharge. So, the secondary generation process is the dominant generation process in these series of experiments, i.e. $t_0 < \tau_r$. The effective rise time t_{eff} varies from 0.3 s to 0.8 s depending on the plasma parameters. The avalanche time is $t_0 = 0.42$ s according to eq. (6.3) with $\ln \Lambda = 16$, $E = 0.1$ V/m and $Z_{\text{eff}} = 2$. The avalanche time is of the same order as the measured t_{eff} . Because $t_{\text{eff}}^{-1} = t_0^{-1} - \tau_r^{-1}$, that implies that the runaway confinement time is large compared to t_0 . For example, when $\tau_r = 5$ s and $t_0 = 0.42$ s, it follows that $t_{\text{eff}} \approx 0.46$ s. In [8], it was indeed estimated $\tau_r > 3.5$ s in Ohmic discharges. Note that the avalanche time is, hence, well estimated by eq. (6.3).

#	NBI-co (MW)	ICRH (MW)	$\bar{n}_{e,b}$ (10^{19} m^{-3})	$\bar{n}_{e,a}$ (10^{19} m^{-3})	$V_{\text{loop},b}$ (V)	$V_{\text{loop},a}$ (V)	$t_{\text{heat or}}^{\text{puff}}$ (s)	$\Delta t_{\text{heat or}}^{\text{puff}}$ (s)	τ_E (ms)
61977	-	-	0.70	1.9	0.95	1.03	2.5	2	-
61980	-	-	0.70	1.9	1.00	1.00	2.5	2	-
61981	-	-	0.70	1.9	1.02	1.02	2.5	2	-
61985	-	-	0.70	2.5	1.12	1.03	2.5	2	-
61987	-	-	0.70	3.1	0.99	1.05	2.5	2	-
62790	-	-	0.51	1.2	0.86	1.08	2.5	2.5	24
64721*	0.09	-	0.63	0.63	1.13	1.10	3	2.5	-
64717*	0.14	-	0.63	0.63	1.12	1.08	3	2.5	-
67607	0.14	-	0.67	0.70	1.17	1.09	3	1.5	10
73207	0.16	-	0.60	0.78	1.07	0.99	3	1.5	-
73751	0.17(D)	-	0.63	0.78	1.03	1.03	3	1.5	16
67608	0.24	-	0.67	0.70	1.16	1.00	3	1.5	12
73209	0.32	-	0.59	1.0	1.06	0.92	3	1.5	18
62795	0.39	-	0.50	1.4	0.82	0.90	2.7	1.0	34
73210	0.39	-	0.59	1.1	1.06	0.89	3	1.5	21
73212	0.59	-	0.59	1.3	1.04	0.82	3	1.5	25
62791	0.60	-	0.50	1.3	0.81	0.90	2.7	1.0	31
55180†	1.3	-	0.59	1.7	1.06	0.47	2	1.5	-
67599	-	0.17	0.67	0.73	1.11	1.16	3	1.5	10
73764	-	0.26	0.61	0.70	1.04	1.03	3	1.5	-
67600	-	0.34	0.67	0.84	1.13	1.07	3	1.5	14
67601	-	0.51	0.67	0.90	1.10	1.13	3	1.5	16
73763	-	0.51	0.62	0.83	1.06	0.97	3	1.5	7
67602	-	0.68	0.67	1.0	1.10	1.13	3	1.5	16
67603	-	0.85	0.67	1.0	1.12	1.09	3	1.5	16
73752	0.17(D)	0.17	0.63	0.84	1.05	0.93	3	1.5	14
73753	0.17(D)	0.34	0.63	1.0	1.13	0.98	3	1.5	18

Table 6.1: Overview of the analyzed runaway discharges with gas puff and additional heating. Ohmic heating is $P_{\Omega} < 0.4$ MW. Indicated are \bar{n}_e and V_{loop} , both before (subscript 'b') and after (subscript 'a') the puff or heating. The V_{loop} is estimated after a typical current diffusion time of 300 ms. Also the time interval of puffing or heating is shown, as well as τ_E . Hydrogen was used for the neutral beam, except for the cases marked with a 'D' at which a deuterium beam was injected. The stars at the shot numbers denote those cases where $I_p = 450$ kA. In all other discharges, $I_p = 350$ kA. The dagger denotes a discharge in TEXTOR, where the the current flat top phase ended at 2.5 s (so only 0.5 s of the heating interval coincidences with this phase). The other discharges are done in TEXTOR-94 where the flat top phase ended at about 5 s.

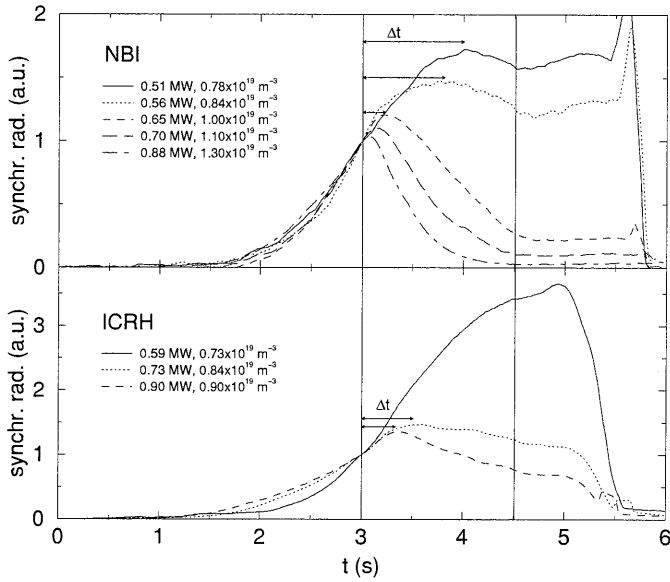


Figure 6.7: Measured radiation evolutions of runaway discharges at which from $t = 3$ s until $t = 4.5$ s heating is applied as indicated by the lines. The current flat top phase ends at about $t = 5$ s. The curves are normalized at their synchrotron radiation level at t_{heat} . Total input power P_{tot} and density \bar{n}_e during the heating interval are indicated. Also, $\Delta t \equiv t_{\text{max}} - t_{\text{heat}}$ is indicated.

Additionally heated part of discharge

In all discharges, it is observed that, directly after the auxiliary heating is switched on at $t = t_{\text{heat}}$, the radiation signal continues to rise. The more power is applied, the shorter the continuation of the rise is. After that initial rise, the signal either continues to rise, now with another effective rise time compared to the Ohmic part, or it decays (i.e. t_{eff} becomes negative). The decay is delayed by $\Delta t \equiv t_{\text{max}} - t_{\text{heat}}$, indicated in figure 6.7, where t_{max} is the time of maximum in the radiation signal. Figure 6.8 shows that Δt is rapidly decreasing with input power P_{tot} and density \bar{n}_e . The Ohmic heating power is $P_{\Omega} \lesssim 0.4$ MW for these discharges.

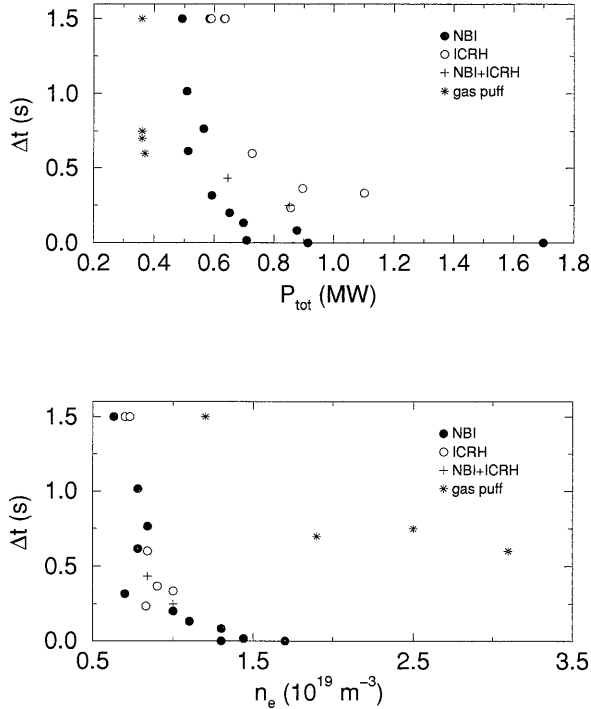


Figure 6.8: *The delay of the maxima in the radiation signals, $\Delta t \equiv t_{\text{max}} - t_{\text{heat}}$ both as function of total heating power and density.*

In figure 6.9, t_{eff}^{-1} (the inverse of the effective rise or delay time) is plotted as function of additional power P_{add} for all discharges listed in table 6.1. The figure shows that t_{eff}^{-1} decreases with increasing P_{add} . The results for the

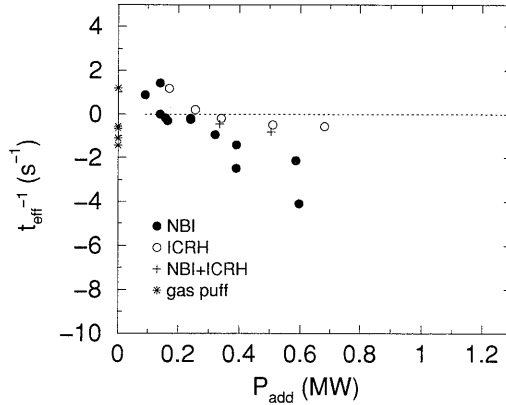


Figure 6.9: Inverse of the effective time t_{eff} as function of additional heating power. There is no density correction made in this plot. Positive effective times correspond to rising radiation signal during heating, negative times correspond to a decaying radiation signal.

ICRH discharges show a less strong dependence on P_{add} . However, in this plot no correction for the density increase is made. The increase in \bar{n}_e is typically larger in case of NBI than in case of ICRH. Figure 6.10 shows that the absolute value of the effective time of only the decaying signals, $|t_{\text{eff}}|$, is decreasing with increasing \bar{n}_e as well as increasing P_{tot} .

The parameters Δt and $|t_{\text{eff}}|$ are mainly introduced to characterize the measured signals. Later, the measured signals are compared to radiation signals calculated with a simulation code. This comparison is done on the basis of these characteristic parameters of measured and simulated radiation signals.

During additional heating, a decrease in electric field E is expected because of a decrease in resistivity due to a temperature increase or because of changes in bootstrap current and current drive effects.

We assume that the loop voltage V_{loop} is a measure of the electric field in the plasma center after a current diffusion time ~ 300 ms in TEXTOR-94. From table 6.1, it follows that the change in V_{loop} and, therefore, in E is mostly relatively small, about 20%. The discharge with 1.3 MW NBI power is an exception, with a 50% drop of the electric field. Three examples of time traces of V_{loop} are shown in figure 6.11. While in the Ohmic part of the discharge the sawtooth activity is low ($\Delta T_e/T_e < 10\%$), the amplitude and the repetition time of the sawteeth increase during NBI. In the discharge

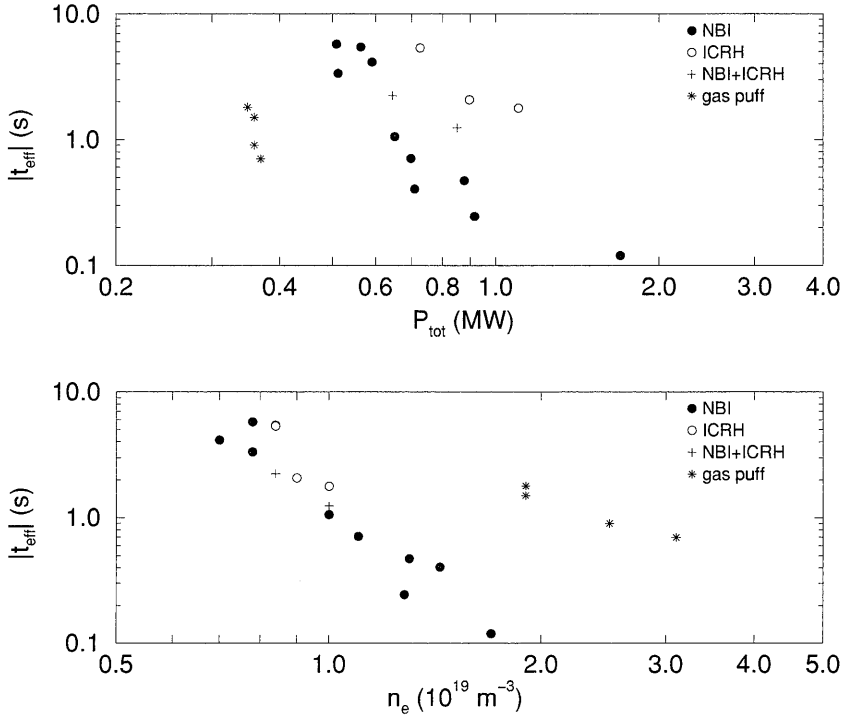


Figure 6.10: *The absolute value of the decay time, $|t_{\text{eff}}|$, of the decaying radiation signals as function of total power and line averaged density.*

with 0.6 MW heating, $\Delta T_e/T_e \approx 15\%$, the discharge with 1.3 MW shows $\Delta T_e/T_e \approx 40\%$.

Gas puff experiments

In the gas puff experiments (with no additional heating), the \bar{n}_e increases in the range 135% to 340%. When the density increase is only 135%, the radiation signal continues to rise during a time > 1.5 s and does not show a maximum. Larger gas puffs show a roll over in the radiation signals, after delay times Δt of > 0.6 s. Hence, the radiation signals depend on \bar{n}_e . From figure 6.10, it is derived $|t_{\text{eff}}| \propto \bar{n}_e^{-2}$.

When it is assumed that the effect of a density increase on $|t_{\text{eff}}|$ in these gas puff experiments is similar to the effect of the density increase during the heating interval, the \bar{n}_e -corrected dependence of $|t_{\text{eff}}|$ on P_{tot} is derived

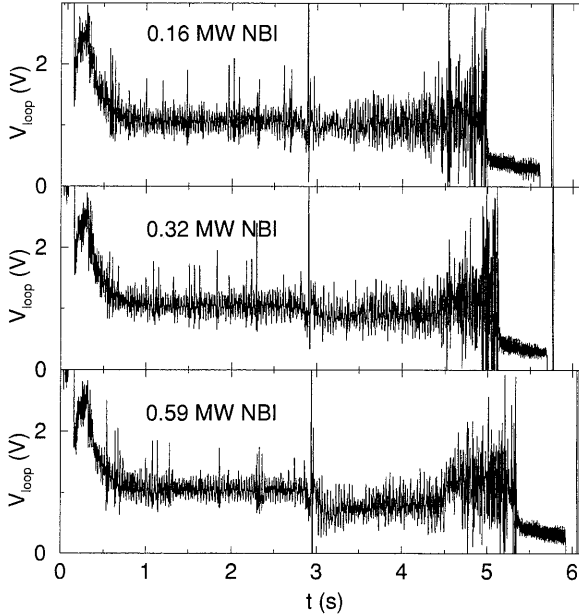


Figure 6.11: Loop voltage signals for three different discharges with neutral beam injection (73207, 73209 and 73212). The loop voltage decreases during the heating interval up to approximately 20%.

for the experiments with auxiliary heating. It is found that approximately $|t_{\text{eff}}| \propto \bar{n}_e^{-2} P_{\text{tot}}^{-2}$ for the NBI and ICRH experiments. The effect of P_{tot} with ICRH is somewhat smaller than with NBI. However, the ICRH data consists of only three data points, which gives a relative large uncertainty in the exact P_{tot} -dependence.

6.2.5 Simulations

All the observed radiation signals show a dominant secondary generation process in the Ohmic phase of the discharge. Therefore, a code has been developed that simulates the amount of measured radiation, including both the primary and secondary generation mechanism. The energy evolution of one runaway electron is calculated including the radiation limit as discussed in section 6.2.2. The power emitted by one runaway electron that is measured with the IR camera, P , is obtained from eq. (6.5) with wave length $\lambda \in$

$[3, 8] \mu\text{m}$. The total detected synchrotron radiation P_{det} at a time t_1 follows from the integration of all runaway density fractions at t_1 having some energy $\gamma(t_1)$ multiplied by corresponding runaway power $P(\gamma(t_1))$.

Ohmic discharge

Simulated evolutions of the synchrotron radiation for an Ohmic runaway discharge are shown in figure 6.12. Also, the energy distribution and the detected power distribution are shown. Experimentally, a pitch angle $\theta \approx 0.1$ is estimated for the high energetic runaways in TEXTOR-94, which can be explained by electron-ion collisions [10]. Therefore, a constant $\theta = 0.1$ is chosen in the simulations. The runaway confinement time τ_r is chosen constant $\tau_r = 5$ s, based on estimates in previous experiments [8, 10]. Other parameters are $E = 0.093$ V/m, $Z_{\text{eff}} = 2$, $\ln\Lambda = 16$, which are typical in TEXTOR-94.

A runaway electron in TEXTOR-94 reaches an energy of about 30 MeV (i.e. $\gamma \approx 60$) after approximately 1.5 s. Figure 6.12(a) shows that the simulated radiation signal is exponentially rising as long as $t_0 < \tau_r$, i.e. the secondary generation is the dominant generation mechanism. When $t_0 > \tau_r$, a steady state situation is reached as shown in figure 6.12(b). In this particular example, $\tau_r = 0.1$ s is chosen. Observations of a steady state radiation signal are scarce. An example is found in [8].

Figure 6.12 also shows the energy and detected power (wavelength range $\lambda \in [3, 8] \mu\text{m}$) distributions after 5 s. When secondary generation is the dominant generation process, the energy distribution is broad. Because of the exponential character of the population growth by secondary generation, no accumulation at the maximum reachable energy, $\gamma \approx 60$, occurs. When the runaway confinement time $\tau_r < t_0$ is small, the time available for acceleration is small as well and the energy spectrum remains narrow. The distributions of detected power show that most of the detected radiation is emitted by the highest energetic runaways.

Additionally heated discharge

Figure 6.9 shows that with increasing additional heating, the inverse of effective time decreases. Because $t_{\text{eff}}^{-1} = t_0^{-1} - \tau_r^{-1}$ where avalanche time $t_0 \sim 1/E$ is given by eq. (6.3), and runaway confinement τ_r is an unknown parameter, a decrease in t_{eff} suggests a decrease in confinement τ_r or a decrease in electric field E . Recall that the secondary generation mechanism is dominant in these series of experiments. Because this generation process is independent on electron density \bar{n}_e , a change in \bar{n}_e is not considered in the simulations.

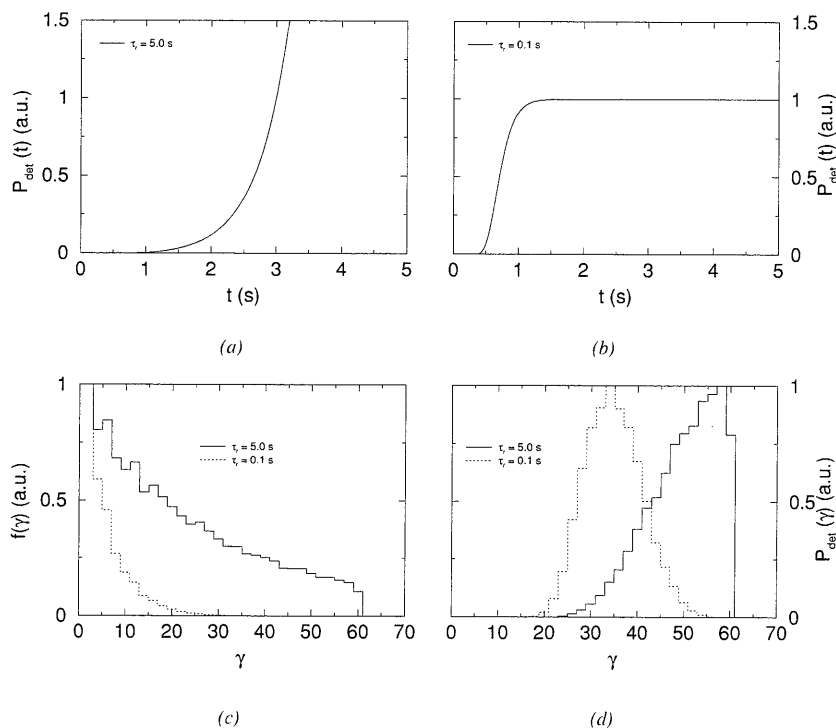


Figure 6.12: The evolutions of the simulated radiation in an Ohmic runaway discharge, including secondary generation. Avalanche time is $t_0 = 0.42$ s. (a) $\tau_r = 5$ s, so $t_0 < \tau_r$ and the signal rises exponentially. (b) $\tau_r = 0.1$ s, so $t_0 > \tau_r$ and the radiation signal reaches steady state. (c) Energy distributions after 5 s, both for $\tau_r > t_0$ and $\tau_r < t_0$. (d) Detected power distributions after 5 s, both for $\tau_r > t_0$ and $\tau_r < t_0$.

However, the radiation signals did show a response on a density increase (gas puff experiments). The physical mechanism behind that observation is not really understood. Because of the observed weak response of the signal at density increases of $\leq 135\%$ (no roll-over), we assume that the density increase effect may be neglected in the interpretation of the synchrotron radiation measurements during auxiliary heating, as long as we consider the discharges with an density increase $\leq 135\%$.

A change in Z_{eff} influences both the primary and secondary generation process. Simulations show, however, that the effect on the generation processes of an increase or decrease in Z_{eff} of more than 50% does not result in radiation signals that roll over. The effect of a change in Z_{eff} on the electric field is treated explicitly as a change in E .

Change in runaway confinement time During its acceleration, a runaway runs through the whole energy spectrum. A priori, it is unknown in what stage of the acceleration the electron experiences a bigger loss when heating or a gas puff is applied. Therefore, a runaway confinement that is a step function of energy parameter γ is implemented into the radiation code as shown in figure 6.13. The energy of the step, γ_{step} , can be varied over the whole runaway energy range in different simulations.

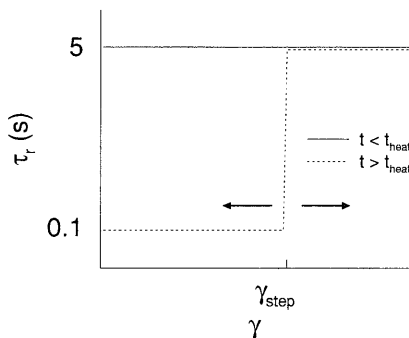


Figure 6.13: Before the heating starts, $t < t_{\text{heat}}$, runaways have all the same confinement time $\tau_r = 5$ s. When $t \geq t_{\text{heat}}$, confinement time becomes $\tau_r = 0.1$ s for runaways with energy $\gamma < \gamma_{\text{step}}$. For runaways with $\gamma \geq \gamma_{\text{step}}$, the confinement time remains $\tau_r = 5$ s. The step can vary in different simulations.

In figure 6.14(a), simulated radiation signals are shown, where at $t < t_{\text{heat}}$ the confinement time is constant $\tau_r = 5$ s and at $t \geq t_{\text{heat}}$

$$\begin{aligned} \gamma < \gamma_{\text{step}} : \tau_r &= 0.1 \text{ s} \\ \gamma \geq \gamma_{\text{step}} : \tau_r &= 5 \text{ s} \end{aligned}$$

The lower τ_r is chosen in such a way, that it is significantly smaller than the time needed to reach the equilibrium runaway energy (at the most 1.5 s). Examples are shown with $\gamma_{\text{step}} = 0, 20, 40, 50, 60$. ' Ω ' denotes the case $\gamma_{\text{step}} = 0$, as already shown in figure 6.12. When $\gamma_{\text{step}} = 60$, runaways of all energies have $\tau_r = 0.1$ s at $t \geq t_{\text{heat}}$ as no particles with $\gamma > \gamma_{\text{step}}$ exist.

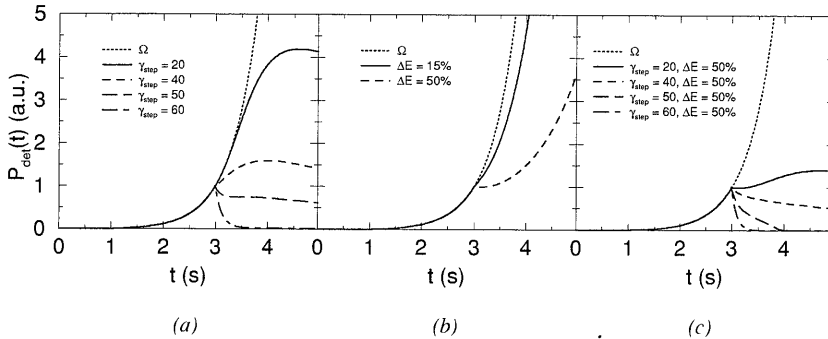


Figure 6.14: (a) Simulated radiation signals where at $t = 3$ s the confinement of runaways changes from 5 s to 0.1 s for runaways with $\gamma < \gamma_{\text{step}}$. Simulations with $\gamma_{\text{step}} = 0, 20, 40, 50, 60$ are shown. ' Ω ' denotes the case without any changes as shown in figure 6.12(a) (b) Simulated radiation signals, where at $t = 3$ s the electric field changes from 0.093 V/m either to 0.079 V/m or to 0.051 V/m. (c) Simulated radiation signals where at $t = 3$ s, both the electric field is decreased from 0.093 V/m to 0.051 V/m and τ_r changes from 5 s to 0.1 s for runaways with $\gamma < \gamma_{\text{step}}$ where $\gamma_{\text{step}} = 0, 20, 40, 50, 60$.

The simulated radiation signals corresponding to $\gamma_{\text{step}} = 20$ and $\gamma_{\text{step}} = 40$ show at $t \geq t_{\text{heat}}$ an initial continuation of the rising signal, after which the radiation eventually decays. When $\gamma_{\text{step}} = 50$ and 60, the simulated signal immediately shows a decay. The delay in decay Δt is smaller when γ_{step} is larger as can be recognized from figure 6.14(a). Because the largest contribution to the total detected radiation comes from the runaways with the highest energy according to eq. (6.5), a stronger loss of lower energetic runaways at $t \geq t_{\text{heat}}$ does not directly affect the radiation signal. The loss of the low energetic runaways becomes only apparent after the time needed to

accelerate them to higher energies of largest radiation contribution. When γ_{step} is chosen successively higher, also runaway electrons are lost that already contributed directly to the radiation signal.

In the simulations shown in figure 6.14(a), the confinement time τ_r for runaways with energy $\gamma \geq \gamma_{\text{step}}$ remained unchanged. Simulations where at $t \geq t_{\text{heat}}$ for runaways with $\gamma \geq \gamma_{\text{step}}$ a confinement time $\tau_r = 1$ s was taken instead of 5 s, were similar to the signals in figure 6.14(a).

Change of electric field In figure 6.14(b), a simulation is shown in which only a decrease in electric field is taken into account (runaway confinement time is chosen constant $\tau_r = 5$ s). The change in E is 15% and 50%, i.e. from $E = 0.093$ V/m to $E = 0.079$ V/m or to $E = 0.051$ V/m at $t \geq t_{\text{heat}}$. Note that in the experiments, the observed change in electric field is about 20% (see figure 6.11, although a lower E on axis is possible due to NBI current drive or due to the skin effect when a time scale $\Delta t < \tau_{\text{skin}}$ is considered), apart from the one discharge into which 1.3 MW NBI power is injected (change in E about 50%).

When the electric field decreases, the maximum reachable energy for one runaway electron is decreased and therefore also the emitted power per electron $P(\gamma(t))$. So, the radiation signal is expected to change immediately after the change which is clearly visible from figure 6.14(b). The effect of the decreased field on the primary generation (the birth rate λ_r is a strong exponential function of $\varepsilon(E)$) is hardly noticeable, as long as the secondary generation is dominant, i.e. as long as $t_0(E) < \tau_r$. Figure 6.14(b) shows that even a change of 50% in E is not sufficient to have $t_0(E) > \tau_r$ (when $\tau_r = 5$ s), which would lead to a negative t_{eff} , i.e. to a decaying radiation signal.

Simultaneous change in electric field and confinement time A simulation of radiation evolutions combining the effects of the changes in electric field E and in confinement time τ_r is shown in figure 6.14(c). In this particular simulation, $\tau_r = 5$ s and $E = 0.093$ V/m, when $t < t_{\text{heat}}$. At t_{heat} , τ_r changes from 5 s to 0.1 s for runaways with energy $\gamma < \gamma_{\text{step}}$ with $\gamma_{\text{step}} = 0, 20, 40, 50, 60$. E changes from 0.093 V/m to 0.051 V/m.

In figure 6.14(c), the initial dip in the radiation signal is a consequence of the change in equilibrium runaway energy because of the change in electric field E . When $\gamma_{\text{step}} = 20$, the signal rises again. After that rise, the strong loss of the lower energetic runaways due to the energy dependence of τ_r becomes apparent as a global maximum in the radiation signal. When $\gamma_{\text{step}} \geq 40$, the combination of the increased $t_0(E)$ and the energy dependent τ_r results in a signal that immediately decays at $t = t_{\text{heat}}$.

A large decrease in electric field in the simulations can not explain the continuation of the signal before the decay sets in. Moreover, the measured decrease in electric field E is about 20%, apart from one extreme case, so the effect of this change is expected to be small. It is therefore not surprising, that the observed features in the measured radiation signals are mainly recognized in the simulations where only the confinement time changed. Even when a change in E of 50% is considered in the simulations, corresponding to the case of 1.3 MW NBI injection, the shape of the radiation signal is primarily determined by a change in runaway confinement.

Summary In summary, the measured radiation signals of heated runaway discharges show a decrease, characterized by $|t_{\text{eff}}|$ after a time delay Δt with respect to the switching on of the heating, depending on the applied heating power. Simulations of radiation signals demonstrate that such a time delay appears when an energy dependent confinement time is implemented into the simulation code. Using a step function as the relation between confinement time τ_r and energy γ , we find that delay times of less than 0.1 s up to 1 s, which is approximately the time needed to accelerate an electron in the observable range of energy, correspond to a step at energies of about 100 keV, which is the critical runaway energy, up to 30 MeV.

Such an energy dependence in confinement time is to be expected from theory when transport is mainly determined by magnetic turbulence as is the case for runaway electrons. The shift of the electron drift orbit, which is proportional to energy, causes an averaging of the effect of magnetic turbulence on runaway transport which depends on the ratio between shift and average magnetic mode width. Runaway electrons with energies of 100 keV up to 30 MeV have drift orbit shift displacements of 0.02–6 cm. To refine the function $\tau_r(\gamma)$ and to relate the drift orbit shift to a scale size of magnetic turbulence, we apply the theory of transport reduction by Mynick and Strachan in the next section.

6.2.6 Relating the energy dependence of runaway confinement to the average width of perturbing magnetic modes

Drift orbit averaging

In [4], the enhancement of runaway electron confinement due to drifts and finite Larmor radius over the value ignoring these effects, $\tau_r/\tau_{r,0}$, is numerically calculated. In this calculation, it is assumed that electron transport is completely determined by magnetic perturbations.

This enhancement factor $\tau_r/\tau_{r,0}$ is given as function of ratio between runaway drift and averaged mode width, d_r/δ , and can be approximated by

$$\frac{\tau_r}{\tau_{r,0}} \approx \left(1 + 1.1 \frac{d_r}{\delta}\right)^{5.7} \quad (6.7)$$

in case of purely even-parity turbulence (see figure 2 in [4]). In [4], it was found that experimental values of confinement enhancement correspond best with this theoretical curve of even-parity turbulence. The enhancement of runaway electron confinement is calibrated with respect to the driftless case. In [4], this driftless runaway transport is equated to thermal electron transport scaled with the ratio between the runaway and thermal velocity, $\tau_{r,0} = \tau_E v_{th}/v_r$ with v_r the runaway velocity. To estimate the runaway confinement time τ_r , it is, therefore, necessary to know the thermal confinement τ_E .

In the region of the detected runaway population, the average q value is taken to be 1.5 and $B = 2.2$ T, so according to eq. (6.6), $d_r = 1.2 \times 10^{-3} \gamma$ m. The relation between runaway confinement time and energy is, therefore,

$$\tau_r(\gamma, \delta) = \frac{\tau_E v_{th}}{v_r} \left(1 + \frac{1.3 \times 10^{-3} \gamma}{\delta}\right)^{5.7} \text{ s} \quad (6.8)$$

where δ is the average mode width of the turbulence.

Table 6.1 shows that for the low density runaway discharges, $\tau_E = 10 - 30$ ms. The thermal electron velocity is typically $v_{th} \approx 1 \times 10^7$ ms⁻¹ (corresponding to an electron temperature $T_e \approx 1$ keV). In figure 6.15(a) and 6.16(a), the runaway confinement time τ_r according to eq. (6.8) is shown as function of energy parameter γ for different values of mode width δ . In these calculations, $\tau_E = 20$ ms is taken.

Simulations based on drift orbit averaging theory

The energy dependent confinement time described by eq. (6.8) has been implemented into the simulation code. A comparison between simulated and measured radiation signals, based on the typical parameters Δt and $|t_{eff}|$, allows the estimation of the average mode width δ .

(i) *Ohmic runaway discharges.* Figure 6.15(b) shows simulated radiation signals in an Ohmic discharge. The runaway confinement time used in these simulations is shown in figure 6.15(a). An exponential rising signal, as observed in radiation measurements in Ohmic runaway discharges, is obtained for $\delta < 0.5$ cm. For a larger δ , the corresponding confinement time becomes

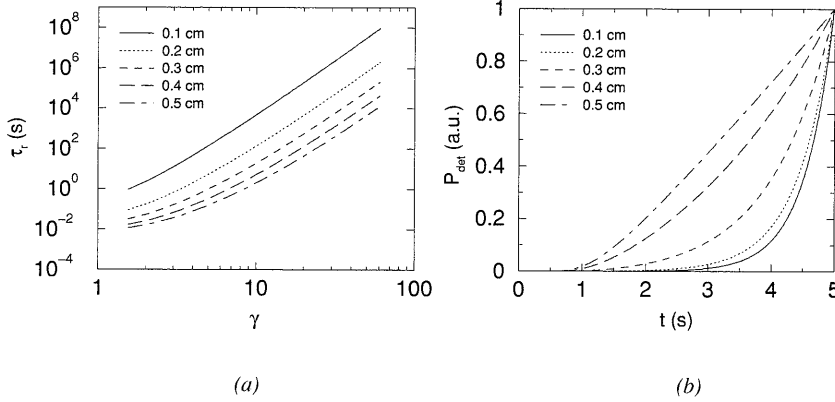


Figure 6.15: (a) Runaway confinement times τ_r are shown for different values of averaged mode widths δ and with thermal confinement $\tau_E = 20$ ms. (b) Simulated radiation signals based on runaway confinement time for different mode widths δ .

small with respect to the avalanche time t_0 . Then, the secondary generation process is no longer the dominant generation mechanism.

(ii) *Additionally heated runaway discharges.* In the simulation of radiation signals in figure 6.16(b), a value of $\delta = 0.2$ cm is taken in the Ohmic part ($t < 3$ s). The heating phase ($t \geq 3$ s) is simulated by taking a larger average mode width, in the range $\delta = 0.5 - 5$ cm. The confinement time corresponding to those mode widths is shown in figure 6.16(a). The radiation signals show a decay after some time delay that depends on the size of the input average mode width δ . A systematic study of a stepwise increasing mode width yields the relation between delay Δt and mode width δ as well as the relation between $|t_{\text{eff}}|$ and δ , shown in figure 6.17 for $\tau_E = 20$ ms.

(iii) *Runaway discharges with gas puff.* The radiation signal during a gas puff shows similar features as the radiation signal during additional heating. Following the previous line of argumentation, it should be concluded that also a large increase of density leads to a loss in lower energetic runaways, which was interpreted as an increase in average mode width of magnetic turbulence.

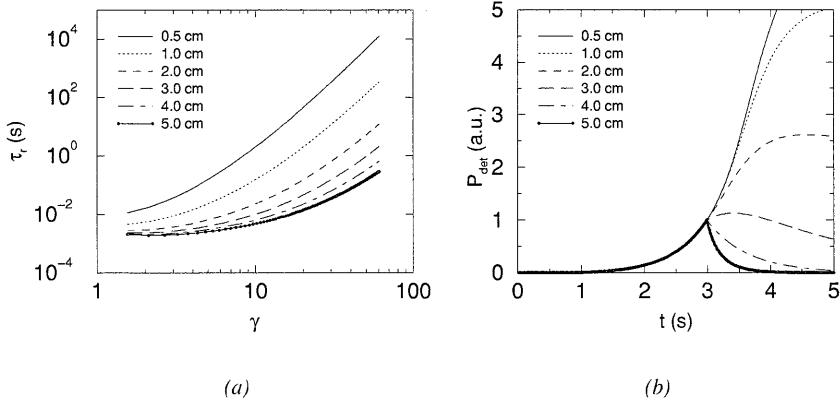


Figure 6.16: (a) Same as figure 6.15(a) but now the confinement time is calculated for larger values of averaged mode widths, $\delta = 0.5 - 5$ cm. (b) Simulated radiation signals where at $t = 3$ s the averaged mode width δ is changed. Before $t = 3$ s, $\delta = 0.2$ cm, after $t = 3$ s, $\delta = 0.5 - 5$ cm. $\tau_E = 20$ ms.

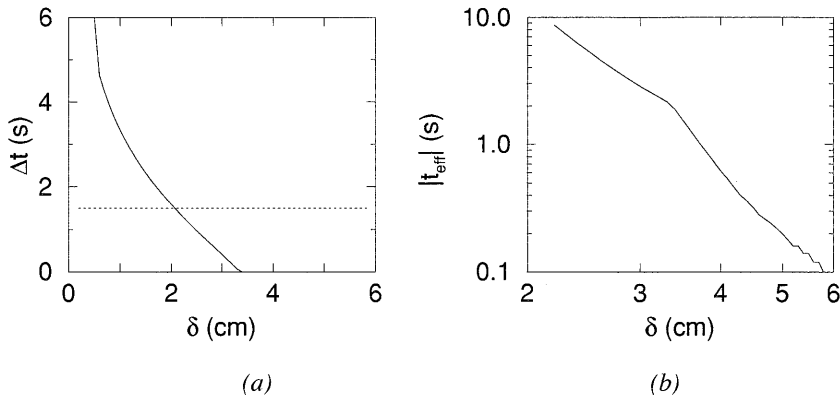


Figure 6.17: (a) Delay in decay Δt and (b) effective time $|t_{\text{eff}}|$ as function of mode width δ . $\tau_E = 20$ ms. The horizontal line in (a) corresponds with the maximum of the heating interval in the experiments.

Relation between mode width and heating power

From the simulations and the experimental data, we determined an average mode width of the magnetic turbulence for Ohmic low density plasmas and for low density plasmas with auxiliary heating. Figure 6.17 shows that Δt and $|t_{\text{eff}}|$ are decreasing with increasing average mode width δ according to our model. Figure 6.8 shows the measured relation between Δt and the additional heating power P_{add} . A comparison of simulated with measured signals on basis of the characteristic parameters Δt and $|t_{\text{eff}}|$ yields the relation between additional heating power P_{add} and average mode width δ . Figure 6.18 shows a few examples of measured radiation signals and of the corresponding simulated radiation signals. Figure 6.19 shows that δ increases with increas-

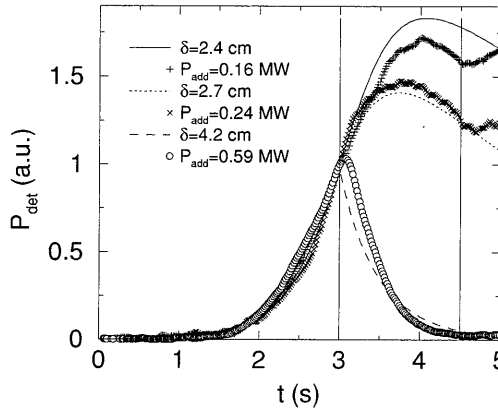


Figure 6.18: *Examples of comparison between measured signals (symbols) and the corresponding simulated signals (lines). The measured signals are from the NBI experiments, and also shown in figure 6.7. The vertical lines indicated the heating interval.*

ing P_{add} or P_{tot} . Here, only those discharges are considered with a maximum increase in density of 120%, which corresponds to a maximum additional heating power of 0.6 MW. We recall that an increase of 135% in the gas puff experiments resulted in a radiation signal that kept on rising after the density increase for more than 1.5 s. Therefore, it is assumed that the observed effects in the heating experiments are mainly caused by the applied heating power and not by the simultaneous density increase.

In summary, we now can directly relate the additional heating power to an average mode width from figure 6.19. As before, in an Ohmic plasma $\delta <$

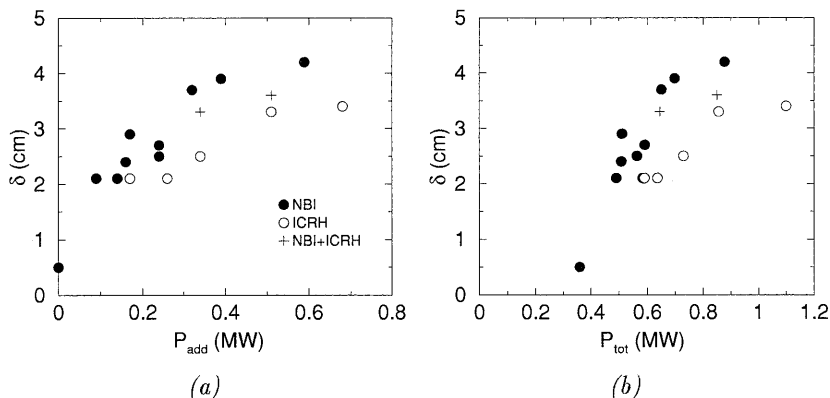


Figure 6.19: Relation between averaged mode width δ and (a) additional heating power P_{add} and (b) total input power P_{tot} derived from a comparison between simulated and measured radiation signals.

0.5 cm. For 0.6 MW NBI heating, $\delta = 4.2$ cm. A small amount of additional heating power already enlarges the averaged mode width considerably.

6.2.7 Discussion

We have interpreted the delay in the synchrotron radiation signals after switching on auxiliary heating as a larger loss of lower energetic runaways. The physical mechanism that can explain the energy dependence of runaway confinement time is the drift orbit averaging that reduces the effect of magnetic turbulence on runaway transport. This interpretation implies that runaway transport is mainly determined by magnetic turbulence, which is expected to be the case.

Using the model given in [4], we found a relation between the delay in the radiation signals and the scale size of the magnetic perturbing modes. During the heating interval of the discharges that were compared with the simulations, the density increased up to 120% and the heating power was in the range from 0.14 MW to 0.59 MW. Gas puff experiments showed that a large density increase ($> 170\%$) influences the synchrotron radiation, but that an increase of 135% does not show a significant effect. Therefore, we related the average mode width to the heating power as shown in figure 6.19.

The absolute values of δ depend on the calibration of the confinement enhancement curve in eq. (6.8). This calibration is rather uncertain. However, since the enhancement curve is very steep, the absolute calibration is not a

very sensitive parameter. In the simulations, we took as calibration factor a global energy confinement time of 20 ms, assuming that the electron heat diffusivity, χ_e , is dominated by magnetic turbulence ($\tau_E = 20$ ms corresponds roughly with $\chi_e \approx a^2/4\tau_E \sim 1 \text{ m}^2\text{s}^{-1}$, which is measured in TEXTOR-94). This assumption is questionable. When the contribution of magnetic turbulence to thermal transport is one order of magnitude lower, δ is a factor 2 smaller.

From table 6.1, it is seen that the energy confinement time increases with increasing heating power. According to the common scaling laws, it is expected that τ_E decreases with increasing heating power. Apparently, in experiments with low auxiliary heating power into low density discharges, τ_E is stronger affected by the density increase than by P_{tot} . On the other hand, we found that δ increases with heating power. When magnetic turbulence would be the only possible loss mechanism, this leads to the inconsistency that τ_E increases with increasing δ . When heat transport is dominated by other turbulent transport mechanisms, an increase in magnetic mode width does not exclude a simultaneous increase in energy confinement time.

Comparison with other experiments

The derived δ are quite similar to measured values in JET. Correlation reflectometer measurements [18] showed the existence of fine-scale density structures. Under Ohmic conditions, the radial extent of these structures was less than 0.5 cm. Under L-mode conditions, the radial extent of the density structures depends on the beam power and for 15 MW of NBI power the radial extent typically was equal or larger than 3 cm.

Interpreting δ as the width of chains of islands, the magnetic turbulence level, \tilde{B}_r/B , can be estimated. The width w of a magnetic island is related to the radial component of the fluctuating field \tilde{B}_r (see e.g. [19])

$$\tilde{B}_r = \frac{mq'B_p w^2}{16rq} \quad (6.9)$$

where m is the poloidal mode number, $q = m/n$, $q' = dq/dr$ the shear of the magnetic field and B_p is the poloidal field. For a runaway electron to be lost due to magnetic turbulence, the plasma must be filled with chains of islands. A region of good surfaces would act as a transport barrier [20]. Poloidal mode numbers of approximately 10 are assumed. For q , a parabolic profile can be taken with $q_0 = 0.8$ and $q_a = 3.8$. At $r = 15$ cm, $B_p \approx 0.1$ T. In an Ohmic runaway plasma with $\delta \equiv w < 0.5$ cm, it is found $\tilde{B}_r/B \sim 2 \times 10^{-5}$. For a heated discharge (0.6 MW NBI) with $\delta \equiv w \approx 4.2$ cm, $\tilde{B}_r/B \sim 1 \times 10^{-3}$. Note that when δ is a factor 2 smaller, the turbulence level is $\tilde{B}_r/B \sim 3 \times 10^{-4}$.

A previous estimate of \tilde{B}_r/B in TEXTOR-94 from runaway measurements [8] was in the order of 10^{-6} . That estimate was made, however, without taking into account the transport reducing effect of the drift orbit shift. The present estimate includes the drift orbit averaging and compares well with the estimate from cross polarization scattering measurements in Tore Supra [21,22].

Differences between NBI and ICRH

The measurements show that the runaway confinement during ICRH is less deteriorated than during NBI. This difference can have several causes. First, the applied heating power with ICRH couples not so well in the low density runaway discharges and it is unclear exactly how much of the power is deposited in the plasma center where the runaways are confined. Also, neutral beam injection increases the plasma rotation. What the effect of rotation is on confinement of runaway electrons is not clear.

6.2.8 Summary and conclusion

In this paper, measurements of synchrotron radiation, emitted by relativistic runaways, during additional heating are presented. A power scan with NBI and ICRH heating is made. The radiation signal in an Ohmic runaway discharge rises exponentially due to the dominant secondary generation mechanism. The application of additional heating leads to eventually decaying radiation signals. The decay in the radiation signal is observed after a time Δt measured from the start of heating. This delay Δt decreases with increasing applied heating power.

The shape of the observed radiation signals is qualitatively reproduced by simulations where at the time that the heating starts a sudden loss of low energetic runaways is introduced. The main contribution of the observed radiation originates from the highest energetic runaway electrons. Therefore, a loss of low energetic runaways becomes apparent only after a time that a low energetic runaway electron needs to reach an energy where it contributes significantly to the total radiation.

The physical mechanism that provides an energy dependent confinement of runaway electrons is the averaging of magnetic turbulence due to the drift orbit shift [4,5]. Here, it is assumed that runaway transport is mainly determined by magnetic field perturbations. When the drift orbit shift that is increasing with electron energy, is larger than the average mode width of the perturbations, the runaway transport due to these perturbations is strongly reduced.

Simulations of radiation signals are done where the runaway confinement time is based on the numerical calculation of the drift averaging effect presented in [4]. A comparison between these simulated radiation signals with measured radiation signals allows a relation between the additional heating power and an average mode width of the magnetic turbulence. In this interpretation, it is assumed that the contribution of the simultaneous density increase during heating to the roll-over of the synchrotron radiation is small. In an Ohmic plasma, it is estimated that the mode width is less than 0.5 cm. An additional heating power of 0.6 MW can enhance the average mode width up to several cm.

In conclusion, the observed synchrotron radiation signals during additional heating are explained by a degradation of runaway confinement time. The runaway confinement time is energy dependent due to the averaging effect of the electron drift orbit shift. Because of the additional heating, the average mode width of magnetic perturbations increases. This makes the drift averaging effect less effective for runaways with the smaller drift orbit shifts. Hence, the applied power causes larger runaway losses in the lower part of the total energy spectrum of the electrons. Relating the averaged mode width needed to explain the shape of the observed radiation signals to a magnetic island width, an estimate of \tilde{B}_r/B is deduced. In Ohmic plasmas, $\tilde{B}_r/B \sim 2 \times 10^{-5}$; in additionally heated plasmas, $\tilde{B}_r/B \sim 1 \times 10^{-3}$ at 0.6 MW neutral beam injection.

Acknowledgments

The authors would like to thank R. Uhlemann and F. Durodié for providing the measurements of NBI and ICRH power, respectively. This work was done under the Euratom-KFA and Euratom-FOM association agreements with financial support from NWO and Euratom.

References

- [1] Rosenbluth M N, Putvinski S V 1997 *Nucl. Fusion* **37** 1335
- [2] Yoshino R, Kondoh T, Neyatani Y, Itmai K, Kawano Y and Isei N 1997 *Plasma Phys. and Contr. Fusion* **39** 313
- [3] Gill R D 1993 *Nucl. Fusion* **33** 1613
- [4] Mynick H E and Strachan J D 1981 *Phys. Fluids* **24** 695
- [5] Myra J R and Catto P J 1992 *Phys. Fluids* **B4** 176

- [6] Kwon O J, Diamond P H, Wagner F, Fussmann G, ASDEX and NI teams 1988 *Nucl. Fusion* **28** 1931
- [7] Entrop I, Jaspers R, Lopes Cardozo N J, Finken K H 1999 *Plasma Phys. and Contr. Fusion* **41** 377
- [8] Entrop I, Lopes Cardozo N J, Jaspers R, Finken K H *Plasma Phys. and Contr. Fusion* **40** (1998) 1513
- [9] Rechester A B and Rosenbluth M N 1978 *Phys. Rev. Lett.* **40** 38
- [10] Jaspers R 1995 *Relativistic Runaway Electrons in Tokamak Plasmas*, PhD Thesis, Eindhoven University of Technology, The Netherlands
- [11] Entrop I, Jaspers R, Finken K H, Lopes Cardozo N J 1997 *Proc. 24th EPS on Contr. Fusion and Plasma Phys.* (Berchtesgaden) Part IV 1705
- [12] Jaspers R, Finken K H, Mank G, Hoenen F, Lopes Cardozo N J and Schüller F C 1993 *Nucl. Fusion* **33** 1775
- [13] Pankratov I M, Besedin N T 1996 *Proc. of the 23rd EPS Conf. on Contr. Fusion and Plasma Physics* (Kiev) Part I 279
- [14] Schwinger J 1949 *Phys. Rev.* **75** 1912
- [15] Finken K H, Watkins J G, Rusbüldt D, Corbett W J, Dippel K H, Goebel D M, Moyer R A 1990 *Nucl. Fusion* **30** 859
- [16] Laurent L, Rax J M 1990 *Europhys. Lett.* **11** 219
- [17] de Rover M, Lopes Cardozo N J, Montvai A 1996 *Phys. Plasmas* **3** 4478
- [18] Costley A E, Cripwell P, Fukuda T 1994 *Proc. of the 21st EPS Conf. of Contr. Fusion and Plasma Physics* (Innsbruck) Part I 199
- [19] Wesson J 1987 *Tokamaks* Oxford University Press
- [20] Hegna C C, Callen J D 1993 *Phys. Fluids* **B4** 1804
- [21] Zou X L, Colas L, Paume M, Chareau J M, Laurent L, Devynck P, Grésillon D 1995 *Phys. Rev. Lett.* **75** 1090
- [22] Colas L, Zou X L, Paume M, Chareau J M, Guiziou L, Hoang G T, Michelot Y, Grésillon D 1998 *Nucl. Fus.* **38** 903

Chapter 7

Runaway snakes

This chapter presents observations of runaway electrons in a perturbed magnetic topology. Due to injection of pellets or due to a shift of the plasma column, the magnetic field surfaces break up and magnetic islands are formed. The drift orbit surfaces of runaway electrons also break up and show a similar island structure. A narrow beam of runaway electrons confined inside an island is called a 'runaway snake'. This chapter investigates the transport properties of runaway electrons inside and outside islands. It is a reproduction of the paper 'Runaway snakes in TEXTOR-94' by I.Entrop, R.Jaspers, N.J.Lopes Cardozo, K.H. Finken, published in *Plasma Physics and Controlled Fusion* **41** 1999, 337, reproduced with kind permission of the journal editor.

Runaway Snakes in TEXTOR-94

I. Entrop^{1,2}, R. Jaspers¹, N.J. Lopes Cardozo¹
K.H. Finken²

Partners in the Trilateral Euregio Cluster:

¹FOM Instituut voor Plasmafysica 'Rijnhuizen', Association
Euratom-FOM, PO Box 1207, 3430 BE Nieuwegein, Netherlands

²Institut für Plasmaphysik, Association Euratom-KFA, Forschungszentrum
Jülich GmbH, 52425 Jülich, Germany

Abstract

Observations of a runaway beam confined in an island-like structure, a so-called runaway snake, are reported. The observations are made in TEXTOR-94 by measurement of synchrotron radiation emitted by these runaways. A full poloidal view allows the study of the synchrotron pattern of the snake to estimate runaway energy, pitch angle and the radius, shift and safety factor of the drift surface q_D at which the runaway beam has developed. The runaway snake parameters are investigated under different current and magnetic field strength conditions. Examples are found of a runaway snake at the $q_D = 1$ and the $q_D = 2$ drift surface. The radial diffusion coefficient of runaways inside a snake is $D_r \approx 0.01 \text{ m}^2\text{s}^{-1}$. The rapid runaway losses in regions of (macroscopic) magnetic perturbations outside a snake and the good confinement inside an island assumed to consist of perfect nested surfaces are consistent with magnetic turbulence as the main cause for runaway transport.

7.1 Introduction

The phenomenon of electron runaway [1] in tokamak plasmas is a consequence of the fact that the mean free path of electrons in a plasma is a strongly increasing function of their velocity. Electrons with a velocity larger than that for which the electric force - due to the electric field that drives the plasma current - balances the drag force due to collisions, are effectively accelerated and reach energies of the order of MeV. Runaway electrons are investigated for several reasons. For future fusion reactors, it is of major interest to know the processes of runaway generation after disruptions, because the highly energetic electrons could cause severe damage to the reactor [2-5]. Secondly, runaway transport is believed to be dominated by perturbations of the magnetic field. In that way, runaways could provide a tool to study magnetic structures in the plasma. The diffusion of runaways can be utilized

to probe the magnetic turbulence that is suggested to be one of the causes of the anomalous heat transport in tokamak plasmas [6–10]. Macroscopic MHD modes will also largely effect the runaway confinement [7]. The presence of magnetic islands gives rise to drift islands. The drift islands can be visualized by the synchrotron radiation emitted by energetic runaway electrons [11]. In this paper, we will concentrate on experimental investigations of the latter phenomenon in TEXTOR-94.

During a typical runaway discharge in TEXTOR-94, synchrotron radiation emitted by the runaways is observed. This radiation is emitted in a narrow cone into forward direction due to the relativistic motion of the runaways (energy $W_r \approx 25$ MeV) and is measured with an infrared (IR) detector [11–13]. Using this method of runaway detection, earlier experiments [11] have shown that after injection of a pellet in an Ohmic runaway discharge a large fraction of the runaway population is lost. This rapid loss is attributed to temporary stochastization of the magnetic field. A small fraction, however, survives the pellet injection and remains as a narrow runaway beam, confined in an island structure that still exists after the stochastization. The toroidal rotation frequency of the runaways is much higher than the rotation frequency of the island structure, so that the runaways effectively form a solid toroidal tube. Because of a clear relation with the 'density snake' observed in JET [14, 15] (a $m = 1$, $n = 1$ tube of high density which can occur if a pellet penetrates to the $q = 1$ surface) this phenomenon was called a 'runaway snake'.

Since those first observations of runaway snakes, more observations have been made and studied in a systematic manner. First, the IR detection system in TEXTOR-94 has been improved. Whereas in the previous set-up only part of the poloidal cross section was imaged on the detector, now a full view is obtained. This full view allows a more accurate study of runaway parameters such as radius and shift of drift orbit surface at which the runaway snake develops. Secondly, from the previous runaway snake observations, it is known that the runaway snake phenomenon is related to magnetic topology in the plasma and, hence, to the q profile. A study of the runaway snakes is made by investigating the effect of changes in the q profile through changes in plasma current and magnetic field.

The present experiments allow to study several aspects of the runaway drift orbit topology. Classically, the drift orbit surfaces are shifted from the corresponding magnetic field line surfaces [16]. A relativistic Hamiltonian description of drift orbit topology [17] including higher order energy terms, predicts that shift and radius of drift surfaces are different from the 'classical' approximation. In this paper, it is tried to answer the question, whether the drift surface parameters that are measured under different conditions

correspond with theory.

From the plasma physical point of view, the study of runaway confinement in a snake could give insight in the heat transport mechanisms in tokamak plasmas, because runaways act like test particles not bound to the ion cloud by ambipolar fields. Runaway snakes are especially interesting for this purpose because of their localized nature. Another question that is to be answered, is what can be learned about transport mechanisms in tokamak plasmas from the confinement properties of the runaways inside a snake.

The study of topology requires an accurate calibration and a careful consideration of the position of synchrotron signal and the position of runaway beam that gave rise to that signal. This is discussed in detail in section 7.2. In section 7.3, a previous snake observation [11] is summarized and the new observations, divided into three categories: runaway snake at full poloidal view, during different current values and after a plasma shift at higher magnetic field, are presented by giving an example of each category. In section 7.4, the interesting runaway parameters derived from the measurements are presented: the safety factor q_D , the radius r_{beam} and shift δ with respect to the magnetic axis of the drift surface at which the snake has developed; energy W_r and pitch angle $\theta = v_{\perp}/v_{\parallel}$, i.e. the ratio between the perpendicular and parallel velocity component of the runaways; rotation frequency of the mode structure and confinement properties of the runaways in- and outside the snake. These parameters are discussed in section 7.5, giving answers to the main questions as stated above. A summary and conclusion are given in the last section.

7.2 Runaway detection

7.2.1 Experimental set-up

In TEXTOR-94 (major radius $R_0 = 1.75$ m, minor radius $a = 0.46$ m), runaways are detected by measuring the synchrotron radiation with an Inframetrics thermographic camera. The camera is positioned to view tangentially into the plasma towards electron approach as shown in fig. 7.1(a). It uses a single HgCdTe detector and two scanning mirrors, one in horizontal and one in vertical direction. One image is scanned in $1/60$ s from top to bottom, in NTSC-TV standard. The radiation is detected in a wavelength range of $3 - 8 \mu\text{m}$. Typical conditions for Ohmic runaway discharges in TEXTOR-94 are a line averaged density $\bar{n}_e < 1 \times 10^{19} \text{ m}^{-3}$, a loop voltage $V_{\text{loop}} \approx 1$ V, a toroidal magnetic field $B_t = 2.2$ T, and a plasma current $I_p = 250 - 350$ kA. Fig. 7.1(c) shows a typical IR picture of a runaway

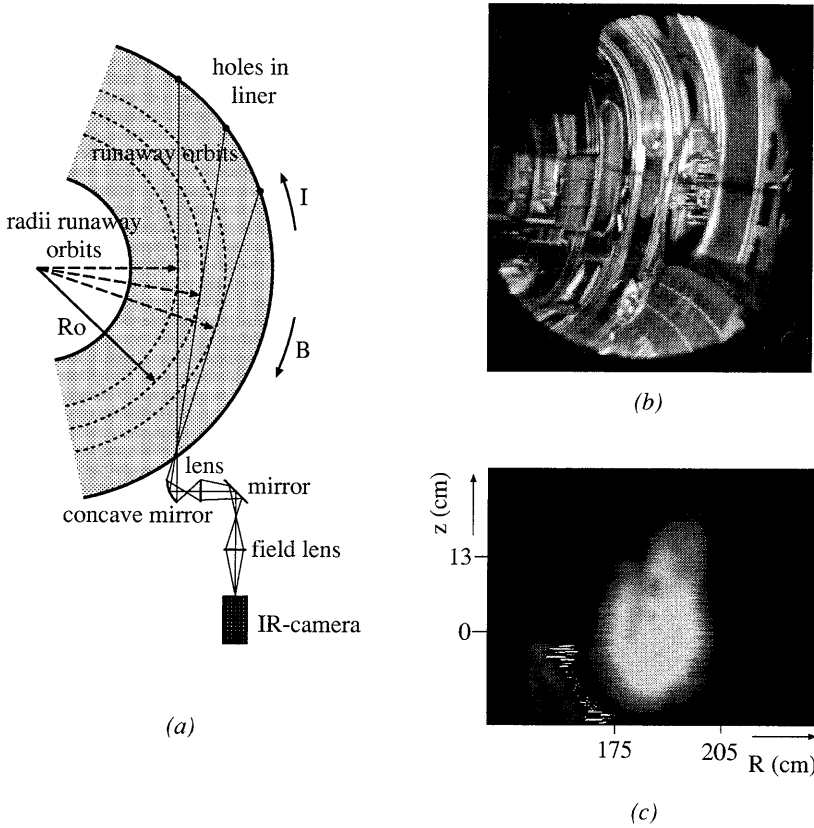


Figure 7.1: (a) Schematic setup of runaway detection system with construction of horizontal runaway position (top view); (b) view from the position of IR camera taken with a visible light camera, in the upper left corner the view is partly cut off by a part of the neutral beam injection system; (c) typical example of an IR picture taken during a runaway discharge in an unperturbed plasma (thermal background is subtracted).

discharge in an unperturbed plasma with subtraction of the thermal background. During the experiments, the IR pictures are recorded on video tape and are processed afterwards.

The optical system used to image the synchrotron radiation on the detector gives rise to deformations of the IR pictures. Fig. 7.1(b) shows this effect with a photograph taken from the IR camera position. A calibration from picture pixel to poloidal position is made as shown in fig. 7.1(a): pixels that correspond with objects in the thermal background (e.g. liner windows, belt limiter), are related with a major radius R by constructing circles in the equatorial plane tangent to the lines connecting these objects and the first mirror. The plot of R against corresponding pixel number is fitted with a continuous curve. Interpolation gives R for every pixel. The intensity is corrected for the transformation from pixel to position in toroidal geometry. Position in vertical direction z is constructed in an analogous way. After calibration, IR pictures are obtained that show the synchrotron radiation signal in a 2D poloidal plane spanned by R and z .

7.2.2 Synchrotron radiation pattern

Scanning a rotating object

The derivation of runaway parameters from the calibrated synchrotron pattern requires an investigation of the effects that influence the pattern. First of all, the scanning nature of the used IR camera implies simultaneous knowledge about time and position. When a rotating object in a 2D plane perpendicular to the line of sight of the camera (e.g. the projection of a toroidal rotating drift island (solid tube of runaways) on the poloidal cross section) is detected, it is possible to derive a rotation frequency f_{rot} of the object (drift island) by determining the time derivative of the rotated angle α .

Other effects are the multiple detection of one rotating object when $f_{\text{rot}} > f_{\text{pict}}$, where f_{pict} denotes the number of IR pictures per second scanned by the camera. Also, there is an elongation of the object image in case the vertical scan velocity, defined as number of lines per second multiplied by the vertical extent of one line in toroidal geometry, is in same direction as the vertical velocity component of the rotating object. This last feature gives the possibility of a unique determination of rotational direction in the poloidal projection.

Effects of the runaway orbit geometry on the synchrotron radiation pattern

More interesting are the effects on the shape of synchrotron pattern of physical nature. In first order approximation, runaways follow the magnetic field lines. Locally, field lines make a smaller angle with the equatorial plane at the high field side (HFS) than at the low field side (LFS). For the conditions used in this paper, the field lines at the HFS point upwards. The particle guiding center trajectories have a similar topology.

Runaways emit their synchrotron radiation in a small cone with vertex angle $2/\gamma$, where γ is the relativistic factor and a measure of energy. For the high energetic runaways in TEXTOR-94, the vertex angle is very small ($\sim 2^\circ$). Hence, runaways emit their radiation practically along their velocity vector. The gyrating velocity vector forms a cone with vertex angle 2θ , where $\theta = v_\perp/v_\parallel$ is the pitch angle. The effect of only the pitch angle on the shape of synchrotron spot was already studied in [13]. The horizontal extent of the synchrotron pattern was found to become broader at the HFS than the diameter of the original runaway beam by $R(1 - \cos \theta)$ where R is the major radius of the runaway orbits forming the beam.

Synchrotron radiation pattern simulations

A computer code was written to calculate the runaway positions in toroidal geometry of which the emitted synchrotron radiation is detected by the IR camera, taking into account the effect of pitch angle θ and the pitch of the helical guiding center orbits. The resulting synchrotron pattern was also calculated. Fig. 7.2 shows a few examples of calculated synchrotron patterns coming from a set of nested runaway drift surfaces with radius $r_{\max} = 15$ cm and pitch angle $\theta = 0$ and $\theta = 0.08$. Because a runaway snake is a closed tube, rotating along the torus, the synchrotron spots originating from the snake appear in a 2D poloidal projection as the pattern coming from a shell $r \in [r_{\min}, r_{\max}]$ of runaways. In fig. 7.2, also a pattern coming from a runaway shell $r_{\min} = 10$ cm $\leq r \leq r_{\max} = 15$ cm with $\theta = 0.08$ is shown.

In [18], the calculation of the pattern was treated analytically. Approximate expressions were found that give, under certain assumptions on position of detector and runaway beam size compared to toroidal geometry, the runaway positions for which synchrotron radiation falls into the detector. In the cases in which the analytical expressions can be used, the results of the numerical calculation were in agreement with the analytical ones.

All calculated patterns in fig. 7.2 show an inclination with respect to the equator, which is a consequence of the helical structure of the runaway

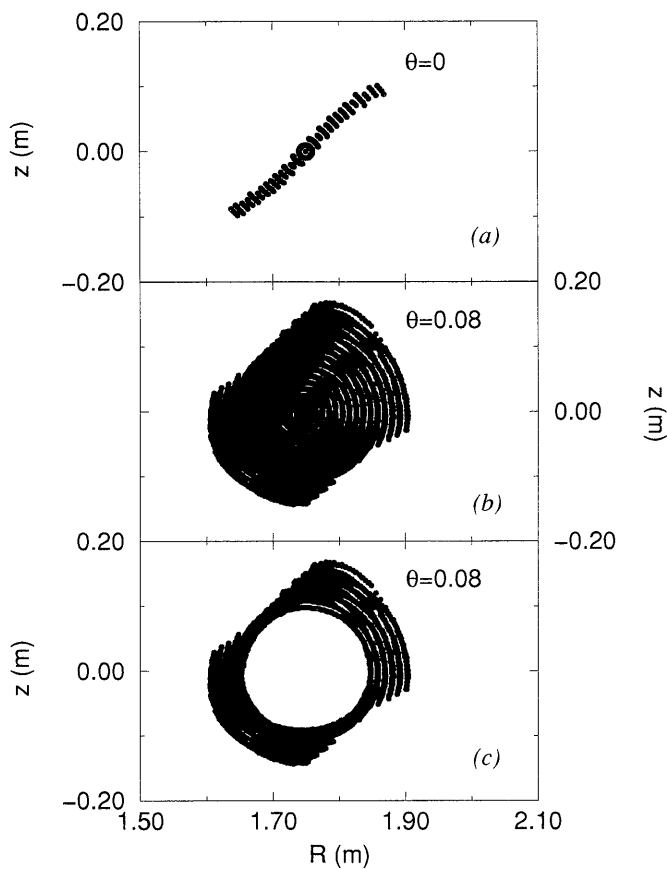


Figure 7.2: Calculated shape of the synchrotron spot (poloidal projection) resulting from runaways ($\gamma = 50$) on nested drift surfaces in a toroidal helical geometry, taking into account pitch angle and the pitch of the magnetic field. (a) $r \in [0, 15]$ cm and $\theta = 0$, (b) $r \in [0, 15]$ cm and $\theta = 0.08$ and (c) runaway shell $r \in [10, 15]$ cm and $\theta = 0.08$. No shift of the runaway beam was taken into account in the simulations ($R = 1.75$ m). A parabolic $q \equiv q_D$ -profile was assumed ($q_0 = 0.88$).

guiding center orbits. In [18], the angle β in the poloidal plane between equator and a line in direction of the inclination is given by

$$\tan \beta \approx D/(q(r)R_0) \quad (7.1)$$

where D is the distance between the observed runaways and the detector and $q(r)$ is the local safety factor of the magnetic field. This relation follows from a simple geometrical argument: $\tan \beta = \Delta z/\Delta R$; in a plane perpendicular to the poloidal plane $\Delta z = DB_p/B_t$ (where B_p is poloidal and B_t toroidal magnetic field) and using $q(r) \approx (rB_t)/(R_0B_p)$ with $r \equiv \Delta R$ the above expression (7.1) is found.

In [17], it has been found that the rotational transform $1/q_D$ of the orbit for a runaway electron decreases, when the runaway energy increases, while the radius of the orbit is almost constant during the acceleration. For the more usual runaway regimes with lower energies, there is no significant difference between the safety factor of the magnetic field lines q and that of the particle drift orbits q_D when equal radii of magnetic field line surface and drift surface are considered ($r = r_D$). However, for particles at $r_D = r$ that were accelerated from almost zero energy to an energy of several MeV, the final q_D is larger than q . Or, the orbits of high energetic runaways with equal safety factor as that of magnetic field lines ($q_D = q$) have a smaller minor radius than the magnetic field lines. In this paper, where high energetic runaways are considered, we expect a difference between drift surface topology (which is measured) and magnetic surface topology and we, therefore, take q_D where q is written in the literature (as e.g. in [18], (7.1)).

A second order effect caused by the locally dependent angle of the drift orbits with the equatorial plane, leads to an additional asymmetry in the synchrotron pattern. For the TEXTOR-94 geometry, it means that the upper half of the synchrotron pattern is larger than the part below the equatorial plane. For the q_D and runaway beam dimension presently considered, the difference between the HFS and LFS angles is of the order of a few degrees. Therefore, the effect of that difference on the synchrotron pattern will be hardly measurable (see fig. 7.2).

Fig. 7.2 shows that the synchrotron pattern is only a narrow curve in the case of a runaway beam with $r_{\max} = 15$ cm for $\theta = 0$. If θ is larger, this curve broadens in the direction perpendicular to the line that fits the inclination of the pattern. The effect of the pitch angle is that, depending on its value, only part of the total synchrotron radiation emitted by the runaways falls onto the detector. If θ is sufficiently large, the total amount of radiation would be detected.

In fig. 7.3, the characteristic dimensions of a synchrotron radiation pattern are shown: a radius r_{\parallel} , parallel with respect to the line corresponding to the

inclination prescribed by (7.1) for a certain q_D , and a radius r_\perp , perpendicular to that line. From the synchrotron pattern parameters measured from the

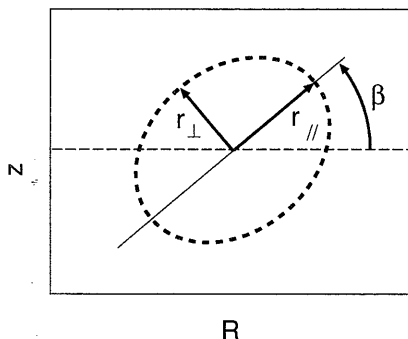


Figure 7.3: Definition of r_\perp and r_\parallel . Angle β is given by the expression (7.1).

observed IR pictures, runaway parameters (r_{\max} , r_{\min} and θ) can be derived. From the simulated patterns, it is known that the r_\parallel corresponds to the maximum of the runaway beam radius r_{\max} for all possible pitch angle values. In case of a runaway shell, r_\perp corresponds to the minimal shell radius r_{\min} .

7.3 Runaway snake observations

7.3.1 Observation of runaway snake in part of poloidal cross section

In [11], a description is given of a discharge which revealed a runaway snake, which we will shortly summarize. Recent observations are discussed more detailed in the next few sections.

The IR camera view used in [11] covered only a part of the poloidal cross section. The IR pictures taken during a steady Ohmic runaway discharge, showed one bright spot and changed only slowly corresponding to the growth of the runaway population. After the synchrotron radiation was well established, a pellet was injected from the LFS. The pellet injection was followed by oscillations in the magnetics, density, ECE and hard x-ray signals. As a result of the injection, the synchrotron radiation pattern showed three distinct phases. First, after the pellet injection, the radiation decreased within about 0.6 ms. Only a small part of the runaways remained confined showing a synchrotron spot strongly reduced in size. Secondly, about 100 ms after the pellet injection, the spot of synchrotron radiation broke up into many

smaller ones. This is caused by the scanning of the camera. This breaking up was visible for several frames. The oscillations of the synchrotron radiation showed the same time structure as the magnetics, density, ECE and hard x-ray signals that are a sign for high MHD mode activity. Finally, after the decay of the MHD modes, again one large synchrotron spot was detected, which stayed in same position without change of intensity or size for more than 600 ms, up to the end of the discharge.

A typical IR picture of a runaway snake is shown in fig. 7.4. The runaway snake event in this figure is described in detail in section 7.3.3. In this single frame ($t = 5.800 - 5.816$ s), the background is subtracted and the contrast of the IR spots enhanced, so that the spots resulting from the rotating runaway drift island are clearly visible.

The spots at the multiple spot pictures in [11] were determined to lie on a circle with a radius comparable with the inversion radius of the sawteeth before the pellet injection. This led to the conclusion that the synchrotron radiation originated from a beam of runaways at the $q_D = 1$ drift surface. The beam was rotating around the torus with a frequency exceeding the picture frequency f_{pict} of the IR camera causing the multiple spot pictures. The rapid loss of a large fraction of the runaway population was ascribed to stochastization of the plasma after the pellet injection during a short time interval. It was hypothesized that this stochastization was due to an overlap of large, low m magnetic islands. The fact that a small beam of runaways survives the stochastic period, shows there is still a big $m = 1$ island confining the runaways.

7.3.2 A: Observation of a runaway snake in full poloidal view

In contrast to the previous example, we now describe a runaway snake observation in full poloidal view. Fig. 7.5 shows \bar{n}_e , I_p , V_{loop} , and the synchrotron signal from the runaways (without background radiation subtraction) of discharge #73189. After 1 s, the first synchrotron radiation is measured as a bright spot in the center of the plasma which grows relatively slowly. Sawtooth activity is absent or otherwise very low ($< 10\%$), as usual in typical runaway discharges. At $t = 2.5$ s, after a steady synchrotron spot established, a pellet is injected from the LFS, which penetrates the plasma to a minor radius of approximately $r \approx 23$ cm as determined from H_α light measurements. The pellet causes the density to rise with ca. a factor 2, and, therefore, it changed, in combination with the rise in V_{loop} , the conditions for runaway generation compared with the period before the pellet injection.

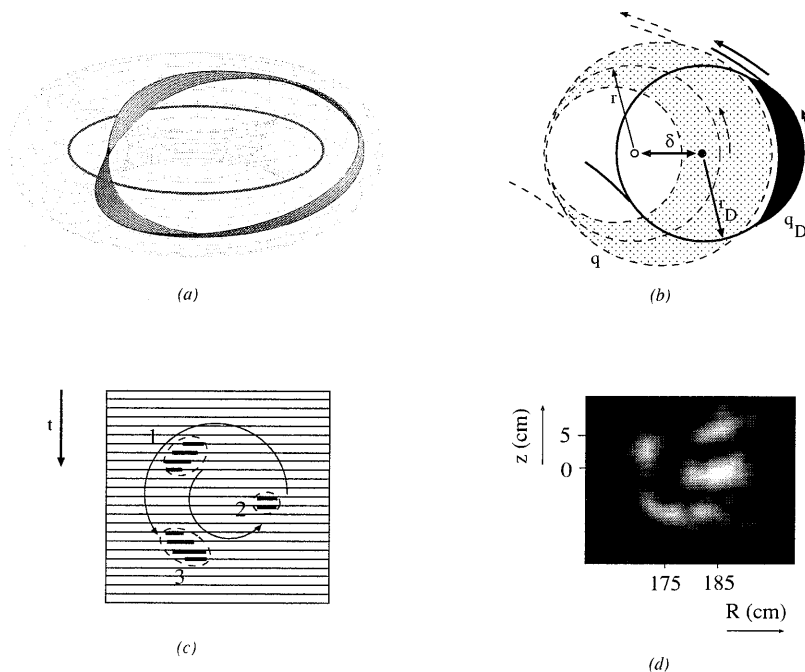


Figure 7.4: (a) Schematic view of a $m = 1, n = 1$ runaway tube in a tokamak; (b) Poloidal cross section, schematically showing a magnetic field surface (dashed line) characterized by r and q with an island, and corresponding drift surface (solid line) characterized by r_D and q_D , also with an island, shifted over distance δ ; (c) One IR picture is build up by scanning from top to bottom. One rotating object (in poloidal projection) can in case of sufficient high rotation frequency sweep across the detector more than once. Spot 2 is originating from the same structure as spot 1, after a rotation of about $4\pi/3(+2k\pi)$ (for integer k) during the time of the relatively slow scanning of only a few camera lines; (d) Typical IR picture (not calibrated) taken at $t = 5.8$ s during a runaway snake event (described in section 7.3.3) after subtraction of the background and optimizing the picture. During the scanning of this single frame (one frame is scanned in ca. 16 ms), the rotating tube of runaways sweeps across the camera view several times.

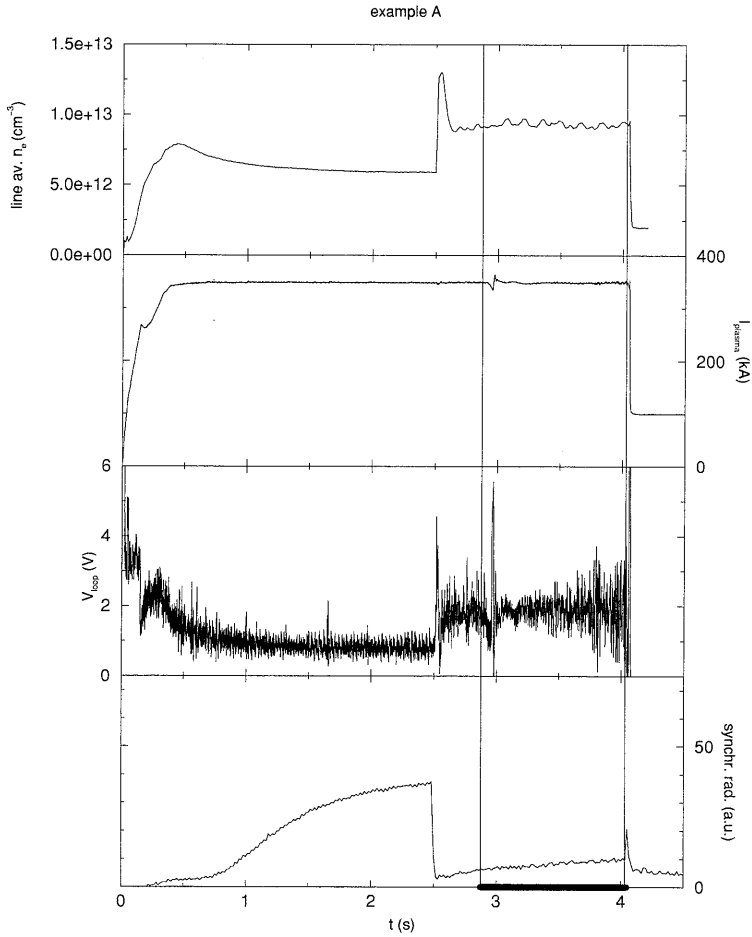


Figure 7.5: \bar{n}_e , I_p , V_{loop} and synchrotron radiation signal for example A, i.e. discharge #73189. $R_0 = 1.75$ m, $a = 0.46$ m, $B_t = 2.2$ T, $q_a = 3.8$. The tail of the I_p signal is an offset error. The synchrotron radiation is shown without subtraction of background radiation. The bold bar on the time axis ($t \in [2.87; 4.03]$ s) indicates the interval during which the runaway snake is observed.

On the density signal, a large oscillation is detected after the pellet injection. The synchrotron radiation vanishes within a few $100 \mu\text{s}$. After ca. 400 ms a small synchrotron radiation spot is detected again, rotating as deduced from subsequent IR pictures. At ca. 4 s, the discharge disrupts.

Fig. 7.6 shows an overlay of subsequent (calibrated) IR pictures in the 2D poloidal cross section, of which a single one is shown in fig. 7.4, for the time interval $t \in [2.87; 4.03]$ s. Every dot corresponds to the central position of

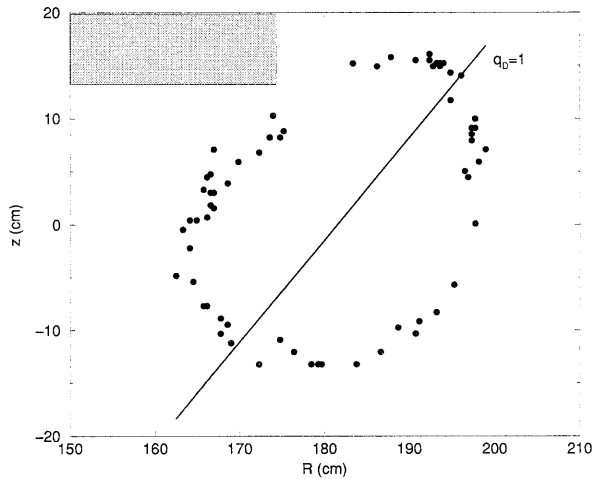


Figure 7.6: *Calibrated synchrotron spots of several subsequent IR pictures (example A, #73189) taken during $t \in [2.87; 4.03]$ s (ca. 70 frames); in the upper left corner the poloidal view is obscured by part of the neutral beam injector. The line indicates the inclination calculated from (7.1) using $q_D = 1$.*

a spot and does not give information about the size of the spot. The shape formed by the spots makes an angle with the equatorial plane of $\sim 30^\circ$. In the upper left corner, part of the poloidal view is obscured by one of the neutral beam injectors. The vertical extent of spots at the left hand side (i.e. HFS) of the IR picture is larger than that of those at the right hand side.

The view in a full poloidal cross section leads to the following conclusions. First, from the overlay of subsequent IR pictures in fig. 7.6, it is observed that the synchrotron spots form an 'ellipse' rather than a circle. As was pointed out in section 7.2, the 'ellipse' shows an inclination. In fig. 7.6 only the central positions of spots are shown. The original IR pictures show that the spots corresponding to the HFS are more elongated, and, therefore, are 'moving' in the scan direction. From that, it is derived that the synchrotron

spots arise from a structure in the plasma, rotating anti-clockwise in the poloidal projection plane, i.e. in electron diamagnetic direction. Finally, in the example shown, no multiple spot pictures are detected, which implies that the rotation frequency is apparently smaller than the scan frequency of the IR camera.

7.3.3 B: Influence of plasma current on a runaway snake

In this example a change in the q profile by changing I_p is investigated. In fig. 7.7, \bar{n}_e , I_p , V_{loop} , neutron signal (measure of runaway loss) and the synchrotron signal (again without background radiation subtraction) are shown (#66526). After 1 s, the first synchrotron radiation is seen as a bright spot at steady central position. At $t = 3.5$ s, two pellets are injected after a gas puff. The first pellet penetrates to a minor radius of $r \approx 32$ cm, the second to $r \approx 24$ cm. The synchrotron radiation vanishes in ca. 30 ms, stepwise from frame to frame. Note that this time is 2 orders of magnitude longer than in example A. After the pellet is injected, oscillations appear, disappear and reappear on the density and magnetic signals, whereas no synchrotron signal is detected. At $t \approx 4.5$ s, runaways have apparently been (re)generated inside the island because synchrotron radiation reappears, now as a smaller spot, rotating around the plasma center. At $t = 5.3$ s; the current starts to decrease with ca. -230 kA/s. During the current decay, synchrotron radiation is still visible as one rotating spot. At ca. $t = 5.75$ s, the spot breaks up into several smaller ones in one single IR picture. The spots disappear, when the discharge ends at $t = 6.27$ s.

For $t \in [4.467; 4.683]$ s where $I_p = 350$ kA (denoted by example B1) and $t \in [5.80; 5.92]$ s where $I_p = 200 - 170$ kA (example B2), spot positions of subsequent (calibrated) IR pictures are shown in fig. 7.8. The synchrotron pattern in example B2 shows a slight inclination. Spots detected in example B1 are more elongated at the HFS than at the LFS of the IR pictures. Hence, the rotation of the runaway beam is counter clockwise as in example A. The vertical extent of the spots becomes smaller the more spots are visible per IR picture, up to a few scanned lines corresponding to about 2 cm (or 390 μ s).

From the fact that the number of spots is increasing in subsequent IR pictures, it is concluded that the rotation frequency is increasing at about 400 ms after the current signal is decaying. Furthermore, it is clearly observed that the radius of the drift surface at which the runaway beam is confined in a drift island shrinks with decreasing current (see fig. 7.8).

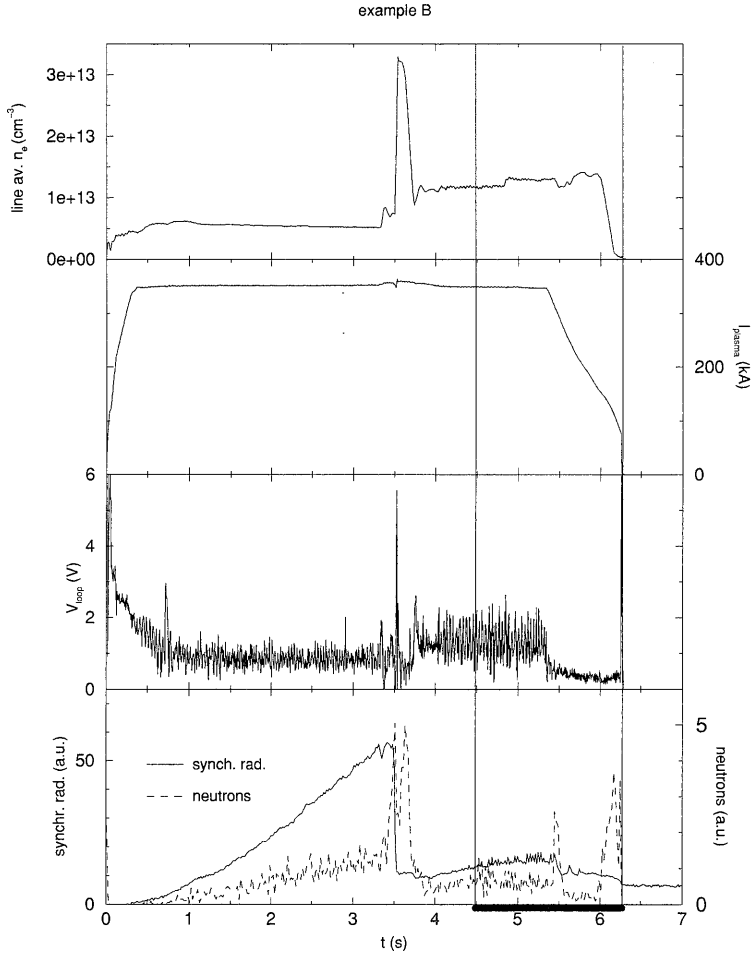


Figure 7.7: \bar{n}_e , I_p , V_{loop} , neutron signal and synchrotron radiation signal for example B, i.e. discharge #66526. $R_0 = 1.7$ m, $a = 0.4$ m, $B_t = 2.2$ T. In example B1, during the flat top phase $q_a = 2.9$, in example B2 during current decay $q_a \approx 5.2$. The synchrotron radiation signal is again shown without background subtraction. The bold bar on the time axis ($t \in [4.5; 6.27]$ s) indicates the interval during which the runaway snake is observed.

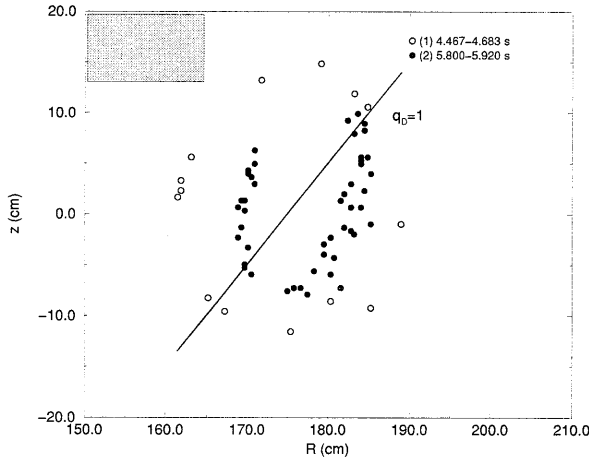


Figure 7.8: *Calibrated synchrotron spots of subsequent IR pictures (example B, #66526) taken at the intervals $t \in [4.467; 4.683]$ s (14 frames) and $t \in [5.8; 5.917]$ s (8 frames). The line indicates the inclination calculated from (7.1) using $q_D = 1$.*

7.3.4 C: Non-pellet induced runaway snake

To study the magnetic field strength dependence of snake parameters, the plasma was shifted to the HFS starting from an Ohmic runaway discharge (#73150). Fig. 7.9 shows \bar{n}_e , I_p , V_{loop} and the synchrotron signal for this case. From $t = 1$ s to $t \approx 3.5$ s, the plasma column is shifted inward from $R = 1.75$ m to $R \approx 1.58$ m, i.e. from $B_t = 2.2$ T to $B_t = 2.5$ at the plasma center. At the same time, the minor radius shrinks from $a = 0.46$ m to $a \approx 0.29$ m. From $t \approx 1$ s, also the first synchrotron radiation is detected. The intensity of the radiation increases slowly to an (overexposed) steady spot. The plasma shift induces MHD activity, shown at other signals. The discharge ends with a disruption at ca. $t = 3.79$ s ($q_{a,cyl} \approx 2.3$). Before the disruption, a part of the large (overexposed) synchrotron spot is rapidly lost at $t = 3.667$ s, leaving a column of small synchrotron spots at the LFS of the torus and, in the same picture, a smaller bright (overexposed) spot in the plasma center region. At the HFS, no small spots can be recognized, possibly due to the overexposure of the detector by the central spot. At the next IR picture, the bright central spot suddenly disappears, together with the spots at the LFS, leaving small spots at both the HFS and LFS observed at a smaller radius than that of the former LFS spots. These spots remain

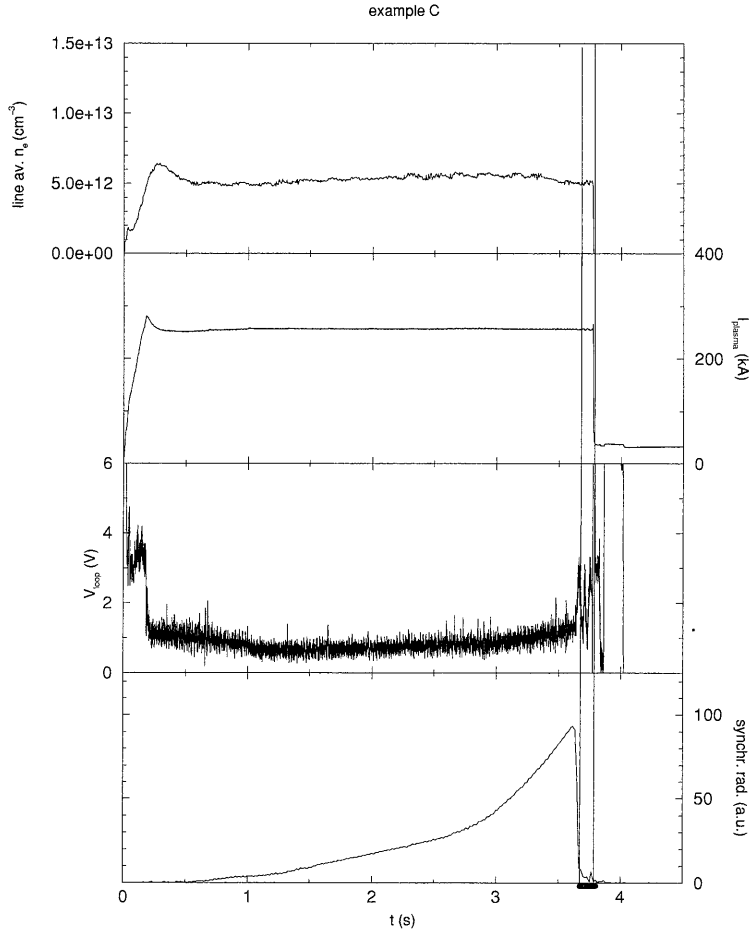


Figure 7.9: \bar{n}_e , I_p , V_{loop} and synchrotron radiation signal (without background subtraction) for example C, i.e. discharge #73150. After the shift (from $t = 1$ s to $t \approx 3.5$ s), $R_0 \approx 1.6$ m, $a \approx 0.30$ m, $B_t = 2.5$ T, $q_a \approx 2.8$. The I_p tail is again an offset error. The bold bar on the time axis ($t \in [3.667; 3.79]$ s) indicates the interval during which the runaway snakes are observed. During this interval, the plasma is not shifted anymore and q_a is constant.

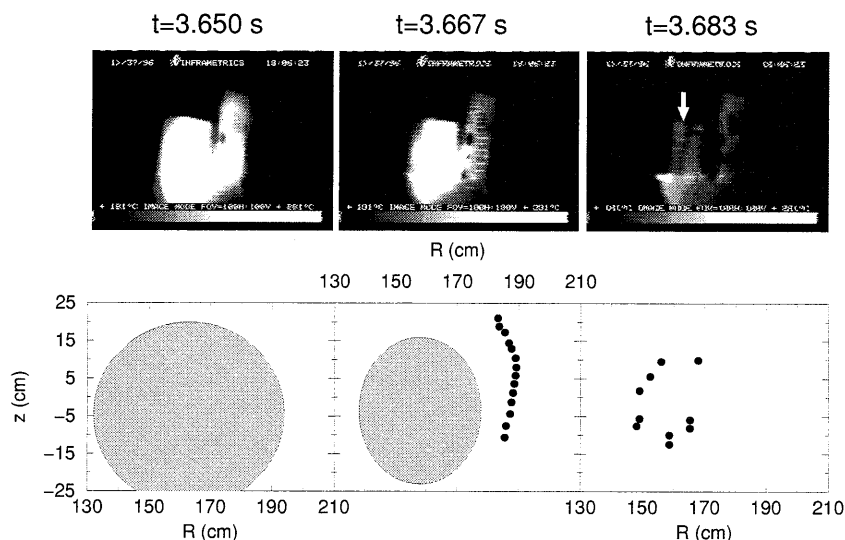


Figure 7.10: Three subsequent IR pictures during MHD activity after plasma shift to the HFS and the corresponding calibrated pictures (example C, #73150) showing spots coming from runaway snakes. The arrow in the IR picture at $t = 3.683$ s points to the spots that are most clearly visible.

visible at a few subsequent IR pictures and then disappear just before the disruption. Fig. 7.10 shows the series of IR pictures as described above. As for example B2, no visible difference in spot length can be recognized between spots at the left hand side and the right hand side of the IR picture.

Fig. 7.11 shows the position of synchrotron spots of a few subsequent IR pictures, observed just before the disruption. At the frame for which the smaller spots at larger radius are visible (referred to as example C1), one big synchrotron spot in the central region is observed, not shown in fig. 7.11. The spots of the following IR pictures (referred to as example C2) form approximately an ellipse with an inclination of about 50° . During the time the runaway snake is observed, the plasma was not significantly shifted anymore.

This example shows the rather spectacular coexistence of a central runaway beam (central synchrotron spot), and a runaway snake (small spots at the LFS) of $q_D > 1$.

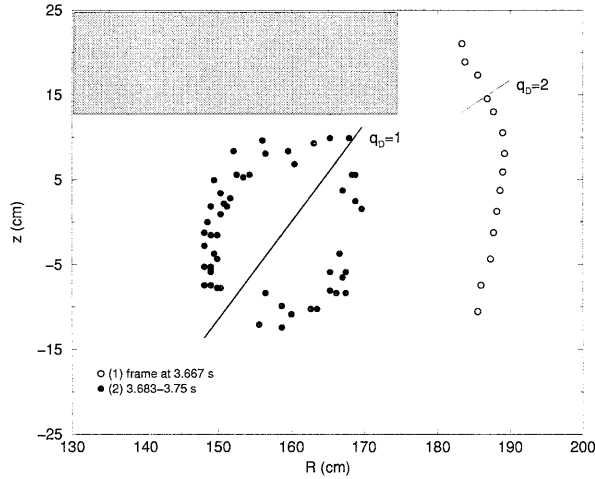


Figure 7.11: *Calibrated synchrotron spots of subsequent IR pictures (example C, #73150) taken at $t = 3.667$ s (one single frame) and the interval $t \in [3.683; 3.717]$ s (2 frames). The lines indicates the inclination calculated from (7.1) using $q_D = 2$ for interval (1) (open circles) and $q_D = 1$ for interval (2) (filled circles).*

7.3.5 Summary of observations

From the above described observations of runaway snakes, the conditions of appearance of a snake are deduced to be large MHD mode activity in a runaway discharge and the loss of a large part of the runaway population. The remaining runaways are confined in an island. When the current decreases, we see that the radius of the drift surface at which the island has developed, becomes smaller. In the experiment where the plasma was compressed, two different snakes, at different drift surface radii, were observed. This experiment further showed that pellet injection is only a way to disturb the plasma and not essential for creating a runaway snake.

7.4 Derived parameters

7.4.1 Drift surface parameters

Because the high energetic runaway electrons experience a large orbit shift, they are only sensitive for magnetic fluctuations with large correlation length,

Table 7.1: Calculated angle of inclination β with respect to the equatorial plane using (7.1), measured r_{\perp} and r_{\parallel} of synchrotron pattern, and estimated drift surface shift δ and runaway pitch angle θ . The radii are measured with help of the lines that corresponds with $q_D = 1$ in example A, B1, B2 and C2 and the line that corresponds with $q_D = 2$ in example C1. The corresponding figures and time intervals during which the runaway snake is visible are indicated.

example	figure	t (s)	β ($^{\circ}$)	r_{\perp} (cm)	r_{\parallel} (cm)	δ (cm)	θ
A	7.5,7.6	2.87-4.03	44 ± 3	14.4 ± 1.2	18.5 ± 0.8	5 ± 1	0.10
B1	7.7,7.8	4.467-4.683	45 ± 2	13.2 ± 1.2	14 ± 2	4 ± 1	0.07
B2	7.7,7.8	5.800-5.917	45 ± 2	7.0 ± 1.2	10.3 ± 1.2	4 ± 1	0.07
C1	7.9,7.10,7.11	3.667	30 ± 2	-	32.1 ± 0.8	-	0.10
C2	7.9,7.10,7.11	3.683-3.75	49 ± 3	9.9 ± 1.2	12.3 ± 1.2	-	0.10

i.e. low mode numbers. The drift surfaces at which a runaway snake has developed, have most likely $q_D = 1$, or in case of example C1 $q_D = 2$. The inclinations β calculated from (7.1) are listed in table 7.1 for the three different examples. Lines with slope $\tan \beta$ through the midpoints (the average of horizontal and vertical spot positions) are shown in the synchrotron spot plots (fig. 7.6, 7.8 and 7.11). The calculated inclinations (assuming $q_D = 1$) fit the orientation of the measured radiation patterns fairly well. Only in example B2 (fig. 7.8), the predicted inclination does not fit the measured one. The predicted inclination is based on the assumption of a circular runaway beam. Probably, during the current decay phase, this assumption is not valid anymore, giving rise to the difference in calculated and measured inclination. For the runaway snake in example C1, only spots at the LFS are visible. It is not possible to see an inclination in that case.

The determination of r_{\min} and r_{\max} of the runaway island follows from the measurement of r_{\perp} and r_{\parallel} of the shell shape in the calibrated IR pictures formed by the the rotating spots in poloidal projection. The results for each example are listed in table 7.1. The determination of r_{\parallel} and r_{\perp} in example B2 was done in the current decay phase. The current decay was only 15% of the maximum value during that time interval, leading to a theoretical decrease in radius of the corresponding magnetic surface of the same order, which is as large as the error in the measurements. Hence, in example B2, although during current decay, still one value is given for both r_{\parallel} and r_{\perp} . From the measured radii, widths of the runaway islands can be estimated, that lie in the range 2 to 4 cm.

Also in table 7.1, the shift of the drift surface δ with respect to the mag-

netic axis is shown. This shift is determined from the distance between the midpoints of the 'elliptical' structures that are shown in the IR pictures and the geometrical tokamak axis. A Shafranov shift of 3 ± 1 cm is estimated between geometrical axis and magnetic axis. Because of relatively large uncertainties concerning the magnetic field topology and plasma position after pellet injection and after the plasma shift, the Shafranov shift is not known more accurately.

The question may arise, why under normal conditions, with an unperturbed plasma, the synchrotron spot shape does not have a clear inclination as in the case of a runaway snake. This may be because in case of a snake the runaways with only one q_D value exist. In an unperturbed runaway discharge, runaways at different q_D surfaces exist, and therefore the total synchrotron spot is an overlay of different shapes as shown in fig. 7.2. Also, a more varied pitch angle distribution in a runaway beam in a unperturbed plasma could result in a spot shape without a detectable inclination.

7.4.2 Runaway energy and pitch angle

The drift surface is shifted from the magnetic surface by a distance δ given in first order approximation by

$$\delta = q\gamma m_e c / eB \quad . \quad (7.2)$$

The shift δ is therefore a measure of runaway energy W_r . In example A, it is found $W_r = 33 \pm 7$ MeV and in example B, $W_r = 26 \pm 7$ MeV, which agrees with previous energy determination [11,13] based on a crude resolution of the IR spectrum. No independent energy measurement has been made for the runaway snakes.

All measured poloidal projections of the synchrotron spots during a snake show complete 'elliptical' shapes. From section 7.2.2, it is clear that this is only possible, if the pitch angle is sufficiently large so that radiation coming from the runaway orbits at r_{\min} falls on the detector. Comparison between calculated and measured synchrotron patterns leads to an estimation of a pitch angle θ of the order 0.1 in example A and C. This is in agreement with previous measurements and Monte Carlo simulations [13]. In example B, $\theta \approx 0.07$ is found. In this example, the inclination did not fit quite well with the assumed one corresponding to the $q = 1$ drift surface as well. Both the pitch angle estimation and the calculated inclination are based on the assumption of circular drift surfaces. Possibly, in example B, during the current decay phase, the plasma shape is no longer circular. For $W_r \approx 30$ MeV and $\theta = 0.1$, there exists an equilibrium between energy gain from the electric field and energy loss due to radiation [13].

7.4.3 Frequency

An estimate of f_{rot} is made by determining the slope of the rotated angle as function of time. In example A, $f \approx 7$ Hz was found, corresponding with density and Mirnov coils signals. In example B1, $f \approx 26$ Hz was obtained. Oscillations on density and magnetic signals have equal frequency during that time interval. In fig. 7.12, the time derivative (in Hz) of the rotated angle is plotted against time for example B2 and C2, together with the frequency derived from other signals of the interferometer, Mirnov coils and ECE measurements. In example C1, $f \approx 3$ kHz was found.

The frequencies of the IR signal are for all examples in agreement with the frequencies on the density and magnetic signals originating from rotating islands in the plasma. This is consistent with the picture that the runaways are confined in an island. The frequencies coming from the rotating islands in the examples A and B1 are much lower than in the other cases, where the frequencies have values that are more typical for $m = 1, n = 1$ or $m = 2, n = 1$ modes in TEXTOR-94. Especially in example A, the mode is rotating slowly for a long time without locking.

7.4.4 Confinement

The loss of runaways after pellet injection and after the plasma shift to the HFS is ascribed to a short period of strong ergodization of the magnetic field. Effective radial diffusion coefficients of $D_{\text{eff}} = a^2/(4\Delta t) \approx 1 - 300 \text{ m}^2\text{s}^{-1}$ are required for the observed losses, where Δt is the time within radiation disappears. The time it takes for the radiation to disappear, varies strongly from discharge to discharge. Apparently, the ergodization is not equally strong in every example. Moreover, the pellets in the examples A and B penetrated to a (minimal) minor radius of about 24 cm, which would correspond roughly to a q value of 2. Still, this is enough to disturb the plasma in the central region where the runaways are confined before pellet injection.

In [11], a radial diffusion coefficient of the runaways in the snake is estimated by

$$D_r = \Delta(w^2)/4\Delta t \quad (7.3)$$

where $\Delta(w^2)$ is the difference in the square of the horizontal extent of the spots, with the result $D_r \approx 0.01 \text{ m}^2\text{s}^{-1}$. The poloidal diffusion coefficient was given by

$$D_\theta = \Delta(l_\theta)^2/4\Delta t \quad (7.4)$$

where l_θ is the filling up of the gaps between the different spots, interpreted as the smearing out of the runaway beam over the drift surface. This last estimation can only be made, when runaways are still present after the magnetic

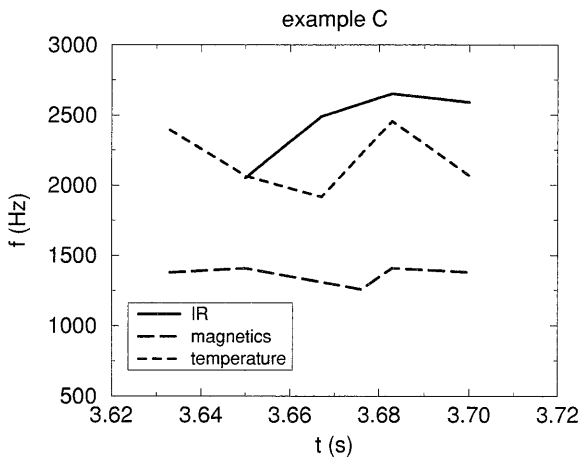
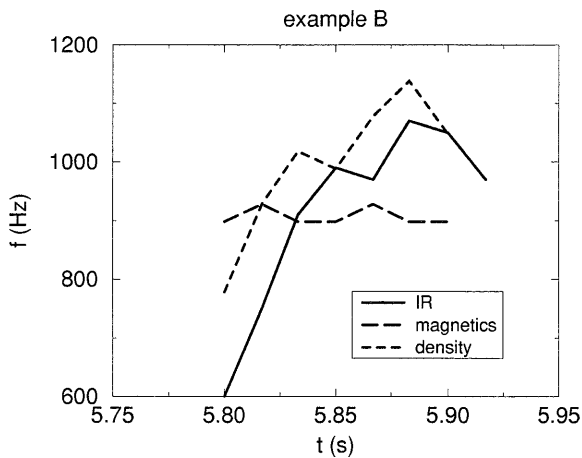


Figure 7.12: Frequency of different signals for example B2 (#66526) and C2 (#73189). The rotation frequency of the synchrotron radiation spots ('IR') is a measure of the rotation frequency of the runaway snake. The oscillation frequency of the magnetic field is derived from the signal of the Mirnov coils. Density and temperature oscillation frequencies are derived from the interferometer and ECE signals.

perturbations have decayed, smearing out poloidally over the drift surface. It was found $D_\theta \approx 0.015 \text{ m}^2\text{s}^{-1}$. As reported in [11], it was observed in a few cases that after the magnetic modes had decayed in about 0.2-0.3 s, indeed the multiple spots form one large spot again. That spot stays approximately in same position without large changes in intensity and size for more than 0.6 s, that is up to the end of the discharge. In other cases, the synchrotron radiation disappeared after the decay of the modes.

Of the examples A, B and C that are discussed in the present paper, only the discharge in example B did not end in a disruption. In that discharge, magnetic perturbations are seen on the magnetics until the end of the discharge. When the magnetic modes decay, the formation of one spot after the snake event would be observed as reported in [11]. This is not the case in example B: the runaway snake is visible until the discharge disrupts. Also, in other similar experiments, no observations have been made of a poloidal smearing out of the runaways over the drift surface, giving rise to a complete shell of synchrotron radiation.

7.5 Discussion

7.5.1 Runaway parameters

Classically, the radius of the drift surface equals that of the magnetic field line surface with same q value. Unfortunately, no accurate experimental data concerning the q profile was available because of the low density conditions of runaway discharges. For the $q = 1$ surface, a radius is estimated with $r = a/q_a$. Using the appropriate parameters for each snake example and compare these results with the measured $(r_\perp + r_\parallel)/2$, we see that for the examples B1, B2 and C1 the measured average radius is in good agreement with the estimation. In example A, $(r_\perp + r_\parallel)/2 \approx 16 \text{ cm}$ is found, whereas $r = a/q_a \approx 12 \text{ cm}$. A possible cause for this difference is that the current density profile is more peaked due to the presence of large MHD islands, so that the $q = 1$ surface lies further out and matches the data better. In example C2, $r_\parallel = 32 \text{ cm}$ and this very likely corresponds to the $q = 2$ surface. In this case, the discharge disrupts shortly after the snake observations have been made because the $q = 2$ limit has been reached.

From the comparison between the calculated inclinations β for the synchrotron pattern and the overlaid spot pictures, and from the considerations concerning the calculated and measured drift surface radii, it is concluded that in example A, B1, B2, and C2 a $q = 1$ snake and in example C1 a $q = 2$ snake was observed.

7.5.2 Higher order theory

From a relativistic Hamiltonian description of drift orbit topology of relativistic particles [17], it was concluded that if higher order energy terms become significant, the radius of drift surfaces is smaller than that of magnetic surfaces with equal q value. Also, the shift of the drift surface with respect to the corresponding magnetic surface is larger than predicted in the first order approximation. Fig. 7.13 shows that the effect of the higher order

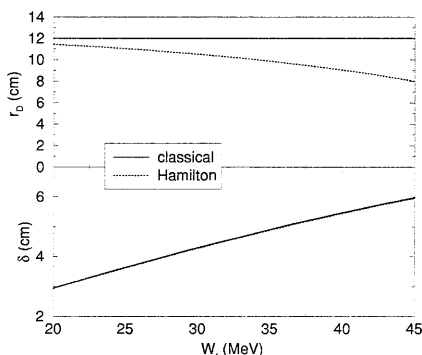


Figure 7.13: Shift δ and radius r_D of the drift surface with $q_D = 1$ as function of runaway energy W_r , in 'classical' approximation and when higher order energy terms are taken into account ('Hamiltonian description'). In the 'classical' approximation, $r_D = r$ when $q_D = q$. This example is calculated for a parabolic q profile, with $q_0 = 0.88$, $I_p = 350$ kA, $R_0 = 1.75$ m and $a = 0.46$ m (parameters of example A). From this, it follows $r_{q=1} = 12$ cm.

energy terms (parameters taken from example A) for the energy range of the runaway electrons that we observe (20-30 MeV) is for the drift surface radius of the order of a few cm. Fig. 7.13 further shows, that the effect on the drift orbit shift, for the energy range that we consider, is too small to be measured with the experimental accuracy we have.

Although the runaways reach relativistic energies in TEXTOR-94, the measurements of the drift surface radius do not show a significant difference from the classical approximation as far as the experimental accuracy allows such a comparison.

7.5.3 Island width

The difference $w = r_{\parallel} - r_{\perp}$ (2 to 4 cm for the different examples) is interpreted as the minimal width of the drift island in which the runaway beam is confined. Assuming that the drift island and the magnetic field island have equal width, an estimate of the magnetic perturbation (tearing mode) can be made by (see e.g. [16])

$$\hat{B} = \frac{mq'B_{\theta}w^2}{16rq} \quad (7.5)$$

where \hat{B} is the amplitude of the radial magnetic field perturbation, m the poloidal mode number, B_{θ} the poloidal magnetic field strength and $q' = dq/dr$ the shear of the magnetic field. In example A, $\hat{B} \approx 5 \times 10^{-4}$ T is found.

7.5.4 Changes in q profile

The snake examples B and C were studied to investigate the effect of changes in current and magnetic field strength on the synchrotron pattern or runaway parameters. Because the exact q profile could not be measured, only qualitative statements can be made.

In example B, it was measured that with lower current the radius of the $q_D = 1$ surface decreases. This is what one expects for the magnetic field surfaces of corresponding q . The increase of the magnetic field strength in example C by the plasma shift was only about 15% compared with the typical field strength. The effect on the q profile with $q_a = 2\pi a^2 B_t / (\mu_0 R I_p)$ is, however, dominated by the changing a and R due to the plasma shift. In the case of a parabolic profile, the magnetic surface radii in the plasma before the shift and after the shift differ only a few cm. The increase in B_t only by shifting the plasma is not sufficient to measure an effect of the changing q profile on the snake parameters.

7.5.5 Transport

From the examples, it is seen that the runaway drift islands are shifted from the magnetic islands to which they correspond. Although the runaways are well confined in a drift island, they actually move in regions where magnetic surfaces are perturbed.

Classical, collision induced transport of runaway electrons would be of the order of $D_r = 0.001 \text{ m}^2\text{s}^{-1}$ or even less. In unperturbed Ohmic runaway discharges it is found $D_r < 0.01 \text{ m}^2\text{s}^{-1}$ [19], which is comparable with the measurement of D_r in a runaway snake. For comparison, in Ohmic discharges

thermal transport is of the order $\chi_e \approx 1 \text{ m}^2\text{s}^{-1}$. One mechanism to enhance runaway transport from the classical estimation is magnetic turbulence since electrostatic turbulence should have negligible effect on the high energetic runaways. In a model, where the magnetic topology in an unperturbed plasma is described by regions of good surfaces and of stochasticity [20], D_r is found to be predominantly determined by the transport in the good zones and to be lower than χ_e , as is in fact measured. The similar runaway transport coefficients in unperturbed plasmas and inside runaway snakes (i.e. drift islands assumed to consist of good surfaces) are fully consistent with this picture.

In [11], cases are discussed in which the magnetic islands decay and the runaway tube spread out over the drift surface to form a shell. Shell shaped synchrotron patterns have not been detected with the full view set-up, because the MHD activity in the snake discharges did not develop in similar ways and often the discharges ended with a disruption.

7.5.6 Acceleration inside a runaway snake

In examples A and B, synchrotron radiation reappeared after the loss shortly after the pellet injection. This reappearance can have several causes. First, newly born runaways could be generated inside the snake after the total runaway population was lost shortly after the pellet injection. In that case, the n_e -dependent primary generation of runaways - acceleration by the electric field taken into account Coulomb collisions - is negligible, because n_e was increased up to a factor of 2 due to the pellets. The secondary generation process, at which already existing runaways kick (thermal) electrons into the runaway regime by close collisions is the main source. Inside a drift island, runaways remained confined and form the seed population needed for the secondary generation. Outside a drift island, however, runaways are absent because of the losses by magnetic turbulence shortly after the pellet injection or plasma shift and, therefore, there is no runaway population to create new runaways by secondary generation. Although no synchrotron radiation was observed by the eye in the IR pictures, a very small number of runaways should be still confined in the remnants of an island after the period of ergodization. The radiation they emit should be of too low intensity to be detected.

It also could be that runaways that were generated before the pellet injection, are still present after the injection but have lost energy. Because the wavelength of the synchrotron radiation is energy dependent, it could be out of the range that is detected by the IR camera. After a re-acceleration, runaways could again gain enough energy, resulting in the reappearance of

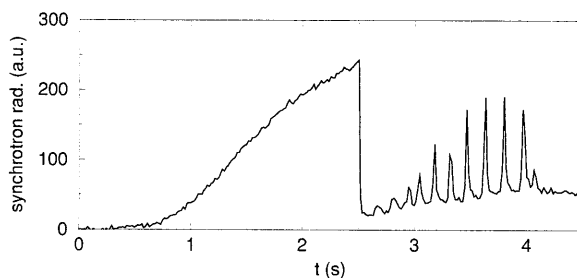


Figure 7.14: *Local evolution of the synchrotron radiation (example A) within a small fixed area in the IR pictures, at which, after the pellet injection at $t = 2.5$ s, the runaway snake appeared (shown here without background subtraction). The generation rate of runaways before the snake and the generation rate inside a snake, given by a curve through the maxima that correspond to the spots originating from the runaway snake, can be compared. The decrease of the maxima towards the end of the discharge is caused by the enhanced magnetic turbulence leading to the disruption at $t \approx 4$ s (see also fig. 7.5).*

synchrotron radiation.

Finally, the wavelength of the synchrotron radiation is not only dependent on the runaway energy, but also on the pitch angle θ . The reappearance of synchrotron radiation could also be the effect of an increased θ instead of an energy gain.

The typical time scale for runaway generation is larger than the in example A measured time interval between pellet injection with the corresponding radiation loss and the reappearance of radiation, as can be seen from fig. 7.14. In this figure, the local synchrotron radiation evolution is shown before and after pellet injection within a small area in the IR pictures where the runaway snake appeared after the pellet injection. The rise in radiation takes longer before the pellet injection than after the pellet injection. Furthermore, θ of the runaways inside the snake is estimated to be of similar value as before the pellet injection, for both example A and B. This leads to the conclusion that the reappearance of synchrotron radiation in the case of example A is caused by the re-acceleration of the runaways after they have lost energy by the pellet injection. In example B, both generation and re-acceleration can cause the reappearing synchrotron radiation. During the generation or re-acceleration phase, runaways should be confined inside the island, which shows a low radial diffusion rate.

7.6 Summary and conclusion

We have presented new observations of the runaway snake phenomenon. Of these new observations we discussed three examples in detail, distinguishing three different situations: a runaway snake viewed in the full poloidal cross section under similar plasma conditions as previous runaway snake observations done in only part of the poloidal cross section [11]; a runaway snake at different plasma current; a runaway snake at high magnetic field strength. Necessary conditions for creating a runaway snake are MHD activity and an initial loss of a large fraction of the runaways. Methods that were used to excite the necessary MHD activity were pellet injection and plasma shift to the HFS. In all the three examples, a $q = 1$ runaway snake was observed, in the case of the plasma shift also a $q = 2$ runaway snake appeared.

Synchrotron patterns are calculated taking into account the pitch of drift orbits, in first approximation equal to the pitch of the magnetic field lines, and the gyration motion of the electrons. The simulations agree with the analytical expressions [18] concerning the shape of the synchrotron spot. From the simulations and the measured synchrotron pictures, runaway parameters as for instance drift surface radius and shift, energy and pitch angle due to the gyration have been derived. In first order approximation, the measurements are understood quite well. Effects due to the relativistic energies on drift surface radius were not measured.

The short phase after pellet injection or plasma shift is characterized by ergodization. Due to macroscopic magnetic turbulence, a large number of existing runaways is lost. In several cases, a small fraction of runaways remain confined inside islands that exist after that period. Transport of runaways that are confined inside such an island structure is very low, of the order of $0.01 \text{ m}^2\text{s}^{-1}$, which is comparable with the runaway transport coefficient in unperturbed plasmas. This result fits into the picture of a plasma in which runaway transport is dominated by magnetic turbulence, and in which the magnetic topology is described by bands of stochasticity and good surfaces. In that model, the effective runaway diffusion coefficient is mainly determined by the zones of good surfaces, which explains the comparable estimates of D_r in perturbed and unperturbed plasmas. The rapid loss outside and the good confinement inside a drift island are fully consistent with magnetic turbulence as the main cause of runaway transport.

Finally, the study of the runaway snakes in general does not only give the opportunity to check several models concerning drift orbit and magnetic field topology and it could not only give more insight into tokamak transport, it also could provide a tool to make island structure visible in the plasma interior. This could be interesting for studies of ergodic divertors, like the

planned dynamic ergodic divertor (DED) in TEXTOR-94 [21].

Acknowledgments

We like to thank the TEXTOR team for operating TEXTOR-94 and J. Hübner for the operation of the pellet injector and evaluating the pellet parameters. We are grateful to I. Pankratov for helpful discussions. This work was performed under the Euratom-KFA and Euratom-FOM association agreements with financial support from NWO and Euratom.

References

- [1] Knoepfel H, Spong D A, Nucl. Fusion **19** (1979) 785
- [2] Gill R D, Nucl. Fusion **33** (1993) 1613
- [3] Joyer P, Martin G, Controlled Fusion and Plasma Heating (Proc. 17th Eur. Conf. Amsterdam 1990) **14B** Part I 303
- [4] Rosenbluth M N, Putvinski S V, Nucl. Fusion **37** (1997) 1335
- [5] Yoshino R, Kondoh T, Neyatani Y, Itmai K Kawano Y, Isei N, Plasma Phys. Contr. Fusion **39** (1997) 313
- [6] Mynick H E, Strachan J D, Phys. Fluids **24** (1981) 695
- [7] Kwon O J, Diamond P H, Wagner F, Fussmann G, ASDEX and NI teams, Nucl. Fusion **28** (1988) 1931
- [8] Catto P J, Myra J R, Wang P W, Wootton A J, Bengtson R D, Phys. Fluids B **3** (1991) 2038
- [9] Myra J R, Catto P J, Wootton A J, Bengtson R D, Wang P W, Phys. Fluids B **4** (1992) 2092
- [10] Esposito B, Martin Solis R, van Belle P, Jarvis O N, Marcus F B, Sadler G, Sanchez R, Fischer B, Froissard P, Adams J M, Cecil E, Watkins N, Plasma Phys. Contr. Fusion **38** (1996) 2035
- [11] Jaspers R, Lopes Cardozo N J, Finken K H, Schokker B C, Mank G, Fuchs G, Schüller F C, Phys. Rev. Lett. **72** (1994) 4093

- [12] Finken K H, Watkins J G, Rusbldt D, Corbett W J, Dippel K H, Goebel D M, Moyer R A, Nucl. Fusion **30** (1990) 859
- [13] Jaspers R, PhD Thesis *Relativistic runaway electrons in tokamak plasmas*, Eindhoven University of Technology, The Netherlands (1995)
- [14] Weller A, Cheetham A D, Edwards A W, Gill R D, Gondhalekar A, Granetz R S, Snipes J, Wesson J A, Phys. Rev. Lett. **59** (1987) 2303
- [15] Wesson J A, Plasma Phys. Contr. Fusion **37** (1995) A337
- [16] Wesson J, *Tokamaks* Oxford University press (1987)
- [17] de Rover M, Lopes Cardozo N J, Montvai A, Phys. Plasmas **3** (1996) 4468; de Rover M, Lopes Cardozo N J, Montvai A, Phys. Plasmas **3** (1996) 4478
- [18] Pankratov I M, Plasma Phys. Reports **22** (1996) 535
- [19] Entrop I, Lopes Cardozo N J, Jaspers R, Finken K H, Plasma Phys. And Contr. Fusion **40** (1998) 1513
- [20] Hegna C C, Callen J D, Phys. Fluids B **5** (1993) 1804
- [21] Finken K H et al, Fusion Engineering and Design **37** (1997) 335-450

Chapter 8

Disruptions, fast pitch angle scattering and transport barriers

In this chapter, several topics are discussed that are only marginally related to the main questions of this thesis. Nevertheless, they are worth a short presentation because of major importance for future tokamaks or because of better insight into runaway behavior in tokamaks in general. First, the observations of runaway electrons during disruptions are presented. Then, it is investigated how a possible electron transport barrier affects the runaway measurements. Finally, observations of fast pitch angle scattering (FPAS) are discussed.

8.1 Disruptions

8.1.1 Introduction

A disruption is a sudden loss of energy confinement of the plasma. In [1], the loss is ascribed to a turbulent destruction of the magnetic surfaces. Before a disruption, often magnetic modes are observed. These modes can grow and eventually overlap, which leads to stochasticity of the magnetic field structure. The plasma energy is lost and the temperature rapidly drops. The plasma resistivity strongly increases, which leads to a fast decay of plasma current and very large toroidal electric fields.

A disruption can be disastrous for a future reactor tokamak. First of all, enormous heat loads on wall components can evaporate, crack or melt the wall materials. Because the plasma position varies, large electric fields

are induced that give rise to large currents in the vessel. These currents induce enormous $\mathbf{j} \times \mathbf{B}$ forces on the vacuum vessel structure. Secondly, the induced toroidal electric field after the sudden temperature drop can generate and accelerate runaway electrons. The runaway electrons generated in a disruption are especially dangerous because the energy in the runaway beam can be deposited very locally due to the outward drift or a position instability. Also, the runaway electrons could possibly reach such high energies (hundreds of MeV) that they penetrate the first wall and cause leakage into the vacuum vessel of the cooling system of the plasma facing components.

It is of major importance to avoid or control disruptions in future tokamaks. For that reason, much effort is put into investigations to understand the actual mechanisms leading to a disruption [2]. Several classes of disruptions are distinguished, such as the low q_a limit or the so-called density or radiation limit. In case of a low q_a limit, the edge safety factor is close to two. Magnetic modes ($m = 2, n = 1$) are growing and the plasma disrupts. In case of a density or radiation limit, a certain critical density is reached at which the radiation power of impurities (due to bremsstrahlung or line radiation) that is proportional to the square of the density, exceeds the amount of input power by Ohmic heating and additional heating. This mostly leads to an MHD unstable situation.

Part of the disruption studies concern the particular problem of runaway generation during disruptions [3–9]. Especially, the question is discussed whether the runaways are primarily generated by the primary generation or by secondary generation. In [3, 4], observations of disruption generated runaway electrons in TEXTOR and TEXTOR-94 are discussed on basis of synchrotron radiation measurements. Runaway electrons can indeed reach relativistic energies of at least 20 MeV during disruptions, otherwise these synchrotron radiation measurements were not possible. In [5, 9], methods to avoid the production of runaway electrons during a disruption are presented. Recently, also in JET [6], runaway electrons generated during disruptions have been observed by means of soft x-ray measurements.

In this section, a summary is given of the observations of disruption generated runaways by means of the synchrotron radiation detection, including the observations discussed in [3, 4]. Several sessions have been dedicated to the investigation of runaway generation during disruptions in TEXTOR-94. These experiments were, however, not very successful, in the sense that in none of the discharges, disruption generated runaways were observed.

8.1.2 Observations

Since the observation of disruption generated runaways by means of synchrotron radiation measurements in TEXTOR [3], only two more observations have been made in TEXTOR-94. The discharges are listed below with a short summary of typical parameters.

- #55860: in this discharge, no synchrotron radiation was measured during the stable phase before the disruption. $B = 2.25$ T and $I_p = 275$ kA. A large deuterium puff caused the disruption. The line averaged density after the puff is roughly $\bar{n}_e \approx 5 \times 10^{19} \text{ m}^{-3}$. The thermal quench is at about $t = 2.846$ s. Some 6 ms after the thermal quench, synchrotron radiation is measured during 3 ms. After the thermal quench and about 0.9 ms before the IR signal is visible, the ECE signal (130 GHz), that is dominated by down-shifted suprathreshold radiation, starts to increase again. After the IR radiation (and the ECE signal) disappeared, the plasma current shows a larger decay for ca. 2 ms, after which it shows the former decay rate again. The current decay time directly after the thermal quench is $\tau_{\text{curr}} \approx 4.5$ ms. From $\tau_{\text{curr}} \approx \mu_0 a^2 / 4\eta$ with $\eta \approx 1.65 \times 10^{-9} \ln \Lambda Z_{\text{eff}} / T_e [\text{keV}]^{3/2}$ the Spitzer resistivity and with $Z_{\text{eff}} \approx 2$, this leads to an estimate of electron temperature of $T_e \approx 25$ eV. In [4], an accurate investigation of this disruption showed that the runaway electrons are mainly produced by the secondary generation process.
- #64845: in the stable phase before the disruption, $B = 2.25$ T and $I_p = 360$ kA. No synchrotron radiation was measured. Before the thermal quench at $t = 1.467$ s, MHD activity was observed. Some 30 ms after the thermal quench, synchrotron radiation is measured during two subsequent frames of the IR camera (one frame per 16 ms). After accurate analysis, the ECE signal (130 GHz) is visible after the quench up to 1.53 s at a very low level. No phase of larger current decay is seen after disappearance of the IR radiation. The loop voltage before the disruption was 1.5 – 2 V which is rather high for a normal Ohmic discharge. It indicates a relatively high value of Z_{eff} . Directly after the disruption, roughly $\bar{n}_e \approx 1 \times 10^{19} \text{ m}^{-3}$ and $\tau_{\text{curr}} \approx 5$ ms, from which the electron temperature $T_e \approx 37$ eV is estimated (with $Z_{\text{eff}} \approx 5$). In [4], it was concluded that in this case, the secondary generation was only weak and that the runaway electrons could have been generated already before the actual disruption.
- #65763: in this discharge, synchrotron radiation was measured before the disruption. About 2.5 s before the disruption, the discharge

reaches the slide-away regime. The plasma current then increases with roughly 12%, up to 400 kA. $B = 2.25$ T. At $t = 3.03$ s, the plasma disrupts. About 64 ms after the thermal quench, synchrotron radiation is measured during three frames of the IR camera. An ECE signal (130 GHz) is visible after the quench at a very low level up to approximately $t = 3.09$ s. No phase of larger current decay is seen after disappearance of the synchrotron radiation. The disruption was triggered by the injection of a pellet. Directly after the disruption, roughly $\bar{n}_e \approx 3 - 4 \times 10^{19} \text{ m}^{-3}$, $\tau_{\text{curr}} \approx 5$ ms, from which the electron temperature $T_e \approx 25$ eV is deduced (again $Z_{\text{eff}} \approx 2$).

In summary, all the disruption generated runaways measurements are done at disruptions with a very fast current decay. This rapid current decay is related to a very cold phase directly after the disruption. The resistivity increases enormously. For example, when T_e drops by a factor 40 (from typically 1 keV to about 25 eV), the resistivity η increases with a factor $40^{3/2} \approx 250$ without taking the rise in Z_{eff} into account. This high η is observed from the loop voltage V_{loop} that saturates shortly after the thermal quench. A saturation occurs when $V_{\text{loop}} > 40$ V. The above discharges do not show minor disruptions before the final major disruption.

8.1.3 Experiments

Several disruption programs have been carried out at TEXTOR-94 to investigate disruptions in general, e.g. mode locking [10] and Greenwald density limit or radiation limit [11, 12]. During these programs, the IR camera was always running to detect synchrotron radiation coming from disruption generated runaways. The different disruption programs lead to about 80 disruptions. Unfortunately, none of these resulted in more observations of disruption generated runaways. Below, the experiments on disruptions are shortly described.

Different methods have been used to make the plasma disrupt. First, several series of disruptions were made at which the edge safety factor q_a gets close to 2. Because $q_a \propto B/I_p$, this $q_a = 2$ limit can be reached by a decrease of the toroidal magnetic field B at constant plasma current I_p or a current ramp at constant B . Another way of reaching the low q_a limit is by compressing and shifting the plasma inward or outward. Typical plasma parameters at the low q_a limit disruptions:

- constant current operation at $I_p = 350$ kA, decreasing B from a maximum field $B = 1.8$ T;

- constant current operation at $I_p = 250$ kA, decreasing B from a maximum field $B = 2.2$ T;
- constant magnetic field operation at $B = 1.2$ T, current ramp starting from $I_p = 250$ kA, with and without additional heating by means of 1 MW NBI (co-direction with respect to plasma current);
- constant current operation at $I_p = 250$ kA, compressing and shifting the plasma outward or inward at a magnetic field of $B = 2.6$ T and $B = 2.2$ T.

Secondly, many discharges were devoted to the study of the density or radiation limit. Typical plasma parameters:

- constant current and magnetic field operation at $I_p = 250$ kA and $B = 2.0$ T, density ramp, both with and without additional heating by means of co- and counter-injection of NBI.

8.1.4 Discussion

The question arises whether we could have measured runaway electrons at all in the disruptions presented in the previous section. The presented observations of disruption generated electrons suggest that a fast current decay, i.e. a very cold phase after the thermal quench, that produces a large toroidal electric field is important. In [3], a model for runaway generation during disruptions is presented which calculates the maximum runaway energy and the runaway current as function of the parameter $\varepsilon = E/E_{\text{crit}}$ with E_{crit} the critical runaway field. An estimate for ε is given by $\varepsilon \approx 4.6 \times 10^{-9} Z_{\text{eff}} j_0 / n_e \sqrt{T_e}$ where j_0 is the central current density approximately equal to that just before the disruption and n_e is measured in 10^{19} m^{-3} and T_e in keV. When $n_e \approx 2 - 3 \times 10^{19} \text{ m}^{-3}$, $T_e \approx 0.05 - 0.10$ keV, $j_0 \approx 1.5 - 2 \text{ MA m}^{-2}$ and $Z_{\text{eff}} \approx 2 - 3$, then $\varepsilon \approx 0.02 - 0.04$, which leads according to the model in [3] to a maximum runaway energy of 15 - 30 MeV. Runaway currents of 0 - 25 kA are reached for $\varepsilon \approx 0.02 - 0.04$. The above mentioned parameters are not untypical for the presented disruptions. Therefore, it is concluded that it should have been possible to observe disruption generated high energetic runaway electrons. The maximum energy can also be estimated directly from the energy gain that comes from the decaying poloidal field, via inductively generated parallel electric field E . This yields [3] $\delta W = ec \int E dt \approx ecL\delta I_p / 2\pi R_0 \approx 21 \text{ MeV}$, with L the total inductance and δI_p the current loss between thermal quench and the time at which the energy content is determined.

The presented observations suggest that high energetic runaway electrons during disruptions are observed as long as the magnetic field structure is not completely destroyed during a disruption. Generated runaway electrons should be confined at few intact magnetic field surfaces for some time to reach 'observable' energies of 25 – 30 MeV. This is consistent with the observation in JT-60 [5], where the generation of runaways after fast plasma termination is suppressed by applying external magnetic perturbations, i.e. by destroying magnetic surfaces. In stochastic magnetic fields, runaways are badly confined. This was already observed in chapter 7: runaway electrons outside an island topology are rapidly lost with diffusion coefficients up to $300 \text{ m}^{-2}\text{s}^{-1}$.

At Tore Supra [7], it is found that the runaway generation at disruptions is a strong function of magnetic field. After an increase of the field with a factor 2.5, many more runaways were generated at disruptions derived from higher neutron rates. Because $\varepsilon \sim j_0 \sim B/R_0$, a stronger field can indeed lead to a larger runaway current during disruptions according to the model in [3]. On the other hand, a stronger toroidal magnetic field could also reduce the relative effect of perturbing fields and, therefore, keep the magnetic structure better intact during a disruption resulting in a better runaway confinement. In most of our experiments, the magnetic field is rather low, $B = 1.2 - 2.0 \text{ T}$. Unfortunately, in the only experiments at high magnetic field ($B = 2.6 \text{ T}$), the disruptions are preceded by relatively large mode activity. It is very likely that this leads to the destruction of all magnetic surfaces during the disruption, so that no runaway electron can be confined.

The role of Z_{eff} is not clear at the generation of runaways at disruptions. A high Z_{eff} causes more (edge) radiation, which could lead to a faster temperature decay, i.e. a colder post-quench plasma. Also, plasma resistivity increases with higher Z_{eff} , which leads to a faster current decay. On the other hand, the effect on the primary and secondary generation is found to be rather negative. The birth rate λ_r decreases with increasing Z_{eff} . In [13], runaway generation is investigated in high Z_{eff} plasmas. It was concluded that an increase in Z_{eff} suppresses the secondary generation. In JT-60, it is observed, however, that the injection of an impurity pellet to get a fast plasma shutdown actually favors the generation of runaway electrons by secondary generation. In [13], it is suggested that the very high electric field caused by the high level of Z_{eff} is dominating a reduction of the secondary generation process.

8.2 Runaway electrons as probe for barriers?

8.2.1 Introduction

Measured heat transport in tokamak plasmas exceeds the neoclassical estimates with one or two orders of magnitude. In recent years, in various tokamaks, conditions have been reached for which regions in the plasma develop with an ion diffusivity that is reduced to the neoclassical level [14]. These plasma regions are called ion transport barriers and can be as large as the entire plasma. Electron thermal transport appears to be driven by different mechanisms than that of ions, because the existence of an ion temperature barrier does not imply an electron transport barrier.

Electron transport barriers have been definitely demonstrated at the Rijnhuizen Tokamak Project (RTP), both in Ohmic and electron cyclotron heated (ECH) plasmas [15–17]. The barriers exist in the vicinity of low order rational numbers in the q profile, e.g. $q = 1, 4/3, 3/2, 2, 5/2$ and 3 . The barrier in the vicinity of the $q = 1$ surface is found to be the strongest. The data shows that the barriers extend at maximum over 10% of the minor radius. In [16], a barrier model is presented where the electron heat diffusivity χ_e is prescribed as a function of q . The diffusivity between the barriers that are positioned near $q = 1, 4/3, 3/2, \dots$ is $\chi_{e,\text{out}} = 10 \text{ m}^2\text{s}^{-1}$, the diffusivity in the barriers increases from $\chi_{e,\text{in}} = 0.35 \text{ m}^2\text{s}^{-1}$ near $q = 1$ till $\chi_{e,\text{in}} = 1.8 \text{ m}^2\text{s}^{-1}$ for outer barriers. This interpretative model surprisingly well reproduces the measurements.

It is pointed out in [17] that many of the experimental features of the observed transport barriers resemble the magnetic field topology in a tokamak. In the following, the region of the very low transport is, therefore, interpreted in a magnetic topology picture as a region of good magnetic surfaces near perturbed, stochastic regions.

In this section, a closer look into the IR pictures and into synchrotron radiation profiles (taken at the equatorial plane) under different plasma conditions is made. The analysis of profiles is motivated by the question whether evidence for electron transport barriers can be found in runaway electrons measurements.

8.2.2 Effect of a barrier on runaway electron measurements

Runaway electrons are effectively test particles, not bound to the ions by ambipolar effects, as long as no rapid changes in runaway density occur. Therefore, runaway transport can be compared to heat diffusivity. Simulations with the model presented in [16] can reproduce the measurements when a heat diffusivity inside the barriers is assumed that is roughly one order of magnitude higher than the neoclassical value. It was found that the value of the diffusivity outside the barriers was not very critical in the simulations, but at least half an order of magnitude larger than the averaged χ_e as follows from a power balance. We will now investigate what these findings imply for the case of runaway electrons.

The neoclassical runaway diffusion coefficient is estimated in chapter 2, $D_{r,neo} \sim 10^{-4} \text{ m}^2\text{s}^{-1}$. The diffusion coefficient inside a barrier is therefore taken $D_{r,in} \approx 10^{-3} \text{ m}^2\text{s}^{-1}$. In Ohmic plasmas, it is measured that the effective runaway diffusion is $D_{r,eff} < 0.01\text{m}^2\text{s}^{-1}$. Outside the barrier, we take, therefore, $D_{r,out} \approx 0.1 \text{ m}^2\text{s}^{-1}$, which is even more than half an order of magnitude larger than this averaged diffusion coefficient. Using $D_{r,eff} \approx (w_b/D_{r,in} + (1 - w_b)/D_{r,out})^{-1}$ with w_b the total barrier width, it is estimated that the barriers when existing roughly extend over 10% of the minor radius. For a more accurate estimate, the actual width of a barrier should be considered as well.

In the above calculation, it is assumed that, in the interpretation of barriers as good magnetic surfaces within regions of stochasticity, the mechanisms that cause a $\chi_{e,in}$ of one order of magnitude higher than the neoclassical value, apply to some extent to the runaway electrons. However, when e.g. electrostatic turbulence is the cause for this enhanced $\chi_{e,in}$ inside a barrier consisting of good surfaces, runaway electrons are affected roughly one order of magnitude less (see chapter 2, $D_{es} \propto 1/v$). This would imply that $D_{r,in} \approx D_{r,neo}$. The estimated total barrier width is in that case only 1% of the minor radius. When $D_{r,out}$ is taken one or two orders of magnitude higher, the same result was found for w_b .

Because of the q dependence of the barriers, one of the possibilities to observe evidence for an electron transport barrier in runaway electron measurements is the behavior of the synchrotron spot in the current decay phase. When the current decays, the q value on axis, q_0 , eventually increases to a value above 1. Hence, the $q = 1$ surface vanishes. A possible transport barrier close to this surface then disappears as well. If runaway electrons were confined in the region within the barrier close to the $q = 1$ surface, they would spread out when this barrier disappears, up to a possible next barrier. This

would be observed as an increase of the synchrotron spot on the IR pictures during current decay. Because outside a barrier at least $D_{r,\text{out}} \approx 0.1 \text{ m}^2\text{s}^{-1}$, the spot should increase on a time scale of at the most 500 ms after the barrier at $q = 1$ vanished. Observations of an increase in synchrotron spot have indeed been done and will be presented in section 8.2.3. It will be shown in section 8.2.4 that there are different ways to interpret the observations.

Other evidence for an electron transport barrier could be provided by synchrotron radiation profiles. Let us assume a low density plasma with a few electron transport barriers. The electron temperature profile of this plasma shows very steep temperature gradients [16,17] close to the barriers. Runaway production is strongly concentrated in the plasma regions where the T_e -profile is more peaked than the n_e -profile. Hence, runaways are, as usual, mostly generated in the plasma center, inside the first barrier. Because the transport in this region is very high, the newly born runaways will spread over the whole region up to the barrier. Outside the first barrier, the generation of runaways is expected to be lower and when runaways are generated they are rapidly lost from the plasma or will be kept within the next barrier when present. The resulting runaway source density profile is a staircase profile, i.e. flat in the regions between the barrier position. Outside the last barrier, no runaways are present. The profile is more peaked than the temperature profile because the birth rate of runaway electrons is much more peaked.

The orbit shift of 25-30 MeV runaways is $\sim 6 \text{ cm}$. This is larger than the expected width of the barrier and therefore, these high energetic runaways, born in the region within the barrier, are, partly, moving in a stochastic region outside the transport barrier. When more barriers are present that are only several cm apart, the runaway electrons could even shift across more than one barrier. During its acceleration, i.e. along its increasing orbit shift, a runaway produces new runaway electrons by secondary generation. When the distances between barriers are of the same order of magnitude as the runaway drift orbit shift, a smoothing of the steps of the staircase can occur. Nevertheless, outside the last barrier, no runaways are confined. The 30 MeV runaway density profile is, therefore, at least top-hat shaped. Recall that not the actual magnetic field structure at the position of the runaway orbit, but the actual drift orbit topology is important. This has been shown in chapter 7 where runaways are confined in a drift island that is shifted from the corresponding magnetic island into a stochastic magnetic region. The steep edges in the high energetic runaway profile are shifted from the actual position of the transport barrier.

Only runaway electrons of high energy contribute significantly to the observed synchrotron radiation. Therefore, the observed radiation profiles can be interpreted as the runaway density profiles of 'mono-energetic' runaway

electrons of high energy. Hence, an investigation of these radiation profiles could show evidence for electron transport barriers.

8.2.3 Observations

In this section, we investigate whether evidence of electron transport barriers as discussed in the previous section can be found in the runaway experimental data. In the next section, we discuss to what extent the observations can be interpreted as evidence for transport barriers.

In the current decay phase of most runaway discharges, it is observed that the (small) sawteeth disappear. Although the absence of sawteeth does not necessarily mean that $q_0 > 1$, it is expected that at some time in the current decay phase, where q_a is increasing, $q_0 > 1$. When a transport barrier close to $q = 1$ disappears as well, an increase in synchrotron spot is expected. In [18], observations of rapidly increasing synchrotron spots in the current decay phase of normal Ohmic runaway discharges are presented. Normally in the current decay phase, a stable synchrotron spot is observed. The spot slowly moves outward because the drift orbit drift is inversely proportional to the plasma current. In some discharges, however, the synchrotron spot size suddenly increases within approximately 0.1 ms during the current decay phase. Simultaneously, the synchrotron spot increases in intensity. After this increase, the ECE signal shows a stepwise increase which is characteristic for the Parail-Pogutse instability [19] (see also section 2.4).

Two radiation profiles in the Ohmic phase of two different runaway discharges are shown in figure 8.1. Because the intensity of the synchrotron radiation in the tails is just above the intensity of the thermal background, the typical error in intensity in the tails is relatively large, up to 50%. In the highest intensity part of the profile, the typical error in radiation is typically 10 – 15%.

The profile of #62791 taken at $t = 2$ s is flat in the highest intensity part and shows steep gradients. The discharge #62791 shows an exponentially rising radiation evolution up to the moment of NBI at $t = 2.7$ s. In almost all Ohmic runaway discharges, such an exponential rise of radiation signal is observed, which is interpreted as a dominant secondary generation process. There are, however, few observations of radiation signals that reach a steady state. An example of such an Ohmic runaway discharge is #62788. The profile of #62788, also taken at $t = 2$ s, is rather peaked. This is one of the profiles already shown in chapter 5 where a profile of runaway diffusion coefficient is derived from radiation profile and evolution. This discharge #62788 has a radiation evolution that shows a flat plateau when $t \gtrsim 4$ s, after an initial rather linearly rising signal.

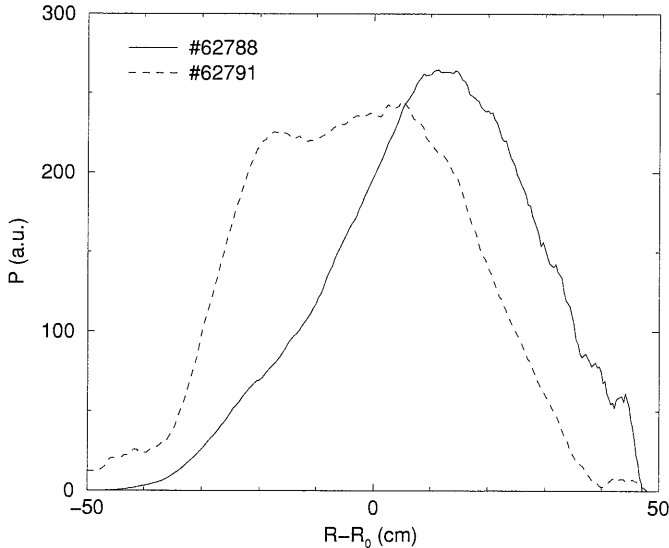


Figure 8.1: Synchrotron radiation profiles at $t = 2$ s for two different discharges. #62788 (see figure 5.4 and 5.6) has a radiation evolution that reaches a steady state at $t = 4$ s, whereas #62791 (see table 6.1 and figure 6.7; the case with largest total input power (NBI) has similar radiation evolution as #62791) has an exponentially rising radiation evolution up to the moment of NBI (at $t = 2.7$ s). The relative shift of the profiles is due to different central plasma positions in the different discharges. In both discharges, $q_a = 3.8$. In #62788 small sawteeth ($\Delta T_e/T_e \approx 10\%$) are present; for #62791, no temperature measurements are available.

8.2.4 Discussion

The exact time at which q_0 rises above unity in the current decay phase can not be derived from the moment of disappearance of sawteeth. The fact that the increase in synchrotron spot is observed after the disappearance of sawteeth, at least does not contradict a possible relation with the disappearance of a barrier near $q = 1$. The observed time scale of the synchrotron spot increase in the current decay phase (0.1 ms) is smaller than the estimated maximum time scale of spot increase after disappearance of transport barrier (500 ms). However, the latter is based on a diffusion coefficient, $D_{r,\text{out}} = 0.1 \text{ m}^2\text{s}^{-1}$, which was rather arbitrary. The value of $D_{r,\text{out}}$ in the barrier model is not very critical. When the observed spot increase

is caused by runaway diffusion, the time scale of 0.1 ms corresponds to a diffusion coefficient $D_r \approx 300 \text{ m}^2\text{s}^{-1}$ which would fit into the model as well.

However, the simultaneous increase in intensity during the spot increase and the stepwise rising ECE signal that is observed after the spot increase, can not be explained only by a loss of electron transport barrier. Moreover, because observations of sudden synchrotron spot increase are done in a steady current flat top phase, the events do not depend on changes in the current, or q profile. These observations make the interpretation of the spot increase as a result of a transport barrier loss not very likely, but definite conclusions can only be drawn after more accurate investigation of the events. In [18], a possible explanation is given based on interaction between runaways and plasma waves. In the next section this phenomenon, together with new observations, is discussed in detail.

The profile of #62791 in figure 8.1 has a shape (top-hat) as was expected when at least one electron transport barrier exists in the plasma. The first and strongest barrier is expected near $q = 1$. The runaway beam radius is approximately $r_{\text{beam}} \approx 15 \text{ cm}$. In a plasma with $q_a = 3.8$, the radius of the $q = 1$ surface is approximately at $r = a/q_a = 12 \text{ cm}$. Outside approximately $r \approx 30 \text{ cm}$, no runaways are observed. This corresponds roughly with the position of the $q = 2$ surface. The barrier hypothesis could explain the rising radiation evolution in the Ohmic phase of #62791. The only possible transport across the barrier, by collisions or electrostatic turbulence ($D_{r,\text{in}} \approx 10^{-3} \text{ m}^2\text{s}^{-1}$ or even less), is small for these high energetic electrons with respect to the diffusion rate outside the barrier. Hardly any runaway electrons are lost and, therefore, the radiation evolution shows an exponential growth.

The peaked profile shape of #62788 leads, according to the above argumentation, to the conclusion that in that discharge, no electron transport barrier is present. The radiation evolution of this discharge, reaching a steady state at $t \approx 4$, is most likely explained by a balance between source of runaways and runaway loss mechanisms. The relative shift of the profiles in figure 8.1 is due to different central positions of the plasma in the different discharges.

The above interpretation of the profiles in terms of an electron transport barrier is rather speculative. The profile and radiation evolution of #62791 can be interpreted in terms of several electron transport barriers between $q = 1$ and $q = 2$. A big difference in plasma conditions up to $t = 2 \text{ s}$, the time of the profiles, could not be recognized between #62788 and #62791. The (possible) formation of barriers in one discharge while in the other no barriers are formed, in spite of similar initial conditions, is a kind of bifurcation that is more often observed in connection with transport barriers [17].

In conclusion, from IR pictures taken during the current decay phase, possible evidence for the existence of an electron transport barrier has been found. However, the observation of the increase in synchrotron radiation spot is accompanied with other phenomena. Most measurements lead to a more consistent picture when they are interpreted as a runaway electron-wave interaction than when they are interpreted in terms of electron transport barriers. The profile measurements show evidence of barriers by means of the typical hat-shape. To give a final judgment on the existence of an electron transport barrier on basis of runaway electron measurements, a much more detailed investigation should be done on radiation profiles.

8.3 Fast pitch angle scattering events

8.3.1 Introduction

In the previous section, observations of a rapid change in synchrotron spot and intensity, presented in [18], were already mentioned. These observations are done during the current decay phase. An example is shown in figure 8.2. A possible explanation for increase in the spot size was given by the loss

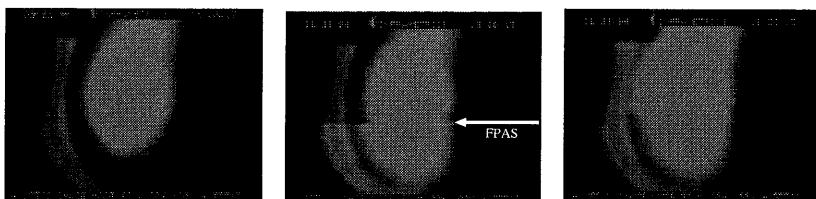


Figure 8.2: *Three subsequent pictures taken with the IR camera showing a fast pitch angle scattering (FPAS) event.*

of an electron transport barrier. Another interpretation of the phenomenon is presented in [18] which leads to a more consistent picture with other simultaneous observations, such as the increase in intensity and the stepwise increasing ECE signal.

The intensity can change by a change in energy W_r , number of runaways N_r or pitch angle θ . Because the short time scale on which this event occurs, it is concluded that the increase in intensity can only be caused by a fast pitch angle scattering (FPAS). The pitch angle increases with a factor of about 1.5.

A possible mechanism to explain an FPAS event, based on interaction of runaways with plasma waves, is discussed in [18]. Starting point is the Parail-Pogutse instability [19] (see also section 2.4) which occurs in the so-called slide-away regime. This regime is characterized by a large suprathermal electron population [20], low density and low loop voltage. These conditions occur for instance during the current and density decay phase of a discharge. If a runaway beam that is being accelerated reaches some critical energy W_{beam} , waves are excited at the anomalous Doppler resonance. Resonance between thermal electrons and these waves lead to a plateau in the distribution function. This flattening of the distribution function causes a broad spectrum of waves to become unstable. These waves isotropize the complete runaway region in energy. After that, the waves are damped. Because the runaways accelerate again and exceed W_{beam} , this whole process repeats itself. This repetitive nature of the instability becomes very clear from ECE measurements. The ECE signals show a stepwise rise until they are saturated.

Among the waves excited in the second stage of the Parail-Pogutse instability, lower hybrid waves are present. These waves can pitch angle scatter the runaway electrons by anomalous Doppler resonance when the runaways have an energy (in MeV) of [18]

$$W_{\text{res}} \approx \frac{70}{(N_{\parallel} - 1)\sqrt{Z_{\text{eff}}n_e}} \quad (8.1)$$

where n_e is expressed in 10^{19} m^{-3} and N_{\parallel} is the parallel refractive index. In TEXTOR-94, typically $N_{\parallel} = 4$, $n_e = 0.5 \times 10^{19} \text{ m}^{-3}$ and $Z_{\text{eff}} = 2$, so $W_{\text{res}} = 23 \text{ MeV}$. This energy is exactly in the range of the electrons observed by synchrotron radiation measurements.

The suggested explanation for an FPAS event is based on the Parail-Pogutse instability, which is of repetitive nature. In the synchrotron radiation signal [18], however, only one single FPAS event per discharge was observed. It was suggested that this is related to the observation in other tokamaks that the Parail-Pogutse instability is strongest at its first occurrence. Another suggestion is that because the density is decreasing during the FPAS event, the resonance between lower hybrid waves and the runaways takes place at a higher energy. On top of that, runaway electrons radiate more strongly after a pitch angle increase and have less energy.

It may be interesting to note that, as is discussed in chapter 2, the Parail-Pogutse instability excludes the presence of high energetic runaway electrons because of the repetitive resonances that lower the energy of the suprathermal electrons. Hence, a fast pitch angle scattering event can only occur, when high energetic runaways are present already before the instability sets in.

Table 8.1: Overview of FPAS event observations in one single IR picture. In all cases, $B_t = 2.2$ T. Error in determination of \bar{n}_e is $\pm 0.05 \times 10^{19} \text{ m}^{-3}$; error in determination of I_p is ± 5 kA.

#	multiple	$I_{p,\text{FPAS}}$ (kA)	$dI_p/dt)_{\text{FPAS}}$ (kA/s)	$\bar{n}_{e,\text{FPAS}}$ ($\times 10^{19} \text{ m}^{-3}$)	$d\bar{n}_e/dt)_{\text{FPAS}}$ ($\times 10^{19} \text{ m}^{-3}\text{s}^{-1}$)
62781	-	350	0	0.60	0
62785	x	350	0	0.50	0
		350	0	0.60	-1.78 (after pellet)
64727	x	300	-163	0.40	0
		217	-163	0.40	0
64728	x	395	-217	0.45	0
		317	-217	0.45	0
66519	-	233	-273	0.40	0
72038	-	161	-644	0.30	0
73206	-	169	-177	0.30	-0.45
73207	-	200	-182	0.30	-0.41

8.3.2 New observations

Several new FPAS event observations occurred in runaway discharges during a variety of experimental programs. These observations are presented below.

The IR camera which is used for the synchrotron measurements is a scanning camera. During a normal runaway discharge, the synchrotron spot covers about 30-60% of the total IR picture. In the current and density decay phase of the discharge, the spot covers less. The chance that an FPAS event is observed during the scanning of the synchrotron spot is related to the amount of coverage of the spot. It is, therefore, not surprising that in all 28 FPAS discharges, only 8 FPAS events are observed during the scanning of the synchrotron spot. In 20 discharges, FPAS events are recognized from a sudden increase from one IR picture to the next. In table 8.1, the 8 FPAS events observed in a single IR picture are listed.

The observations presented in table 8.1 are similar to those made in previous experiments [18]. After the (first) FPAS event, all discharges reach the slide-away regime. This is deduced from the rising ECE signal or, if this signal was not available, from a significant decrease in V_{loop} . In five discharges, the rise in ECE is clearly stepwise. In one discharge, no clear steps can be recognized and in two discharges no ECE signal is available. Often, the rise

in ECE signal is accompanied with spikes on the ECE signal. The neutron signals, when available, show mostly a flattening or even decrease when the discharge goes into the slide-away regime. Sometimes, a peak in the neutron signal appears at the FPAS event.

New is the observation of more FPAS events in a single discharge. Also, it is obvious that the plasma conditions that are needed for the instability to develop can be reached in the flat top phase as well as in current or density decay phase. Nevertheless, an FPAS event shows only up as long as during the occurrence of the Parail-Pogutse instability already high energetic runaways are present. Sometimes, discharges with FPAS events show small modulations of the synchrotron spot before the FPAS event which are a sign for mode activity.

Most of the other FPAS events that are observed from an increase in synchrotron spot from one picture to the next, take place during the current decay phase, just before the discharge ends. After the events, the discharges reach the slide-away regime, which is recognized from a low loop voltage, low density and an increase in ECE. Often spikes are observed on the ECE signals before the increase.

8.3.3 Discussion

The new observations are in agreement with the mechanism for an FPAS event as proposed in [18]. The observations of an FPAS event during the current flat top phase rejects, at least for these events, the interpretation based on the disappearance of an electron transport barrier. The 'observable' interaction between high energetic runaway electrons and waves in the plasma depends on low n_e values according to equation (8.1). The n_e happens to reach sufficiently low values mostly during the n_e decay phase, during which also the current decays. Furthermore, the observation of a multiple pitch angle scattering proves that the FPAS of the runaway beam can be indeed a repetitive instability, as is predicted from the suggested explanation with the Parail-Pogutse instability as starting point. Nevertheless, in most cases the energy density of the lower hybrid waves excited during the second occurrence of the instability is apparently too small to pitch angle scatter the runaways more than once.

It may be interesting for future investigations to note that in the FPAS discharges, often magnetic mode activity is observed. Synchrotron spots are unsteady before and after an FPAS event and often, the discharges result in a runaway snake, when the modes have eventually developed to an island topology in a stochastic background plasma.

References

- [1] Wesson J A, Gill R D, Hugon M, Schüller F C, Snipes J A et al. 1989 *Nucl. Fusion* **29** 641
- [2] Schüller F C 1995 *Plasma Phys. and Contr. Fusion* **37** A135
- [3] Jaspers R, Lopes Cardozo N J, Schüller F C, Finken K H, Grewe T, Mank G 1996 *Nucl. Fusion* **36** 367
- [4] Jaspers R, Pankratov I M, Entrop I, Finken K H 1998 *Proc. of the 25th EPS Conf. on Contr. Fusion and Plasma Physics* Prague B068PR
- [5] Kawano Y et al. 1997 *Proc. of the 24th EPS Conf. on Contr. Fusion and Plasma Physics* Berchtesgaden **21A** Part II 501; Yoshina R, Kondoh T, Neyatani Y, Itami K, Kawano Y, Isei N 1997 *Plasma Phys. Contr. Fusion* **39** 313; Yoshino R, Tokuda S, Kawano Y 1999 *Nucl. Fusion* **39** 151
- [6] Gill R D, Alper B, Edwards A W, Ingesson L C, Johnson M F, Ward D, 'Direct observations of runaway electrons during disruptions in the JET tokamak', submitted to *Nucl. Fusion*
- [7] Joyer P, Martin G 1990 *Proc. of the 17th EPS Conf. on Contr. Fusion and Plasma Heating* Amsterdam **14B** Part I 303
- [8] Putvinski S, Barabaschi P, Fujisawa N, Putvinskaya N, Rosenbluth M N, Wesley J 1997 *Plasma Phys. and Contr. Fusion* **39** 12B B157
- [9] Rosenbluth M N, Putvinskij S V, Parks P B 1997 *Nucl. Fusion* **37** 955
- [10] de Vries P C, Waidmann G, Donné A J H, Schüller F C 1996 *Plasma Phys. and Contr. Fusion* **38** 467
- [11] de Vries P C, Rapp J, Schüller F C, Tokar' M Z 1998 *Phys. Rev. Letters* **80** 3519
- [12] Rapp J, de Vries P C, Schüller F C, Tokar' M Z, Biel W, Jaspers R, Koslowski H R, Krämer-Flecken A, Kreter A, Lehnen M, Pospieszczyk A, Reiser D, Samm U 1999 *Nucl. Fusion* **39** 765
- [13] Pankratov I M, Jaspers R, Finken K H, Entrop I, Mank G 1998 *Nucl. Fusion* **38** 279
- [14] Greenfield C M et al 1997 *Phys. Plasmas* **4** 1596; Mazzucato E et al. 1996 *Phys. Rev. Lett.* **77** 3145

- [15] Lopes Cardozo N J et al. 1997 *Plasma Phys. and Contr. Fusion* **39** B303
- [16] Hogeweyj G M D, Lopes Cardozo N J, de Baar M R, Schilham A M R 1998 *Nucl. Fusion* **38** 1881
- [17] de Baar M N, Beurskens M N A, Hogeweyj G M D, Lopes Cardozo N J 1999 'Tokamak plasmas with dominant electron cyclotron heating; evidence for electron thermal transport barriers', to appear in *Phys. of Plasmas* **6** (december issue)
- [18] Jaspers R J E 1995 *Relativistic runaway electrons in tokamak plasmas* PhD Thesis, Eindhoven University of Technology, The Netherlands
- [19] Parail V V, Pogutse O P 1978 *Nucl. Fusion* **18** 303
- [20] Schokker B C 1996 *Suprathermal electrons in tokamak plasmas* PhD Thesis, Eindhoven University of Technology, The Netherlands

Chapter 9

Evaluation

This thesis presents a study of runaway electron transport in a tokamak plasma. The motivation for this study was the question to what extent magnetic turbulence contributes to the anomalous heat transport observed in tokamak plasmas. In this evaluation, the main experimental results are summarized and the questions formulated in the introduction are addressed. These questions were:

- What is the runaway electron transport under different plasma conditions?
- How are scale size and level of magnetic turbulence derived from the runaway transport measurements?
- What is the contribution of magnetic turbulence to anomalous heat transport?

Runaway transport

By means of synchrotron radiation measurements, the radial transport of runaway electrons is determined under different plasma conditions.

In chapter 5, a radial diffusion coefficient profile for high energy runaways in an Ohmic plasma is derived from measurements of synchrotron radiation profiles. At half radius, $r = a/2$, the runaway diffusion coefficient D_r is found to be $0.002 \text{ m}^2\text{s}^{-1} < D_r < 0.01 \text{ m}^2\text{s}^{-1}$, which corresponds to a runaway confinement time τ_r of $> 3.5 \text{ s}$. For comparison, neoclassical theory estimates a runaway diffusion coefficient of $< 10^{-4} \text{ m}^2\text{s}^{-1}$.

Experimental evidence of the energy dependence of the runaway confinement time τ_r is presented in chapter 6. In discharges with auxiliary heating, the intensity of the synchrotron radiation shows a decline after the heating

is switched on. The runaway confinement is deteriorated by the auxiliary heating power. For confinement of heat and thermal electrons, similar observations have been made, as well as for 1 MeV runaway electrons in the plasma edge in ASDEX [1]. In TEXTOR-94, the decline of the radiation is, however, observed only after a delay of 0.1 – 1 s, depending on the heating power. The delay can be explained by assuming that the deterioration of runaway confinement is restricted to an energy range well below 30 MeV, i.e. the energy of the observed runaways. The loss of runaways at lower energy appears only later as a reduced number of observable runaways at high energy. With increasing heating power, the energy range of runaway confinement deterioration increases to higher energies resulting in a shorter delay in radiation decline.

In chapter 7, the confinement of runaway electrons is discussed in a plasma with large magnetic islands. The runaways are confined in drift islands of similar topology as the magnetic islands that consist of perfect flux surfaces. The radial runaway diffusion coefficient inside an island is at the most $0.01 \text{ m}^2\text{s}^{-1}$. Outside a drift island, $D_r = 1 - 300 \text{ m}^2\text{s}^{-1}$. The drift island is shifted from the magnetic island because of magnetic field gradient and curvature. The well confined runaways inside a drift island are, therefore, partly moving in a region where the magnetic field is stochastic.

Magnetic turbulence

The energy dependence of the runaway confinement is explained by the averaging effect that the drift orbit shift has on the effect of magnetic turbulence on the runaway transport. A runaway experiences the perturbations of a single magnetic mode of various phase on its orbit during one transit time, which causes the averaging. Furthermore, when the orbit shift is larger than the typical scale size of the magnetic perturbation, it 'feels' the mode only a fraction of its transit period, which further reduces the effect of magnetic turbulence.

The typical drift orbit shift of the observable runaways is in the order of centimeters. Because the runaway electrons are so well confined in Ohmic plasmas, the typical size of the average magnetic mode in an Ohmic plasma has to be significantly smaller than the drift orbit shift. The detected IR signal of runaways at high energy reflects, however, the acceleration history of these runaways. Hence, the synchrotron radiation measurements contain information on runaways during their complete energy development from 100 keV to 30 MeV. These energies correspond to orbit shifts in the range 0.02 – 6 cm.

In a model by Mynick and Strachan [2], the ratio between runaway con-

finement time for the case including drift orbit averaging effects and the runaway confinement time without these effects is expressed as function of the ratio between drift orbit shift (d) and average mode width (δ) of the perturbation. Because the orbit shift d is proportional to electron energy, the model in [2] gives an energy dependent confinement time with average mode width δ as free parameter. Comparison between measured radiation signals and simulated radiation signals based on that energy dependent confinement time results in estimates for the typical scale size of magnetic perturbations. In Ohmic plasmas, $\delta < 0.5$ cm. In plasmas with auxiliary heating, δ increases with increasing power. For example, with 0.6 MW NBI, $\delta \approx 4.2$ cm. An increase in mode width up to ~ 4 cm corresponds with a reduction in confinement time for high energetic runaways from $\tau_r > 1$ s in an Ohmic plasma to $\tau_r \sim 100$ ms in an heated plasma. This corresponds to an approximate diffusion coefficient of high energetic electrons of $D_r \sim 1 \text{ m}^2\text{s}^{-1}$ in an additionally heated plasma.

The size of the perturbing field can be estimated when the average scale size of the magnetic modes is interpreted as the width of chains of islands. Then, in Ohmic plasmas it is found $\tilde{B}/B \sim 2 \times 10^{-5}$, in a plasma with 0.6 MW heating power, $\tilde{B}/B \sim 1 \times 10^{-3}$. The estimates are valid at $r/a = 0.3$. These estimates are rather uncertain because of the assumptions needed to relate the scale size to the width of chains of islands. Moreover, a value of $\tilde{B}/B \sim 10^{-3}$ seems to be overestimated: in chapter 7, a fluctuating field of $\tilde{B} \sim 10^{-4}$ T was estimated to cause large magnetic islands, that eventually lead to a disruption of the plasma.

Other models are investigated to find a more accurate estimate of \tilde{B}/B . A model by Myra and Catto [3] also calculates the transport reducing effect of the electron orbit shift. The starting point is the quasilinear collisionless radial electron diffusion coefficient due to magnetic perturbations given by [4], $D_e = \pi q R_0 v_{||} (\tilde{B}/B)^2$, which is multiplied by a drift modification factor Υ . This factor is given as a function of the ratio between drift orbit shift d and magnetic mode width δ . It decreases with increasing ratio. In the model, different poloidal structures of the magnetic turbulence are considered to calculate the transport reducing factor Υ . Here, we only consider the results based on poloidally uniform magnetic turbulence, because it fits best to our picture of magnetic turbulence.

Because both Υ and the radial mode width δ are unknown, \tilde{B}/B can not be estimated from the model by Myra and Catto [3] alone. Hence, the mode widths that follow from comparison of experiment and simulations based on the model by Mynick and Strachan [2] are used to give an estimate of \tilde{B}/B . In Ohmic plasmas, $\delta < 0.5$ cm. The diffusion coefficient of high energetic runaways (orbit shift of ~ 6 cm) in an Ohmic plasma is $0.002 \text{ m}^2\text{s}^{-1} <$

$D_r < 0.01 \text{ m}^2\text{s}^{-1}$. This leads to an estimate (with $q = 1$ and $v_{\parallel} = c$) $5 \times 10^{-6} < \tilde{B}/B < 1 \times 10^{-5}$ in Ohmic plasmas. In a plasma with 0.6 MW NBI heating, $\delta \approx 4.2 \text{ cm}$. It was derived above that in a additionally heated plasma $D_r \sim 1 \text{ m}^2\text{s}^{-1}$. Then, the magnetic turbulence level is approximately $\tilde{B}/B \sim 3 \times 10^{-5}$.

Numerical calculations of magnetic field line trajectories by de Rover et al. [5] showed that, first, field lines in a chaotic field do not make a Gaussian random walk as is assumed in the derivation of the quasilinear collisionless diffusion coefficient by [4] (and therefore also in the calculation by [3]). Secondly, magnetic shear can not be neglected in studies of transport in chaotic field as is commonly done. A magnetic field that is perturbed by small current filaments, shows for levels of $\tilde{B}/B \sim 2 \times 10^{-4}$ chains of small islands with a width of approximately 0.3 cm mixed with regions of good magnetic surfaces. When $\tilde{B}/B \sim 10^{-3}$, the average displacement of magnetic field lines has increased, there are hardly any good magnetic surfaces and the islands that can be recognized have widths of approximately 1.5 cm. Calculation of test particle transport in these stochastic magnetic fields yields a diffusivity χ that is much smaller than the measured χ . Therefore, different decorrelation mechanisms (time dependence of magnetic fluctuations, electrostatic fluctuations) of particles from the magnetic field lines must be included in the model if magnetic turbulence is to cause the thermal transport anomaly. Unfortunately, in this test particle transport model of de Rover et al. [5], the averaging of the drift orbit shift on the effect of magnetic turbulence on transport has not been taken into account. Hence, a direct estimate of magnetic turbulence level or scale size based on runaway transport measurements is not possible. What the model predicts for thermal transport is discussed in the next subsection.

Table 9.1 gives an overview of the estimates of scale size and level of magnetic turbulence according to the different models as discussed in this section. For comparison, measurements and estimates of core magnetic turbulence in other tokamaks are mentioned. Zou et al. [6] estimate $\tilde{B}/B \sim 3 - 6 \times 10^{-5}$ from cross polarization scattering measurements in Tore Supra. In [7], vertical ECE measurements lead to an estimate $\tilde{B}/B \sim 4 \times 10^{-5}$ in electron cyclotron heated plasmas in TEXT-U. In JET [8], the determination of runaway diffusion by fast electron bremsstrahlung measurements correspond to levels $8 \times 10^{-6} < \tilde{B}/B < 4 \times 10^{-5}$ in Ohmic plasmas (based on the model of [3]). Correlation reflectometer measurements in JET [9] showed a radial extent of density structures of less than 0.5 cm under Ohmic conditions. For 15 MW of NBI power, the radial extent was typically at least 3 cm.

Table 9.1: Overview of results on scale size and level of magnetic turbulence according to different models. Note that the results for de Rover et al. are numerically calculated and not directly connected to Ohmic or heated plasmas, although they are listed that way. (MS denotes Mynick and Strachan.)

models	Ω		NBI	
	δ (cm)	\tilde{B}/B	δ (cm)	\tilde{B}/B
Mynick and Strachan [2]	< 0.5	2×10^{-5}	4.2	1×10^{-3}
Myra and Catto [3]	(MS)	$5 \times 10^{-6} - 1 \times 10^{-5}$	(MS)	3×10^{-5}
de Rover et al. [5]	0.3	2×10^{-4}	1.5	10^{-3}

Anomalous heat transport

The estimates of scale size δ of magnetic turbulence according to Mynick and Strachan [2] are based on a calculation of transport reduction normalized to the case of runaway transport without any drift orbit averaging effects. As in [2], this 'driftless' runaway confinement is equated to thermal electron transport with a correction factor for velocity in our simulations. First, it should be noted that this calibration is rather uncertain. The calibration factor is, however, not a very sensitive parameter: when it varies one order of magnitude, the estimated δ changes only a factor two. Secondly, because of this calibration to thermal confinement, an estimate of the contribution of magnetic turbulence to this thermal confinement would only result in that value we put into the model.

According to Myra and Catto [3] a value of $\tilde{B}/B < 10^{-5}$ is found in Ohmic plasmas. When it is assumed that for thermal confinement the drift orbit averaging can be neglected (i.e. the drift modification factor $\Upsilon \approx 1$), the thermal electron diffusivity is $\chi_e < 0.01 \text{ m}^2\text{s}^{-1}$. In TEXTOR-94, $\chi_e \sim 1 \text{ m}^2\text{s}^{-1}$ is measured in Ohmic heated plasmas. These values imply that less than 1% of the anomalous thermal transport is caused by magnetic turbulence in an Ohmic plasma. In an additionally heated plasma, a value of $\tilde{B}/B \sim 3 \times 10^{-5}$ results in $\chi_e \sim 0.05 \text{ m}^2\text{s}^{-1}$. Because the heat diffusivity is about a factor of two to three larger in heated plasmas relative to Ohmic plasmas, the contribution of magnetic turbulence during auxiliary heating to thermal transport increases to a few percent.

From Mynick and Strachan [2], a scale size of magnetic turbulence of

< 0.5 cm was derived in Ohmic plasmas. According to de Rover et al. [5] (test particle transport in stochastic magnetic fields), this corresponds with a magnetic turbulence level of approximately $\tilde{B}/B \sim 10^{-4}$. The heat diffusivity (including decorrelation effects) is estimated $\chi_e \sim 0.01 \text{ m}^2\text{s}^{-1}$. During auxiliary heating, the scale size of magnetic turbulence increases to several cm, which corresponds to de Rover et al. to levels of $\tilde{B}/B > 10^{-3}$. This results in $\chi_e > 2 \text{ m}^2\text{s}^{-1}$ during heating. These results imply that the contribution of magnetic turbulence to anomalous thermal transport increases from only 1% in Ohmic plasmas to 100% in additionally heated plasmas.

As already mentioned, a value of $\tilde{B}/B \sim 10^{-3}$ can cause large magnetic islands and can even lead to a plasma disruption (see chapter 7). It is not very likely that such a high value occurs in steady state plasmas (see also estimates of \tilde{B}/B in other tokamaks mentioned above). This high level of turbulence was derived from an average mode width of approximately 4 cm. In our calculations, we calibrated the confinement reduction curve to a thermal confinement of 20 ms. This corresponds roughly to a χ_e of same order of magnitude as is measured in TEXTOR-94. This calibration implies, therefore, that in that case the measured thermal transport is completely determined by magnetic turbulence. When in an Ohmic plasma, magnetic turbulence is only contributing to χ_e for 10% or even less, the calibration factor (i.e. the value of thermal confinement) should have been at least one order of magnitude larger than we took. The estimated mode width δ would then be two times smaller. In an Ohmic plasma, it is then derived $\delta < 0.3$ cm. In heated plasmas, $\delta \approx 2$ cm. Note that the values of δ now compare well with the values found according to de Rover et al. where numerically calculations were made of perturbed magnetic fields for levels $\tilde{B}/B \sim 1 - 10 \times 10^{-4}$. So, in comparison with other models, the possible overestimation of $\tilde{B}/B \sim 10^{-3}$ in the model of Mynick and Strachan gives a clue about the correctness of the calibration, i.e. of the input value to what extent magnetic turbulence contributes to thermal transport. More precise modeling of test particle transport (e.g. including drift orbit averaging effects in the model by de Rover et al.) in perturbed magnetic fields can give more accurate estimates of the scale size and level of magnetic turbulence.

In conclusion, it is observed that during auxiliary heating the mode width δ increases, provided that our analysis revealing δ is correct. Corresponding levels of magnetic turbulence increase as well. The influence of magnetic turbulence to the electron heat flux during auxiliary heating increases. In Ohmic plasmas, however, the magnetic field fluctuations hardly contribute to the electron heat flux. Other transport mechanisms are needed to explain the measured heat diffusivity. Turbulent fluctuations of the electric field is one of the options. The question arises, when thermal transport in an Ohmic plasma

is determined by electrostatic fluctuations, what is the contribution of these fluctuations to runaway transport? Recall that one of the main assumptions in all models is that runaway transport is dominated by magnetic turbulence. How reasonable is that assumption?

The transport due to electrostatic turbulence is proportional to the inverse of electron velocity. When the measured Ohmic heat diffusivity ($\chi_e \sim 1 \text{ m}^2\text{s}^{-1}$) is determined by electrostatic fluctuations, the contribution to runaway diffusion is at least a factor $v_r/v_e \approx 30$ less. In that case, $D_r \sim 0.03 \text{ m}^2\text{s}^{-1}$. This estimate is of same order of magnitude as the measured runaway diffusion coefficient. Hence, electrostatic turbulence should not be neglected in a study of runaway confinement in Ohmic plasmas. During auxiliary heating, the runaway diffusion coefficient due to electrostatic turbulence is approximately $D_r \sim 0.1 \text{ m}^2\text{s}^{-1}$ (χ_e enhances with a factor two to three during heating). This is only 10% of the estimated runaway diffusion coefficient during auxiliary heating ($D_r \sim 1 \text{ m}^2\text{s}^{-1}$). Magnetic turbulence enhances the estimated runaway transport coefficient due to electrostatic turbulence during heating. The importance of magnetic turbulence during heating follows also from the radiation signal evolutions that are reproduced in simulations using an energy dependent confinement. This energy dependence is explained by an averaging effect that probably only works out in a magnetic turbulence picture. It is, therefore, concluded that the contribution of magnetic turbulence to the heat diffusivity and runaway transport increases in auxiliary heated plasmas. In Ohmic plasmas, the magnetic turbulence does not contribute significantly to heat transport.

References

- [1] Kwon O J, Diamond P H, Wagner F, Fussmann G, ASDEX and NI teams 1988 *Nucl. Fusion* **28** 1931
- [2] Mynick H E, Strachan J D 1981 *Phys. Fluids* **24** 695
- [3] Myra J R, Catto P J 1992 *Phys. Fluids B* **4** 176
- [4] Rechester A B, Rosenbluth M N 1978 *Phys. Rev. Lett.* **40** 38
- [5] de Rover M, Schilham A M R, Montvai A, Lopes Cardozo N J 1999 *Phys. Plasmas* **6** 2443
- [6] Zou X L, Colas L, Paume M, Chareau J M, Laurent L, Devynck P, Grésillon D 1995 *Phys. Rev. Lett.* **75** 1090
- [7] Giruzzi G, Steimle R F, Roberts D R, Sing D, Wootton A J 1996 *Plasma Phys. and Contr. Fusion* **38** 1593
- [8] Esposito B, Martin-Solis R, van Belle P, Jarvis O N, Marcus F M, Sadler G, Fischer F, Froissard P, Adams J M, Cecil E, Watkins N 1996 *Plasma Phys. and Contr. Fusion* **38** 2035
- [9] Costley A E, Cripwell P, Fukuda T 1994 *Proc. of the 21st EPS Conf. of Contr. Fusion and Plasma Physics* (Innsbruck) Part I 199

Summary

Nuclear fusion is one of the candidates of future energy supply. It is the process in which two light nuclei melt together under release of an enormous amount of energy. To overcome the repelling forces of the two positively charged nuclei, fusion only takes place at very high temperature or pressure. In a thermonuclear reactor, a very hot, completely ionized gas is confined in a magnetic field configuration to avoid wall contact. The presently most successful type of reactor is the tokamak. In a tokamak, the confining magnetic field is produced by external toroidal coils and by an induced plasma current. The magnetic field configuration consists of toroidal nested surfaces spanned by the helical magnetic field lines. Radial transport across the surfaces is caused by collisions and is expected to be very small.

One of the major problems in tokamak physics is, however, the anomalous radial heat transport via electrons and ions. When fusion should serve as future energy source and fusion reactors should be as efficient and compact as possible, it is important to understand this anomalous transport. Anomalous transport is caused by turbulent fluctuations of the electric or the magnetic field. Because already very small magnetic field fluctuations, with respect to the confining field, can enhance the heat transport considerably, it is difficult to diagnose especially this magnetic turbulence. Hence, the question how much magnetic turbulence contributes to the anomalous transport, is still an open one. It is this question that is investigated in this thesis.

One way of probing the magnetic turbulence in a tokamak plasma is the investigation of transport of very fast electrons. The electric field that drives the plasma current, accelerates electrons. Part of the electron population has such a high velocity that the drag force due to collisions is too small to balance the acceleration. These 'runaway' electrons are effectively accelerated. They seldomly collide and are completely decoupled from the ions. Their radial transport is expected to be dominated by the magnetic field perturbations.

In the TEXTOR-94 tokamak, runaway electrons are accelerated up to energies of 30 MeV. These electrons emit synchrotron radiation in the infrared wavelength range. The radiation is emitted in a very narrow cone because

of the high (relativistic) energy. In TEXTOR-94, the runaway electrons are observed with an infrared camera that is positioned in the equatorial plane and views tangentially into the tokamak into direction of electron approach. The synchrotron radiation is, hence, detected in a poloidal projection. The detected intensity is a measure of number of runaway electrons. From radiation evolutions and profile measurements, the runaway electron transport properties can be derived.

In an Ohmic plasma, i.e. a plasma that is only heated by the plasma current, high energetic runaway electrons are confined very well. The typical confinement time is more than a few seconds. Also, in a plasma where large regions of stochastic magnetic field lines are formed but in which large magnetic islands consisting of good surfaces survive, the transport of runaways is very small inside the islands. In the stochastic regions, however, the runaway transport is high. In those perturbed plasmas, the runaway electrons are only confined in the islands.

In plasmas where auxiliary heating is applied, by means of injection of a neutral beam or waves resonant with the ion cyclotron motion around the magnetic field lines, the runaway confinement shows a degradation. It has been shown in this thesis that this degradation depends on the runaway energy. Lower energetic runaways are suffering from larger losses than the higher energetic runaways during the auxiliary heating.

The energy dependent deterioration of runaway confinement during heating can be explained by the averaging effect of the drift orbit shift on the runaway transport due to magnetic turbulence. Electron orbits are shifted from the magnetic surface because of the magnetic field gradient and curvature. This shift increases with runaway energy. The larger the drift orbit displacement is, compared with the scale size of the magnetic turbulence, the less the runaway electron performing that drift orbit is sensitive to the magnetic fluctuations with that typical scale size. An increasing amount of auxiliary heating power results in an increasing scale size of magnetic turbulence. This causes a runaway loss in an increasing part of the low energy side in the total runaway energy range. The loss of lower energetic runaway electrons during the heating finally results in a decaying radiation signal after a delay corresponding to the time needed for the energy gap to 'show up' in the synchrotron measurements. This explanation of the energy dependent deterioration of runaway confinement by the drift orbit averaging effect requires that the loss of runaway is mainly caused by magnetic turbulence.

When runaway electrons are born in TEXTOR-94, they have an energy of about 100 keV which corresponds to a drift orbit shift of 0.02 cm. Runaway electrons of 30 MeV observed with the infrared camera are shifted even up to 6 cm. This implies that the typical scale size of magnetic turbulence

must be in the range from 0.02 cm until 6 cm. A model by Mynick and Strachan in which the effect of the drift orbit shift on runaway transport is numerically calculated allows a more accurate estimate of the average scale size as function of input power. In an Ohmic plasma, this size is less than 0.5 cm, while in a plasma with auxiliary heating, it is enhanced up to approximately several centimeters. The exact calibration of the numerically determined relation between the effect of the drift orbit shift and the runaway energy is uncertain. Therefore, the estimated scale size can vary a factor of two.

The strength of the perturbing magnetic fields can be estimated from the typical scale size of magnetic turbulence. In Ohmic plasmas, the ratio between the perturbing fields and the confining magnetic field is $10^{-6} - 10^{-5}$ depending on the model that is used to derive this ratio. In additionally heated plasmas, the perturbing fields increase to one thousandth of the toroidal magnetic field strength.

Now, the contribution of magnetic turbulence to the heat transport, χ_e , can be investigated. In Ohmic plasmas, $\chi_e \sim 1 \text{ m}^2\text{s}^{-1}$ is measured in TEXTOR-94. Perturbing fields that are $10^{-6} - 10^{-5}$ times the magnetic field can cause a transport that is approximately 1% of the measured heat transport. In additionally heated plasmas, the measured heat transport is a factor two to three larger than the value that is measured in Ohmic plasmas. A magnetic turbulence level of $10^{-4} - 10^{-3}$ can induce a transport that is up to several tens of percents of the measured χ_e .

With the estimation of the level of magnetic turbulence, the contribution of magnetic turbulence to the anomalous heat transport via electrons can be investigated. We find that in Ohmic plasmas, the contribution of magnetic turbulence to the heat transport in tokamak plasmas can be neglected. When auxiliary heating is applied, the magnetic turbulence is enhanced and its contribution to anomalous heat transport becomes more significant.

Samenvatting

Kernfusie is een van de kandidaten voor de levering van energie in de toekomst. Het is het proces waarbij twee lichte atoomkernen samensmelten en waarbij een enorme hoeveelheid energie vrijkomt. Omdat de afstotende kracht tussen twee positief geladen kernen moet worden overwonnen, fuseren twee kernen alleen bij zeer hoge temperatuur of onder zeer hoge druk. In een thermonucleaire reactor wordt een zeer heet, geheel geïoniseerd gas opgesloten in een magnetisch veld om contact met de reactorwand te voorkomen. In een tokamak wordt het opsluitende magneetveld deels opgewekt door externe toroidale spoelen en deels door een plasmastroom. De topologie van het magneetveld bestaat uit geneste toroidale oppervlakken die opgespannen worden door de helische magneetveldlijnen. Radiaal transport, dat wil zeggen transport van het ene naar het volgende oppervlak, wordt in deze topologie veroorzaakt door botsingen en is naar verwachting erg klein.

Een van de grootste problemen op het gebied van de tokamakfysica is echter het hoge (anomale) warmtetransport via elektronen en ionen in radiale richting. Als kernfusie als toekomstige energiebron gebruikt gaat worden en fusiereactoren zo efficiënt en compact mogelijk moeten zijn, is het van belang deze anomale warmtegeleiding te begrijpen. Anomaal transport kan worden veroorzaakt door turbulente fluctuaties van het elektrische of magnetische veld. Magneetveldverstoringen die erg klein zijn ten opzichte van het opsluitende magneetveld, kunnen de warmtegeleiding al flink vergroten. Het is daarom moeilijk deze magnetische turbulentie te meten. De vraag in hoeverre magnetische turbulentie aan warmtetransport bijdraagt is dan ook nog steeds niet beantwoord. Het is deze vraag die in dit proefschrift wordt behandeld.

Een manier om de magnetische turbulentie in een tokamakplasma te meten is het bestuderen van het transport van zeer snelle elektronen. Het elektrische veld dat de plasmastroom drijft, versnelt elektronen. Een deel van de elektronenpopulatie heeft een zodanig hoge snelheid, dat de wrijvingskracht ten gevolge van botsingen te klein is om deze versnelling voldoende tegen te gaan. Deze runaway-elektronen worden effectief versneld. Ze botsen

zelden en zijn geheel losgekoppeld van de ionen. Het wordt aangenomen dat hun transport in radiale richting wordt gedomineerd door de verstoringen in het magneetveld.

In de TEXTOR-94 tokamak worden runaway-elektronen versneld tot energieën van 30 MeV. Deze elektronen stralen synchrotronstraling in het infrarode golflengtegebied uit. Door de hoge (relativistische) energie wordt de straling in een smal kegeltje uitgezonden. De runaway-elektronen worden in TEXTOR-94 waargenomen met een infraroodcamera die in het equatoriale vlak is opgesteld en die langs de raaklijn aan de magnetische as de tokamak in kijkt, in de richting waar de elektronen vandaan komen. De synchrotronstraling wordt zo in poloidale projectie gedetecteerd. De waargenomen stralingsintensiteit is een maat voor het aantal runaway-elektronen. Van de tijdsverloopmetingen en profielmetingen van de straling kunnen de transporteigenschappen van runaway-elektronen afgeleid worden.

In een Ohms plasma, dat wil zeggen een plasma dat slechts door de plasmastroom wordt verhit, zijn runaway-elektronen met hoge energie goed opgesloten. De typische opsluittijd is meer dan enkele seconden. Ook in een plasma waarin door grote magneetveldverstoringen grote gebieden met stochastische veldlijnen zijn ontstaan maar waarin grote magnetische eilanden die bestaan uit goede oppervlakken zijn blijven bestaan, is het transport van runaways in de eilanden erg laag. Het runaway-transport in de stochastische gebieden is daarentegen hoog. Runaway-elektronen blijven in dergelijke verstoorde plasma's alleen gevangen in de eilanden.

In plasma's waar extra verhitting wordt toegepast, bijvoorbeeld door het inschieten van een bundel neutrale deeltjes of door het toedienen van golven die resonant zijn met de gyratiebeweging van de ionen om de magneetveldlijnen, vertoont de runaway-opsluittijd een verslechtering. Het blijkt uit de in dit proefschrift beschreven experimenten, dat deze verslechtering afhankelijk is van de runaway-energie. Runaways met lagere energie ondervinden tijdens de extra verhitting een groter verlies dan de runaways met hogere energie.

De energie-afhankelijke verslechtering van de runaway-opsluittijd kan verklaard worden door het middelende effect dat de verschuiving, die de oppervlakken gevormd door de helische deeltjesbanen ondervinden, op het runaway-transport door magnetische turbulentie heeft. Banen van elektronen zijn verschoven ten opzichte van het magneetveldoppervlak door de gradient en de kromming in het magneetveld. Deze verschuiving neemt toe als de elektronen grotere energie hebben. Hoe groter de verschuiving is in vergelijking met de typische schaallengte van magnetische turbulentie, des te minder de runaways die zich op dat verschoven oppervlak bevinden, gevoelig zijn voor de magnetische verstoring. Een toenemende hoeveelheid extra verhitting resulteert in een grotere schaallengte van de magnetische turbulen-

tie. Dit veroorzaakt een verlies van runaways in een toenemend gedeelte aan de kant van de lage energie in het gehele runaway-energiebereik. Het verlies van runaways met lagere energie tijdens verhitting geeft uiteindelijk een afvallend stralingssignaal na een vertraging die overeenkomt met de tijd die nodig is voor het 'energiegat' om in de synchrotronmetingen gezien te worden. Deze verklaring van de energie-afhankelijke verslechtering van de runaway-opsluittijd door dit middelende effect van de verschuiving van de baanoppervlakken vereist dat het verlies van runaways voornamelijk door magnetische turbulentie wordt veroorzaakt.

Als runaway-elektronen ontstaan in TEXTOR-94, hebben ze een energie van ongeveer 100 keV. Deze energie komt overeen met een verschuiving van 0.02 cm. Runaway-elektronen met een energie van 30 MeV die worden waargenomen met de infraroodcamera zijn zelfs tot 6 cm verschoven. Dat wil zeggen dat de typische schaallengte van magnetische turbulentie in het bereik van 0.02 cm tot 6 cm moet liggen. Een model van Mynick en Strachan waar het effect van de verschuiving op het transport van runaways numeriek is berekend, geeft een preciezere afschatting van de schaallengte als functie van het toegediende verhittingsvermogen. In een Ohms plasma is deze lengte minder dan 0.5 cm, terwijl in een plasma met extra verhitting deze lengte is toegenomen tot enkele centimeters. De precieze calibratie van het numeriek bepaalde verband tussen het effect van verschuiving op transport en de runaway-energie is onzeker, Daarom kan de geschatte waarde voor de schaallengte een factor twee variëren.

De sterkte van het versturende magneetveld kan worden afgeleid van de typische schaallengte van de magnetische turbulentie. In Ohmse plasma's is de verhouding tussen de versturende magneetvelden en het opsluitende magneetveld $10^{-6} - 10^{-5}$, afhankelijk van welk model wordt genomen om deze verhouding te bepalen. In de plasma's met extra verhitting nemen de versturende magneetvelden toe tot maximaal een duizendste van de sterkte van het opsluitende veld.

Met deze bepaling van de grootte van de magneetveldverstoringen kan het aandeel van magnetische turbulentie aan het anomale warmtetransport via elektronen worden onderzocht. We vinden dan, dat de bijdrage van magnetische turbulentie aan het warmtetransport verwaarloosd kan worden in Ohmse plasma's. Als extra verhitting wordt toegepast, neemt de magnetische turbulentie toe en haar bijdrage aan het anomale warmtetransport wordt significanter.

Dankwoord

Op een van de laatste bladzijden wil ik graag iedereen bedanken die op welke wijze dan ook heeft bijgedragen aan de totstandkoming van dit proefschrift.

Ten eerste mijn eerste promotor, Niek Lopes Cardozo. Van Niek heb ik veel geleerd over de plasmafysica, een heel nieuw vakgebied voor mij toen ik als oio op Rijnhuizen begon. Zijn enthousiasme werkte vaak aanstekelijk en ik wil hem bedanken voor de motiverende discussies tijdens zijn bezoeken aan Jülich of de mijne aan Rijnhuizen. In Jülich kon ik altijd bij Roger terecht met al mijn vragen over runaways en aanverwante zaken. Ik bedank hem ook voor zijn hulp bij al het experimenteerwerk. Auch danke ich Dr. Finken für die Betreuung in Jülich und für seine Hilfe bei der Diskussion der Ergebnisse. Mijn tweede promotor, Chris Schüller, bedank ik voor die te sporadische discussies over voornamelijk disrupties en de (non)generatie van runaway-elektronen daarbij. Weiterhin bin ich Günter Mank, Thomas Denner und Bert Hiller zum Dank verpflichtet für ihre Hilfe bei der Vorbereitung und dem Durchführen von Runaway-Experimenten, vor allem am Anfang meiner Arbeit in Jülich. Tenslotte wil ik de leden van de leescommissie, Niek, Chris, Roger en Leon Kamp, bedanken voor hun suggesties ter verbetering van dit proefschrift. Auch Dr. Finken danke ich für seine Hinweise zur Verbesserung meiner Doktorarbeit.

De eerste paar maanden van mijn onderzoekstijd op Rijnhuizen en later de bezoeken aan Rijnhuizen waren altijd weer prettig door het even (bij)kletsen met Marco, Marc, Jos en Frank. Die Zeit in Jülich habe ich als angenehm empfunden, nicht zuletzt dank vielen der Doktoranden am IPP: Mario, Joachim, Stefan, Mathias, Peter, Jörg, Thomas, Leon und allen übrigen DIPPs. Kon je in mijn begintijd het aantal Nederlanders in het IPP nog op een hand tellen, later kwam daar behoorlijk verandering door de komst van Ben, Rob, Tony, Nils, Jaco, Victor, Egbert, Fred, Marlies, Hans en alle andere TECcers.

Wat meer op de afstand, maar zeker niet minder belangrijk voor het uiteindelijke resultaat, waren vrienden en familie. Karen wil ik met name bedanken voor haar hulp bij het maken van de kaft. Verder bedank ik al diegenen die me hebben gesteund, vooral tijdens de dipjes en de laatste loodjes, en die hebben gezorgd voor de nodige afleiding buiten het werk om.

Curriculum vitae

Ik ben geboren op 21 juli 1970 te Dordrecht. Mijn VWO diploma heb ik gehaald in 1988, aan het Drachtster Lyceum te Drachten. Direct daarna ben ik natuurkunde gaan studeren aan de Rijksuniversiteit in Groningen. Mijn afstudeerwerk betrof een theoretisch onderzoek naar een oplossinggenererende transformatie voor een gemodificeerde Einstein-vergelijking. In juni 1994 ben ik afgestudeerd. Op 1 januari 1995 ben ik begonnen aan mijn promotie-onderzoek bij het FOM-instituut voor plasmafysica Rijnhuizen in Nieuwegein. Na een korte kennismaking met de plasmafysica ben ik verhuisd naar Jülich alwaar ik mijn onderzoek naar de generatie en transporteigenschappen van runaway elektronen in de TEXTOR-94 tokamak heb verricht. De resultaten van dat onderzoek staan beschreven in dit proefschrift.

Stellingen

behorende bij het proefschrift

Confinement of relativistic runaway
electrons in tokamak plasmas

Ingeborg Entrop

Eindhoven, 20 december 1999

1. In een tokamakplasma wordt een warmtegeleiding gemeten die groter is dan de theorieën voorspellen. Dit kan worden veroorzaakt door verstoringen in het magneetveld. De ruimtelijke uitgebreidheid van deze verstoringen kan worden bepaald door het transport van relativistische 'runaway' elektronen te bestuderen.

Dit proefschrift, hoofdstuk 6

2. In een tokamakplasma dat slechts door de plasmastroom wordt verhit, is de bijdrage van magnetische turbulentie aan de warmtegeleiding klein. Deze bijdrage wordt echter heel belangrijk als het plasma wordt verhit door middel van het inschieten van een bundel neutrale deeltjes.

Dit proefschrift, hoofdstuk 5, 6 en 9

3. Een manier om brandstof aan een fusieplasma toe te dienen is het inschieten van ijsbolletjes van waterstof. De ongunstige netto brandstofinjectie in plasma's met een grote populatie van niet-thermische deeltjes wordt vaak toegeschreven aan het onvermogen van het ijsbolletje deze plasma's binnen te dringen. Een net zo belangrijke oorzaak is echter dat de zojuist gedeponeerde brandstof meteen weer met grote snelheid het plasma uit wordt gedreven.

4. In een tokamak kan het transport van deeltjes worden onderdrukt door een gradient in de poloidale stroomsnelheid die wordt aangedreven door de combinatie van een radiaal elektrisch veld en het magneetveld. Hoe groter het magneetveld is, hoe groter de gradient moet zijn om het transport in gelijke mate te onderdrukken.

5. De effectieve actie die de dynamica van een 'string' beschrijft, is, in laagste orde van de stringdimensie, invariant onder de zgn. dualiteitstransformatie. Deze transformatie kan daarom gebruikt worden om nieuwe oplossingen van de bewegingsvergelijkingen die uit de effectieve actie in laagste orde volgen, te vinden.

6. Het is essentieel dat de voorziene calibratieprocedure zijn neerslag vindt in het ontwerp van nieuwe meetapparatuur.
7. Het feit dat de restauratie van Leonardo da Vinci's 'Laatste Avondmaal' in de Santa Maria delle Grazie kerk te Milaan mede door toepassing van röntgenfluorescentie-analyse op monsters van het schilderij mogelijk was, illustreert hoe belangrijk fysisch onderzoek is voor het behoud van cultuurgoed.
B.J.Gonsior, Phys. Blätter 55 (1999) nr.9, p.61

8. Zij P een polynoom van graad n , D de differentie-operator gedefinieerd door $DP(x) = P(x) - P(x - 1)$ en $|a| < 1$, dan geldt

$$\sum_{k=0}^{\infty} P(k)a^k = \sum_{k=0}^n \frac{(D^k P)(-1)}{(1-a)^{k+1}}.$$

9. Bij het go-spel is het spelen op goede vorm een manier om het uitrekenen van lange zettenreeksen te vermijden.
10. Na de succesvolle introductie in Nederland van Valentijnsdag en het Halloweenfeest zal het vieren van de '4th of July' niet lang meer op zich laten wachten.